$CD8^+$ T cell hyperfunction and immunometabolism in murine models of chronic liver disease

Katrina Jorritsma

Department of Biochemistry, Microbiology and Immunology

Faculty of Medicine

University of Ottawa

Thesis submitted to the Faculty of Medicine in partial

fulfillment of the requirements for the degree of Master of Science in

Microbiology and Immunology

Abstract

Chronic liver disease, whether viral or metabolic, has negative impacts on local and systemic immune function. Notably, $CD8^+$ T cells, which are vital in the immune response to intracellular pathogens and neoplasms, are impacted in their metabolic programming and function. We aimed to further characterize immune impairments in murine models replicating HCV infection and MASLD pathology. We hypothesized that in advanced liver fibrosis, altered $CD8^+$ T cell mitochondrial fitness and upregulated glycolysis are associated with hyperfunction, potentially driving elevated effector functions. In diet-induced liver disease, generalized $CD8^+$ T cell hyperfunction was observed, characterized by elevated GrzB and IFN-γ expression. This was accompanied by transient elevations in ROS and mitochondrial potential as well as upregulated glycolysis and mitochondrial respiration, in a sex-dependent manner. In conclusion, we report that circulating $CD8^+$ T cells are hyperfunctional in a murine model of diet-induced liver disease, replicating many features of MASH.

Acknowledgements

I would like to thank my supervisor Dr. Angela Crawley for her guidance and support, shaping my development as a graduate student. Thank you for always pushing me to participate in conferences and learning experiences, and to engage in critical thinking. I am grateful for the one-on-one support and continuous encouragement you offered through my studies.

I would also like to thank my colleagues in the Crawley lab: namely, Natasha Campeau who helped with animal care, sample processing, staining and flow cytometry; Jeff Li, who not only acted as a mentor but contributed significantly to the optimization, development, and completion of seahorse experiments and supported me in the design and execution of the animal model; and David Lawton who contributed to animal experiments, lending an extra hand in necropsies. I would also like to thank our research associate, Agatha Vranjkovic, for her training and guidance. I am grateful to have completed my studies in such a collaborative environment.

I would like to thank the members of my thesis advisory committee, Drs. Michele Ardolino and Erin Mulvihill. They not only provided excellent feedback at our yearly committee meetings but were always available to offer additional experimental guidance. Thank you, Dr. Ardolino, for your valuable collaborations with the Crawley lab and support for the animal studies.

Lastly, I would like to thank everyone in the Harper Lab, especially Michele Kanaan and Mitali Uppal, who helped me design, troubleshoot and perform seahorse experiments. Lastly, I would like to thank the following University of Ottawa core facilities: The Flow Cytometry and Virometry Core, the Louise Pelletier Histology Core and the Animal Care and Veterinary Services Facility.

Table of contents

List of Figures

List of tables

List of Abbreviations

AUD – Alcohol use disorder

APC – Antigen presenting cell

CCl_3 – Trichloromethyl

CCl_4 – Carbon tetrachloride

DAA – Direct acting antivirals

DAMP – Danger associated molecular pattern

DNL – De novo lipogenesis

ECM – Extracellular matrix

GrzB – Granzyme B

HBV – Hepatitis B virus

HCC – Hepatocellular carcinoma

HCV – Hepatitis C virus

HFD – High-fat diet

HIV – Human immunodeficiency virus

HSC – Hepatic stellate cells

HFMCDD – High-fat, methionine deficient, choline deficient diet

H&E – Hematoxylin and eosin

IL-1β – Interleukin 1 beta

IL- 2 – Interleukin 2

IL-10 – Interleukin 10

IFN-γ – Interferon gamma

kPa – Kilopascals

MASLD – Metabolic dysfunction associated steatotic liver disease

MASH – Metabolic dysfunction associated steatohepatitis

MetS – Metabolic syndrome

MCD – Methionine choline deficient

NAFLD – Non-alcoholic fatty liver disease

NASH – Non-alcoholic steatohepatitis

OXPHOS – Oxidative phosphorylation

PBMC – Peripheral blood mononuclear cells

PBS – Phosphate buffered saline

PWID – People who inject drugs

ROS – Reactive oxygen species

SD – Standard deviation

SLE – Systemic lupus erythematosus

SLD – Steatotic liver disease

SVR – Sustained virologic response

T_E – Effector T cell

TCR – T cell receptor

TGF-β1 – Transforming growth factor beta 1

TNF-α – Tumor necrosis factor alpha

Chapter 1: Introduction

1.1 Burden of chronic liver disease

Chronic liver disease results in significant morbidity and mortality worldwide, currently affecting approximately 1.5 billion people[1]. In Canada, liver disease is the 10th leading cause of death, and impacts 1 in 4 Canadians in their lifetime[2]. Liver disease can be caused by various factors such as hepatic viral infections (i.e., hepatitis C virus), alcohol use disorder (AUD), metabolic dysfunction-associated steatotic liver disease (MASLD, formerly NAFLD) and genetic conditions. Among these, viral hepatitis and MASLD account for most global cases, 38% and 59%, respectively. Meanwhile, AUD contributes to approximately 2% of cases, and affects 1 in 5 Canadians in their lifetime[1,3]. Alcohol abuse or dependence often coincides with viral hepatitis and/or MASLD, further increasing the risk of liver injury and downstream health consequences[4,5]. In North America, metabolic dysfunction-associated steatohepatitis (MASH, formerly NASH) an inflammatory form of MASLD, recently surpassed viral hepatitis as the main cause of liver transplantation, with a 12% increase in MASLD/MASH-related cases in Canada alone[2,6]. These trends can be attributed to the rising epidemic of obesity and diabetes in this population[7,8,9,10].

1.2 HCV infection

1.2.1 HCV infection and disease progression

Hepatitis C virus (HCV) is a blood-borne hepatotropic virus with a heterogenous genome, including seven different genotypes and many subtypes. HCV is rapidly evolving, influenced by geography and host factors, dictating treatment responses and success[11]. It is

transmitted through contact with infected blood; through needle sharing in people who inject drugs (PWID), vertical transmission from mother to child, sexual activity, and poorly sterilized medical equipment[11,12,13]. The World Health Organization vows to eradicate HCV by 2030, reducing disease incidence by 90% and HCV-related deaths by 65%[14]. In Canada, efforts need to primarily be targeted towards prevention and screening in PWID and high-risk populations to meet this target.

HCV infection is often asymptomatic and can develop as acute or chronic in nature. Depending on the viral genotype, approximately 15% of infected individuals develop an acute infection, in which the virus is spontaneously cleared. The remaining 85% develop a chronic, persistent infection, and are at a greater risk of liver damage[15]. In chronically infected individuals, infection often goes undetected and untreated, promoting the development of liver fibrosis, or scar tissue, and liver cancer. Furthermore, host metabolism plays an important role in the progression of HCV-related liver injury. According to viral genotype, HCV influences lipid and glucose metabolism, driving the development of insulin resistance and diabetes. These in turn contribute to the progression of liver fibrosis and steatosis[16,17].

1.2.2 HCV treatment

The previous standard of care for HCV treatment involved the administration of pegylated interferon α (peg-IFNα) and ribavirin. This combination therapy yielded highly variable rates of cure or sustained virological response (SVR), from 40-90%, according to viral genotype and host factors such as age, race, and degree of pre-existing liver injury[18,19]. Peg-IFNα and ribavirin also induced adverse side effects in many patients, such as cognitive dysfunction, anemia, pancreatitis and neutropenia[20]. However, HCV treatment has come a long way in recent

years, marked by the development of direct-acting antivirals (DAAs) in 2011, yielding upwards of 90% SVR rates and fewer adverse reactions. Various DAA regimens exist and are targeted towards specific HCV genotypes, inhibiting viral entry, replication, or life cycle. However, high-risk individuals are susceptible to re-infection post HCV cure, and prevention remains an important barrier to HCV elimination. Furthermore, HCV vaccine development is challenging for many reasons; including viral genetic diversity, a lack of immune competent animal models for vaccine testing, antibody resistance, and the inability to generate robust virus-specific T cell responses[21].

1.2.3 Sex differences in HCV

Males are disproportionately affected by HCV, with higher disease prevalence, elevated HCV RNA levels, more rapid disease progression and lower rates of spontaneous viral clearance[22,23]. Moreover, in Canada, this trend continues to be true as 62% of new HCV diagnoses in 2019 occurred in males[24]. Chronic HCV with cirrhosis poses the highest risk (25%) for hepatocellular carcinoma (HCC)[19], and as expected, males are also more likely to develop HCC than females. These sex differences may be partially caused by the hormone estradiol, which has a protective effect against the development of liver fibrosis, slowing its progression in pre-menopausal females[25]. Immunological mechanisms are thought to contribute to this as well. In HCV-infected males, peripheral blood mononuclear cells (PBMCs) were found to produce more TNF-α, IL-1β, IL-8 and MCP-1, in comparison to healthy controls and age-matched HCV-infected pre-menopausal females. Elevated estradiol correlates with reduced monocyte infiltration into the liver and reduced pro-inflammatory cytokine production from PBMCs, important contributors to liver fibrosis[26]. Furthermore, in animal models of liver disease,

estradiol reduces reactive oxygen species (ROS) production, TGF-β1 expression, hepatic stellate proliferation and collagen deposition[25,27].

1.3 MASLD

1.3.1 MASLD pathogenesis

Approximately 30% of the global population is affected by MASLD[28], of which 20-30% develop the inflammatory form of the disease termed MASH[29]. Metabolic syndrome (MetS), encompassing obesity, insulin resistance, hypertension, and hyperglycemia, is the most important driver of MASLD/MASH. Approximately 75% percent of diabetics develop MASLD, as insulin resistance impairs the regulation of lipolysis, promoting excessive fatty acid deposition in the liver[30,31]. However, the literature also reports the role of MASLD as a driver of insulin resistance. *De novo* lipogenesis (DNL), the synthesis of fatty acids from dietary glucose and fructose, triggers inflammatory processes and insulin resistance. Danger-associated molecular patterns (DAMPs), such as saturated fatty acids resulting from DNL, contribute to inflammasome activation in the liver and downstream pro-inflammatory IL-1β and IL-10 expression[30]. Recent evidence also shows that the gut microbiome plays an important role in disease progression, contributing to chronic hepatic inflammation[32,30]. Furthermore, diabetes and obesity each increase the risk of HCC four times in comparison to those without diabetes and of healthy weight, respectively[33]. Therefore, individuals with co-morbid MASLD, obesity, diabetes, and dysbiosis are more likely to progress to MASH, cirrhosis, and HCC.

1.3.2 Diagnosis and treatment of MASLD

Similar to HCV, individuals with MASLD are often asymptomatic, and signs of the disease may only become apparent once they have progressed to advanced liver fibrosis and steatohepatitis. However, certain markers such as ALT/AST can be used in routine blood testing to identify individuals with abnormal liver function and potential MASLD. MASLD is diagnosed when steatosis is present in >5% of hepatocytes, which is quantified using various imaging tools such as ultrasound, CT, and MRI. Unfortunately, the definitive diagnosis of MASH requires liver biopsy[30], which is no longer standard practice given the magnitude of individuals with potential MASLD. Currently, the most effective intervention for the treatment of MASLD, in the context of obesity and diabetes, remains lifestyle interventions such as dietary modifications and physical activity. Given the complexities of MASLD/MASH, treatment targets are elusive and complex. Although many therapeutic agents exist, such as thiazolidinediones, to improve insulin sensitivity in diabetes[34,35], these have not been tested in combination with other agents in long-term clinical trials. Combination therapy is likely needed to target lipid metabolism, oxidative stress, inflammation, and dysbiosis, but no single drug with multiple metabolic targets exists.

1.3.3 Sex differences in MASLD

Estrogens have also been found to have a protective effect against the development of liver fibrosis in MASLD and are associated with lower MASLD/MASH disease prevalence and slower disease progression in pre-menopausal females. This effect is also extended in post-menopausal females receiving hormone replacement therapy, supplementing exogenous estrogen[36]. Males exhibit more severe steatosis/steatohepatitis, more advanced fibrosis, elevated pro-inflammatory cytokine levels, higher liver tumour incidence and increased overall

mortality[37]. An important contributing factor to MASLD development is fat distribution and males tend to accumulate more visceral adiposity, which contributes to systemic inflammation, insulin resistance and hepatocyte metabolic stress. This accelerates liver fibrosis progression, increasing the risk of HCC[38,39]. Similar findings have been replicated in animal models, in which estrogen supplementation has a protective effect against insulin resistance, lipogenesis, glucose tolerance and body weight gain[18,40], important risk factors in MASLD/MASH.

1.4 Liver fibrosis

1.4.1 Liver fibrosis progression

Liver fibrosis is triggered by repetitive cycles of tissue damage and repair, progressively increasing scar tissue development. Inflammation is a major driver of fibrogenesis, and the secretion of pro-inflammatory cytokines from immune cells and HCV-infected hepatocytes activate hepatic stellate cells (HSC). DAMPs, resulting from hepatocyte death, also play an important role in HSC activation, either directly acting on HSCs or activating Kupffer cells to produce pro-inflammatory IL-1, TNF-α and TGF-β1. Differentiated HSCs, myofibroblasts, then deposit extracellular matrix (ECM) components such as type I and III collagen, fibronectin and proteoglycans in the liver[41,42].

Over time, liver fibrosis in chronic HCV and MASLD/MASH progresses to cirrhosis, increasing the risk of liver decompensation and HCC. An estimated 1-6% of cirrhotic HCV-infected individuals develop HCC annually[43,44], while approximately 2.6% of individuals with cirrhotic MASH develop HCC[45]. HCC accounts for approximately 75-85% of primary liver cancer cases, which is the third leading cause of cancer-related deaths worldwide[46]. Hepatocyte

death, inflammation, ROS and DNA damage play an important role in HCC development, promoting hepatocyte mutation[47].

1.4.2 Liver fibrosis scoring

Many methods can be used to grade liver fibrosis in HCV and MASLD patients, each varying in accuracy, complexity, and risk. Liver biopsies have commonly been used for fibrosis scoring; however, these procedures are invasive, introduce frequent complications and are subject to intra-observer variation. Biopsies also have high rates of sampling error, in which small tissue samples do not accurately portray liver pathology[48]. In liver biopsy, the METAVIR scale attributes a score of F0-4 according to fibrosis severity: F0: no fibrosis, F1: portal fibrosis without septa, F2: portal fibrosis with rare septa, F3: numerous septa without cirrhosis and F4: cirrhosis[49]. Though liver biopsy is no longer the gold standard, the METAVIR scoring system is still widely relevant.

Today, minimally invasive strategies are commonly used, such as transient elastography, also known as FibroScan[50]. This technique measures liver stiffness in kilopascals (Kpa) for which associations with F-scores can be made in a disease-specific manner. Individuals are classified in the following categories; healthy liver: 2-7 kPa (F0), minimal fibrosis: 8-9 kPa in HCV or 7.5-10 kPa in MASLD (F1-2), advanced fibrosis: 9-14 kPa in HCV or 10-14 kPa in MASLD (F3) and cirrhosis: ≥14 kPa (F4)[51]. The fibrosis 4 (FIB4) index can also be used to grade fibrosis, providing an estimate of fibrosis severity based on an algorithm that includes age, ALT/AST levels and platelet count. However, it can have sub-optimal sensitivity in older patients with advanced fibrosis and may be poorly generalizable to individuals with MASLD/MASH[52].

1.5 Immune cells and their role in liver injury

Many innate and adaptive immune cells play a direct role in the progression of liver tissue injury. Notably, the interplay between T cells, B cells and macrophages triggers a cascade of inflammatory processes in the liver, driving fibrosis. In MASLD, liver resident Kupffer cells initiate inflammatory processes in response to elevated fatty acids, producing TNF-α, IL-1β and chemokines attracting circulating monocytes. Once infiltrated in the inflamed liver, monocytes differentiate into pro-inflammatory M1 macrophages, producing ROS and inflammatory cytokines[53,54]. Furthermore, liver-infiltrating $CD8^+$ T cells have been found to express pro-inflammatory IL-10, increase hepatic macrophage infiltration, and induce HSC activation[55]. In HCV, liver infiltrating $CD8^+$ T cells contribute to liver pathology through the killing of virus-infected hepatocytes and non-specific inflammatory responses[56]. In MASH, $CD8^+$ T cells display an activated-exhausted phenotype, producing elevated TNF-α, IFN-γ, GrzB and PD-1, and are involved in non-specific killing of hepatocytes[57]. Meanwhile $CD4^+$ T cell subsets play a multitude of roles, either contributing to or preventing disease progression. In MASH, an imbalance in the Th17/Tregs ratio drives chronic inflammation[58] and IL-17 has been found to activate STAT3 signaling and HSCs to produce type 1 collagen[59]. Finally, B cells play a role in the progression of liver fibrosis through IgG-mediated insulin resistance, and activation of T cells and macrophages[53,60,61].

1.6 $CD8^+$ T cell dysfunction

1.6.1 $CD8^+$ T cell function

$CD8^+$ T cells play an important role in the response to intracellular pathogens and certain cancers. Naïve quiescent cells traffic through the circulation, and frequently passage through the

spleen and lymph nodes where they may encounter immune cells presenting their cognate antigens. Naïve T cells are activated following the antigen-specific T cell receptor (TCR) recognition of peptide- major histocompatibility complex 1 (MHC I) on antigen presenting cells (APCs) and the obligatory receipt of co-stimulatory signals from the binding of CD28 with CD80/CD86 on APCs. These signals promote clonal expansion and differentiation into effector cells (T_E)[62,63].

Upon activation, T_E lose CD62L and CCR7 expression and are trafficked to the site of infection or injury, where they release cytokines such as TNF-α, IL-2 and IFN-γ[64,65,66]. Cell surface antigen recognition by $CD8^+$ T cells triggers the release of lytic granules containing cytotoxic perforin and granzymes. Perforin creates pores in the lipid bilayer of target cells, allowing for granzyme-mediated apoptosis. Target cell death can also be initiated by the Fas/FasL interaction or TNF-α death receptor ligation[67]. These mechanisms drive virus-specific $CD8^+$ T cell mediated viral clearance in HCV infection[68], and tumor control in HCC[69]. After challenge, the majority of short lived T_E cells then undergo apoptosis in a contraction phase, while the remaining 5-10% of these cells persist as long-lived memory cells[64], conferring long-term protection against repeat antigen exposure.

1.6.2 $CD8^+$ T cell exhaustion

Prolonged antigen exposure in chronic infection and cancer can promote $CD8^+$ T cell exhaustion, limiting effective cellular defense mechanisms. In chronic viral infections, particularly HCV and HIV, exhausted $CD8^+$ T cells progressively lose effector functions, noted by an impairment in IL-2, IFN-γ and TNF-α production. These cells also express many inhibitory receptors, such as PD-1, CTLA-4, Tim-3 and LAG3[70,71,72], and downregulate trafficking

molecules such as CCR7 and CD62L[64]. Yates et al. demonstrated that exhausted $CD8^+$ T cells in HCV and other viral infections have distinct epigenetic signatures, which persist long after viral clearance with DAA therapy. These are termed "epigenetic scars", likely a result of chronic TCR signaling[73]. In HCC, exhausted tumour specific $CD8^+$ T cells are impaired by the immunosuppressive tumour microenvironment. This includes the overexpression of PD-L1 and PD-L2 on cancer cells, which bind to upregulated PD-1 on exhausted $CD8^+$ T cells, inhibiting co-stimulation and TCR signaling. Therefore, PD-1 overexpression on bulk and antigen-specific $CD8^+$ T cells inhibits cytokine production and expression of pro-survival Bcl-2[66,74,75,76].

1.6.3 T cell hyperfunction

The notion of immune overactivation, including T cell hyperfunction, has been reported in many chronic infections, such as HCV and HIV[77,78]. The Crawley lab has observed hyperfunction of bulk circulating $CD8^+$ T cells in individuals with chronic HCV infection, correlating with the degree of sustained liver injury. This hyperfunction, characterized by an increase in IFN-γ and perforin expression, was apparent in individuals with cirrhosis (F4), and persisted even after viral clearance with DAAs. These $CD8^+$ T cells sustained elevated IFN-γ and perforin expression 24-weeks post SVR, in comparison to minimally fibrotic and healthy individuals[77]. Aberrant, bulk T cell activation also occurs in HIV infection and HIV/HCV co-infection, influencing antiretroviral therapy efficacy. In HIV infected patients, $CD8^+$ T cells express elevated activation markers CD38 and HLA-DR[78]. Finally, in MASLD, it was found that tissue resident $CXCR6^+$ $CD8^+$ T cells display an activated exhausted phenotype, expressing elevated granzyme, TNFα, IFNγ as well as PD-1[57]. However, the effect of MASLD on bulk circulating $CD8^+$ T cells needs to be better characterized.

1.7 Metabolism as a driver of T cell function

1.7.1 Overview of T cell metabolism

Naïve, effector and memory T cells adopt different metabolic states to meet their functional demands. Naïve T cells rely primarily on fatty acid oxidation and oxidative phosphorylation (OXPHOS) to generate ATP. Upon TCR activation, CD28 mediated signaling activates the PI3K-AKT signaling pathway, increasing GLUT1 expression and cellular glucose uptake[79,80,81]. Activated T cells rely largely on glycolysis for energy production, which rapidly supplies the ATP necessary for effector functions, notably IFN-γ production. On the other hand, memory T cells have a similar resting metabolic state to naïve T cells but respond much faster to repeat antigen challenges. Memory cells can more rapidly uptake glucose and engage in glycolysis. Furthermore, nutrient availability in the T cell environment can also influence metabolism, function, cytokine production and cell signaling[80,82]. For example, in low nutrient conditions (elevated ADP+AMP/ATP ratio), AMPK inhibits mTOR activity, increasing catabolism to replenish energy stores[79].

1.7.2 T cell metabolism in chronic disease

In chronic infections, such as HCV and the murine model of chronic lymphocytic choriomeningitis virus (LCMV) infection, exhausted virus specific $CD8^+$ T cells have reduced mitochondrial potential, elevated ROS and impaired mitochondrial respiration and glycolysis. Downregulation of these metabolic pathways suppresses T cell effector functions, negatively impacting infection control[83,84,85]. Furthermore, in hepatitis B virus (HBV) infection, it was found that exhausted virus specific $CD8^+$ T cells have impaired metabolic plasticity. These cells were unable to shift between glycolysis and OXPHOS in response to nutrient availability, in

contrast to more functional CMV-specific cells[86]. On the other hand, chronically activated autoreactive $CD4^+$ T cells in systemic lupus erythematosus (SLE) have higher mitochondrial respiration and glycolytic capacity, supporting effector function. These T cells have been found to have elevated mTOR activity and overexpression of GLUT1, increasing glycolytic flux and supporting the overproduction of IFN-γ[87,88,89].

In obesity, a common precursor to MASLD and MASH, distinct metabolic alterations in $CD8^+$ T cells have also been noted. However, T cell metabolism in diet-induced liver disease remains incompletely understood, as some groups report $CD8^+$ T cell exhaustion[90,91], while others report elevated $CD8^+$ T cell metabolism and function. Finlay et al. reported that in mice with diet-induced obesity, splenic and lymph node antigen-specific $CD8^+$ T cells have elevated glycolytic capacity, resulting from activated mTOR and HIF1 pathways[92].

1.8 Animal models of chronic liver disease

1.8.1 Model of hepatotoxin-induced liver fibrosis

The use of animal models to study HCV-related immune dysfunction remains challenging. Chimpanzees, the only animals naturally susceptible to HCV, are no longer commonly used in laboratory research due to ethical and practical limitations[93]. Therefore, methods to study HCV infection or HCV-related pathology were developed in small animal models, notably rodents. To replicate HCV-induced liver pathology, in the absence of experimentally confounding viral infection, a model of carbon tetrachloride (CCl_4) induced liver injury was developed. This potent hepatotoxin is injected intraperitoneally (i.p.) and is metabolically activated by hepatocytes, converting it to trichloromethyl (CCl_3). CCl_3 radicals induce hepatocyte death, impair lipid metabolism, increase cellular ROS production and recruit

macrophages which release pro-inflammatory cytokines, contributing to fibrotic tissue development[94,95]. Over 8-20 weeks, CCl_4 administration induces pericentral fibrosis with eventual central-portal bridging, leading to cirrhosis[96].

1.8.2 Models of diet-induced liver fibrosis

Many models of diet-induced liver disease exist, including the methionine and choline deficient (MCD) diet, high-fat diets (HFD), Western diets and many others. Unfortunately, only few models induce advanced liver fibrosis, MetS, and systemic inflammation characteristic of MASLD and MASH. The MCD diet restricts key micronutrients, important in triglyceride export from the liver[97], inducing rapid development of liver steatosis and fibrosis, while causing severe weight loss (>15% of body weight) within only a few weeks. These MCD-fed animals lack hallmark features of MetS such as overweight/ obesity, hyperglycemia, insulin resistance and elevated serum triglycerides, poorly replicating human MASLD[98]. On the other hand, HFDs (≥45% fat) better replicate MetS with significant elevations in body mass, but do not rapidly or consistently induce advanced liver fibrosis, even after upwards of 24 weeks of feeding[99,100].

To overcome the challenges associated with both the MCD diet and HFDs, the high fat, methionine, and choline deficient diet (HFMCDD) composed of 60% fat, 0.1% methionine and no added choline was recently developed. This murine model of MASLD integrates both diets to rapidly generate advanced liver fibrosis, prevent weight loss and induce MetS marked by dyslipidemia and hyperglycemia[99,101]. Animals often maintain a similar weight to controls, removing obesity as a potential confounder to experimental studies. This model has also been shown to induce moderate fibrosis (F1/2) by 4 weeks of diet-feeding, periportal-sinusoidal (F2) fibrosis by 8 weeks and advanced bridging pan-lobular fibrosis (F3) by 12 weeks[102].

1.9 Rationale and hypothesis

Research in the Crawley lab has shown that $CD8^+$ T cells are hyperfunctional in both chronic HCV and a murine model of hepatotoxin-induced liver disease. In both cases, $CD8^+$ T cells express elevated cytotoxic molecules and pro-inflammatory IFN-γ in advanced liver fibrosis, in a lasting manner[77,103]. The Crawley lab has also found that the gene expression profiles in HCV-infected individuals with minimal and advanced fibrosis vary significantly. Many of these differentially expressed genes are involved in metabolic pathways, such as glycolysis, OXPHOS, lipid metabolism and mTOR signaling[104]. Other groups have reported direct $CD8^+$ T cell metabolic impairments in chronically activated, exhausted HCV and HIV-specific $CD8^+$ T cells, influencing effector function[70–73]. However, the metabolic phenotype of hyperfunctional peripheral $CD8^+$ T cells in chronic liver disease is not well characterized. As $CD8^+$ T cells are crucial in the immune response to intracellular pathogens and cancer, it is important to understand how cellular metabolism is impaired and whether this knowledge can be leveraged to improve immune responses therapeutically. In advanced liver fibrosis and MASLD, the interaction between host and cellular metabolism, as well as the influence of metabolism on $CD8^+$ T cell function, are poorly understood.

Hypothesis: In advanced liver fibrosis, altered $CD8^+$ T cell mitochondrial fitness and upregulated glycolysis are associated with lasting cellular hyperfunction.

1.10 Objectives

1. Determine if $CD8^+$ T cell hyperfunction is associated with altered mitochondrial fitness in murine models of advanced liver fibrosis.

2. Evaluate $CD8^+$ T cell glycolysis and oxidative phosphorylation in a model of diet-induced liver injury.
3. Evaluate lasting alterations in $CD8^+$ T cell function and metabolism after the removal of liver insult.

Chapter 2: Material and Methods

2.1 Animals

Animal projects fall under the approved protocol OHRIe-3003 with the Animal Care and Veterinary Service (ACVS) at the University of Ottawa, certified by the Canadian Council on Animal Care. In the CCl_4 and HFMCDD experiments, C57BL/6 mice were purchased from Jackson Laboratory or bred at the University of Ottawa ACVS facility. At treatment initiation, animals were aged between 7-10 weeks. In the high-fat diet experiments, mice were bred and housed at the Carleton University vivarium, through a collaboration with Dr. Jennifer Bruin.

Table 1: Animal studies conducted

Study		Number of mice	Sex	Treatment	Treatment duration
CCl_4	*E01	14	8M, 6F	M: 4 ctl, 4 CCl_4 F: 3 ctl, 3 CCl_4	16 weeks
	E02	22	15M, 7F	M: 6 ctl, 9 CCl_4 F: 4 3 ctl, CCl_4	21 weeks
HFMCDD	E01	21	M	9 ctl, 12 diet	21 + 4 weeks regression
	E02	19	F	7 ctl, 12 diet	21 + 4 weeks regression
	E03	24	12M, 12F	M: 6 ctl, 6 diet F: 7 ctl, 5 diet	17 weeks

CCl_4 – carbon tetrachloride
HFMCDD – High fat methionine deficient choline deficient diet
*E01 was conducted using OT-1 C57BL/6 mice

2.2 CCl_4 administration

In a model of hepatotoxin-induced liver fibrosis, C57BL/6 mice were injected i.p. with 0.1mL of CCl_4 (≥99.5%, anhydrous, Sigma-Aldrich, MO, USA) at a concentration of 1.0mL/kg of body weight diluted in filtered household olive oil (Bertolli). Control mice were injected with olive oil alone. Animals were injected twice weekly for 16-21 weeks. Body weight and overall physical condition were carefully monitored for signs of distress, such as ≥20% loss in body weight, reduced mobility, hunching and/or piloerection, used to justify humane endpoint.

2.3 The HFMCDD model of liver disease

In a model of diet-induced liver fibrosis, C57BL/6 mice were placed on the HFMCDD composed of 60% kcals from fat, 0.1% methionine without added choline (A06071302, Cedarlane, ON, CAN) *ad libitum*[105]. Animal cages and diet pellets were changed 2-3 times weekly due to their high lard content and rapid breakdown. Control animals remained on the standard chow diet (Teklad diet #2018) composed of 24% kcals from protein, 18% kcals from fat and 58% kcals from carbohydrates, supplemented with 0.4% methionine and 1200mg/kg of choline[106], provided by the University of Ottawa ACVS. Body weight and overall fitness were monitored 2-3 times weekly.

2.4 The high fat diet model of liver disease

To induce liver disease using a high-fat diet (HFD) model, C57BL/6 mice aged 28-30 weeks were placed on a 45% high fat diet (Research Diets, D12451)[107] for 14 weeks. Controls remained on a standard chow diet composed of 13% kcals from fat, 20% kcals from protein, 67% kcals from carbohydrates (Teklad Diet #2014)[108] provided by the University of Carleton

vivarium. Fat and lean mass were measured relative to total body weight at week 11 using an EchoMRI-700 (EchoMRI LLC, Houston, TX, USA), and a glucose tolerance test was performed at week 13 to evaluate systemic glucose homeostasis.

2.5 Liver perfusion and histology

At endpoint, animals were euthanized by carbon dioxide inhalation at the uOttawa ACVS facility. The abdomen was disinfected using 70% ethanol and a midline incision was performed exposing the liver, heart, and inferior vena cava. Livers were then perfused with approximately 50mL of PBS through cardiac puncture. Sections taken from the right lobe of the liver were fixed in 4% paraformaldehyde (Sigma-Aldrich, MO, USA) for 72 hours, and then transferred to 70% ethanol. Samples were sent to the Louise Pelletier Histology Core Facility for paraffin embedding, sectioning, and staining. Liver sections were stained with Masson's Trichrome stain for visualization of fibrotic tissue, and with Hematoxylin and Eosin (H&E) for the visualization of ballooning, steatosis, and inflammation. Liver injury and fibrosis scores (METAVIR Scale, F0-4) were determined by an experienced pathologist (Nour Histopathology Consultation Services, Ottawa, ON, Canada).

2.6 Blood collection and PBMC isolation

Blood samples were collected at baseline, before treatment initiation, and every subsequent 4 weeks. Blood was collected from the lateral saphenous vein using Microvette CB300 tubes (Fisher Scientific, CA, USA) containing heparin to prevent sample coagulation. Blood was lysed with Hybri-Max^{TM} Red Blood Cell Lysing Buffer (Sigma-Aldrich, MO, USA) for 8 minutes to remove red blood cell contamination. Pelleted cells were then washed with PBS,

counted by trypan blue exclusion, and resuspended at a density of $1x10^6$ cells/mL in 20% RPMI medium.

2.7 PBMC stimulation and culture

For cell stimulation, a 96-well high-binding plate was coated with anti-CD3 antibodies (5μg/mL in PBS, clone 145-2C11, BD Biosciences, CA, USA) for one hour at 37°C. After incubation, the plate was washed twice with PBS. Isolated PBMCs were then plated at a density of $2x10^5$ cells/well with soluble anti-CD28 (2μg/mL in 20% RPMI medium, clone 37.51, BD Biosciences, CA, USA) and cultured for 48 hours at 37°C.

2.8 Flow cytometry

$CD8^+$ T cell phenotype and function

Five hours prior to the end of the 48-hour stimulation, PBMCs were supplemented with protein transport inhibitors Brefeldin (GolgiPlug, BD Biosciences, CA, USA) and Monensin (GolgiStop, BD Biosciences, CA, USA). At the end of the 48-hour stimulation, cells were then transferred to a 96-well v-bottom plate and washed with PBS. For labeling of dead cells, 100μL of Zombie NIR was added to each well (1:5000 dilution in PBS, Biolegend), and incubated for 20 minutes at room temperature. Next, 50μL of F_C block (clone 2.4G2, BD Biosciences) was added to each well and incubated for 20 minutes at room temperature to prevent non-specific antibody binding. To distinguish cell phenotypes, cells were stained with 50μL of cell surface antibody cocktail containing BV785 CD8 (clone 53.6-7, BioLegend), Alexa Fluor 700 CD4 (clone GK1.5, BioLegend), BV421 CD44 (clone IM7, BioLegend), PE CD62L (clone MEL-14, BioLegend) and PE-Cy5 CD19 (clone 6D5, BioLegend). For intracellular staining, cells were

first fixed using Cytofix/Cytoperm Fixation/Permeabilization kit (BD Biosciences, CA, USA) for 20 minutes at room temperature. Finally, cells were stained with 100μL of BV650 IFN-γ (clone XMG1.2, BioLegend) and PE-CF594 GrzB (clone GB11, BD Biosciences) cocktail for 30 minutes. The plate was refrigerated overnight, and samples were analyzed the following day on the Cytek Aurora at the University of Ottawa Flow Cytometry and Virometry Core Facility. $CD8^+$ T cell function was determined by gating on whole PBMCs, single cells, live cells, $CD19^-$ $CD8^+$ cells and finally IFN-γ^+ or $GrzB^+$ cells using unstimulated samples to set respective gates.

$CD8^+$ T cell mitochondrial potential and reactive oxygen species

Immediately after PBMC isolation cells were plated at a density of $2x10^5$ cells/well and washed with 200μL of PBS. Dead cells were labeled with Zombie NIR (1:5000 dilution in PBS, Biolegend) for 20 minutes at room temperature. Next, 50μL of F_C block (clone 2.4G2, BD Biosciences) was added to each well and incubated for 20 minutes at room temperature to prevent non-specific antibody binding. Cells were stained with 50μL of the cell surface marker cocktail containing; Pacific Blue CD8 (clone 53-6.7, Biolegend), cFluor V610 CD4 (clone RM4-5, Cytek), BYG781 CD44 (clone IM7, Cytek) and BV785 CD62L (clone MEL-14, Biolegend) for 20 minutes at room temperature. Cells were then stained with 100μL of 25nM Mitotracker Deep Red in PBS (ThermoFisher Scientific, MA, USA) for 20 minutes at 37°C. Last of all, cells were stained with 100μL of 5μM CellROX Green in PBS (ThermoFisher Scientific, MA, USA) for 30 minutes at 37°C. Mitochondrial potential and reactive oxygen species (ROS) were determined using Mitotracker Deep Red and CellROX green mean fluorescent intensity (MFI) respectively, immediately after staining, on the Cytek Aurora.

2.9 Spleen collection and splenocyte isolation

Spleens were homogenized using sterilized frosted glass slides and strained through a 70μM strainer, into cold unsupplemented RPMI medium, to remove remaining tissue. Samples were then lysed with 3mL of cold Hybri-Max™ Red Blood Cell Lysing Buffer (Sigma-Aldrich, MO, USA) for 5 minutes to remove red blood cell contamination. Remaining splenocytes were washed with cold PBS and counted by trypan blue exclusion.

2.10 $CD8^+$ T cell isolation

Spleens were harvested and splenocytes isolated as described in section 2.9. From splenocytes, $CD8^+$ T cells were isolated by negative magnetic bead selection (EasySep™ Mouse $CD8^+$ T cell Isolation Kit, STEMCELL, BC, CAN). Briefly, cells were suspended in sorting buffer (PBS with 2% FBS and 1mM EDTA) at $1x10^8$ cells/mL. Cells were then incubated for 10 minutes at room temperature with 20μL/mL of F_C block and 50μL/mL of isolation cocktail. Then, 125μL/mL of Streptavidin RapidSpheres™ were added for 5 minutes before placing the samples in the EasySep™ magnet for 2.5 minutes[109]. Unlabeled $CD8^+$ T cells were poured off, washed with PBS, and counted by trypan blue exclusion.

2.11 Adoptive transfer of $CD8^+$ T cells

OT-1 C57BL/6 mice were euthanized, and their spleens harvested. Spleens were homogenized using the plunger of a 30mL syringe and strained through a 70μM strainer. Samples were lysed with 3mL of cold Hybri-Max™ Red Blood Cell Lysing Buffer (Sigma-Aldrich, MO, USA) for 5 minutes[110,111]. Splenocytes were washed with cold PBS and counted by trypan blue exclusion. $CD8^+$ T cells were then isolated using the EasySep™ Mouse negative

$CD8^+$ T cell Isolation Kit as described in section 2.10. $CD8^+$ T cells were re-suspended in PBS at $1x10^6 – 2x10^7$ cells/mL. Then, 100uL of cells in PBS were injected via intravenous (i.v.) tail vein injection into CD45.1 C567BL/6 mice for a total of $1x10^5 – 2x10^6$ $CD8^+$ T cells over four independent experiments. $CD8^+$ T cells were then followed one-week post-adoptive transfer through flow cytometry analysis of recipient saphenous blood PBMCs. Cell surface antibodies FITC CD45.1 (clone A20, Biolegend) and BV510 CD45.2 (clone 104, Biolegend) were used to label recipient and donor-specific cells, in addition to the complete antibody panel described in section 2.8.

2.12 Seahorse metabolic assay

Oxygen consumption rate (OCR) and extracellular acidification rate (ECAR) were quantified using the Seahorse XFe96 Extracellular Flux Analyzer (Agilent, CA, USA) provided by the Harper Lab at the University of Ottawa. On the day of the assay, Seahorse 96-well plates were coated with 50μL/ well of Poly-D-lysine (PDL) at a concentration of 50μg/mL[112] (ThermoFisher, MA, USA) for 1 hour at room temperature, and then stored at 4°C. Freshly isolated $CD8^+$ T cells were seeded at a density of $2.5x10^5$ cells/ well onto the PDL pre-coated XF96 plate. Cells were suspended in nonbuffered XF RPMI 1640 medium supplemented with 10mM glucose, 2mM L-glutamine and 1mM pyruvate (Agilent, CA, USA). ECAR and OCR were measured in response to the sequential injection of 2.5μM of oligomycin, 2.0μM of FCCP, 1.0μM of each rotenone/antimycin A and 20μM of monensin.

2.13 Analysis and statistics

Flow cytometry experiments were completed on the Cytek Aurora, and data were analyzed using FlowJo 10.8.2 software. Compensation, or spectral unmixing, was performed in SpectroFlo® software on the Cytek Aurora. Graphs and statistical analysis were generated using GraphPad Prism 10.0 software. Data are presented as means ± standard deviation (SD), and statistical analyses were completed using unpaired one and two-tailed Student's *t*-test and two-way ANOVA ($p \leq 0.05$).

Chapter 3: Results

3.1 Carbon tetrachloride model of liver fibrosis

3.1.1 The effect of CCl_4 on body weight

The CCl_4 model is used to generate advanced liver fibrosis and centrilobular necrosis in mice[96], modeling HCV-induced tissue damage. Following previously described methods, approximately 8-week-old C57BL/6 mice were treated with CCl_4, a potent hepatotoxin, for 21 weeks (Figure 1A). Through treatment, body weight was measured at regular intervals (2x/week) and mice were monitored for physical signs of distress, such as hunching and piloerection, and humane euthanasia was performed with ≥ 20% body weight loss. Control and CCl_4 groups were of similar weight at treatment initiation and gained weight at similar rates. There were no statistically significant differences in body weight through treatment, despite a transient drop in weight in the CCl_4 group at week 17 (Figure 1B). This can potentially be attributed to the prolonged treatment period. These mice were administered CCl_4 for 16-21 weeks, unlike previous experiments, in which treatment duration lasted approximately 12 weeks.

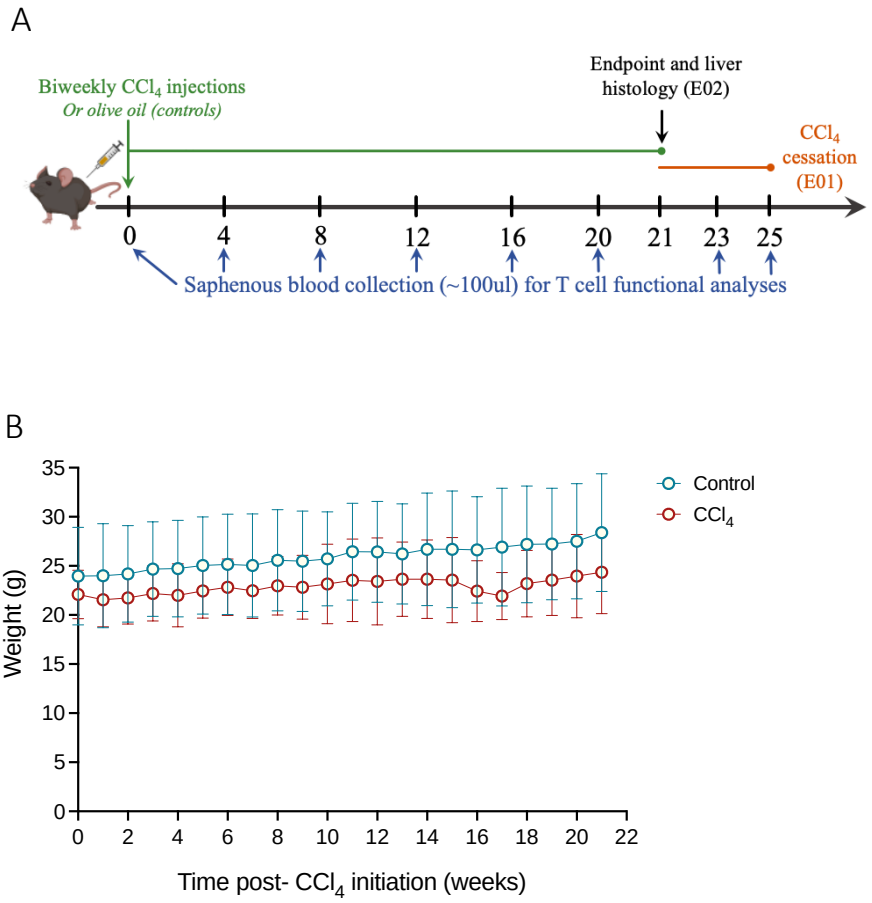

Figure 1: Model of CCl_4-induced liver fibrosis.

(A) A schematic of the experimental design is shown. C57BL/6 mice aged approximately 8 weeks were injected intraperitoneally (i.p.) 2x/ week with CCl_4 (0.1mL, 1.0mL/kg of body weight) for 16-21 weeks. Saphenous blood samples were collected at baseline and every subsequent 4 weeks to assess circulating $CD8^+$ T cell function. At the experimental endpoint, liver sections from euthanized mice were collected for histology. (B) Control (oil) and CCl_4-treated animals show similar patterns of weight gain through treatment. Data presented as group means ±SD. No statistically significant differences exist between groups, determined using a two-way ANOVA test.

3.1.2 Liver fibrosis severity in CCl_4-treated animals

a. *Liver injury at peak CCl_4 treatment*

Liver histology was performed in CCl_4 E02, an experiment completed in collaboration with Jiafeng Li, a PhD candidate in the Crawley lab. Animals were euthanized and liver sections were stained with Masson's Trichrome (Figure 2A-B) for histology, after 21 weeks of CCl_4 treatment. This dye allows for the differentiation between muscle tissue, stained in red, and collagen fibres, stained in blue[113]. At this time, CCl_4 treated mice had significantly elevated liver fibrosis in comparison to oil-treated mice (Figure 2C). When stratifying these results by sex, this effect is lost in females, in which there was large variability in fibrosis scores among CCl_4 animals, ranging from F0-F4 (Figure 2D). Meanwhile, the difference between groups remained significant in males, in which all CCl_4 treated mice had advanced (F3) liver fibrosis (Figure 2E). Furthermore, all oil-treated controls had some degree of liver fibrosis, most scoring F1-2, and one with F3 fibrosis. These results differed from the Crawley lab's previous findings in this model, in which control mice normally exhibit no fibrosis (F0) or very minimal fibrosis (F1)[103].

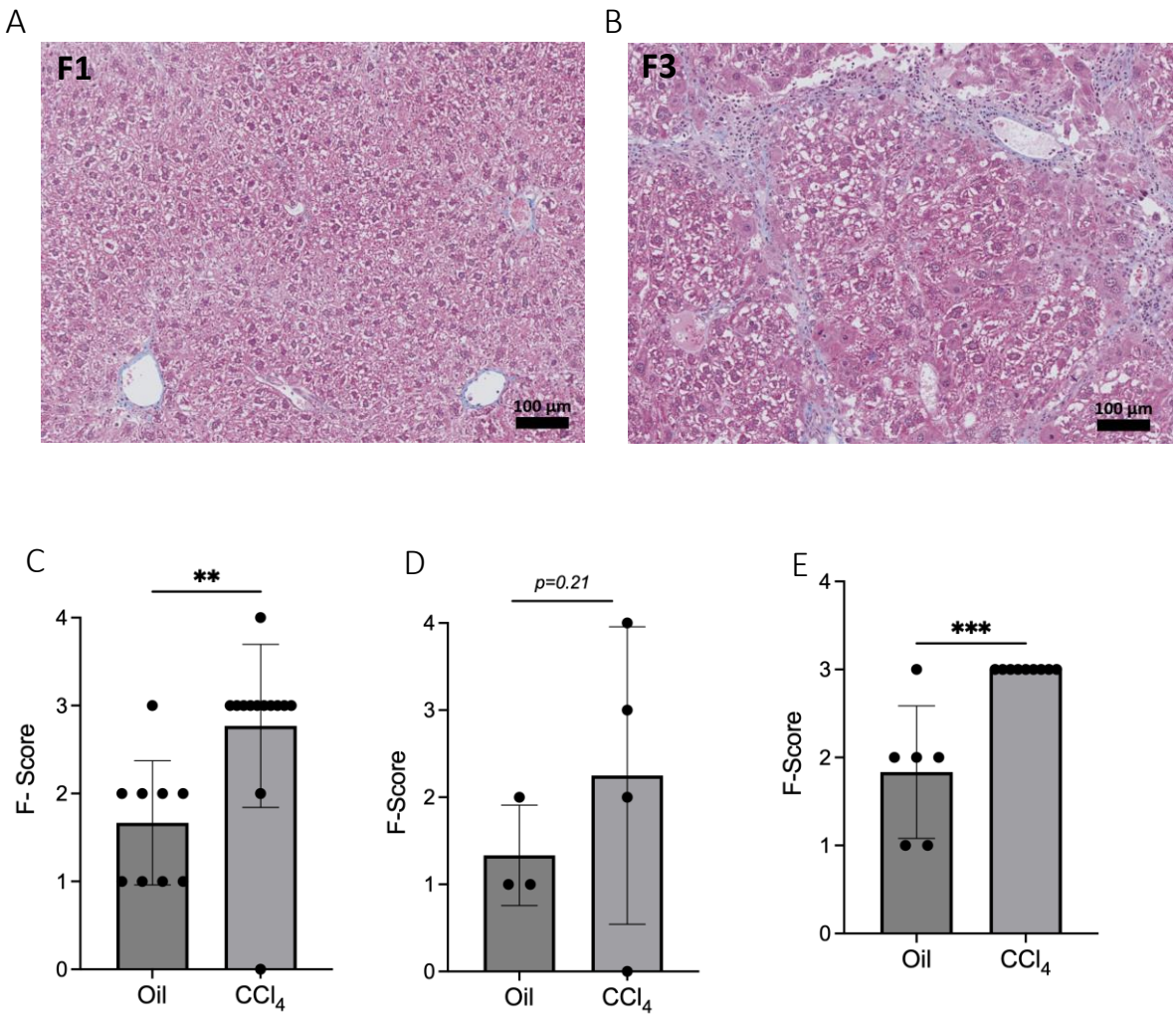

Figure 2: CCl_4 induces advanced liver fibrosis in C57BL/6 mice.

At the experimental endpoint of 21 weeks, animals were euthanized for liver histology. Liver sections collected from the right lobe were formalin-fixed and paraffin embedded, then sectioned and stained with Masson's Trichrome stain. Fibrosis staging was determined using the METAVIR (F-score) scoring system: F0 = no fibrosis, F1/2 = minimal liver fibrosis, F3/4 = advanced fibrosis. (A) Representative liver histology image for control and (B) CCl_4 mice. (C) Summary of liver fibrosis scores in the entire cohort (n=15M, 7F), (D) in females and (E) in males after 21 weeks of treatment. Data are presented as group means ±SD and statistically significant differences were determined using a one-tailed unpaired Student's *t*-test (**$p \leq 0.01$, ***$p \leq 0.001$).

b. Liver injury following CCl_4 cessation

Liver histology was also performed in CCl_4 E01 for the assessment of liver injury post-CCl_4 cessation. These animals were administered CCl_4 or oil, as previously described, for a period of 16 weeks, after which treatment was stopped. Following this 4-week regression period, animals were euthanized for liver histology, in which liver sections were stained with Masson's Trichrome for the assessment of fibrosis severity (Figure 3A and B). CCl_4-treated animals exhibited moderate liver fibrosis, with scores ranging from F1-2, while controls displayed larger variability (F0-2). Half of the animals in the control group sustained liver injury, which persisted following i.p. oil cessation. Interestingly, there was significantly elevated liver fibrosis in the CCl_4 group even after the treatment cessation period (Figure 3C). Therefore, differences in liver fibrosis are somewhat sustained after 4 weeks. The degree of liver injury remodelling cannot be quantified in this cohort, as sample size did not allow for histological analyses of a subset of animals at peak treatment. However, according to the previous findings in this model, and the results discussed above, the animals in the CCl_4 group likely would have developed moderate to advanced liver fibrosis (F2-4) at peak treatment.

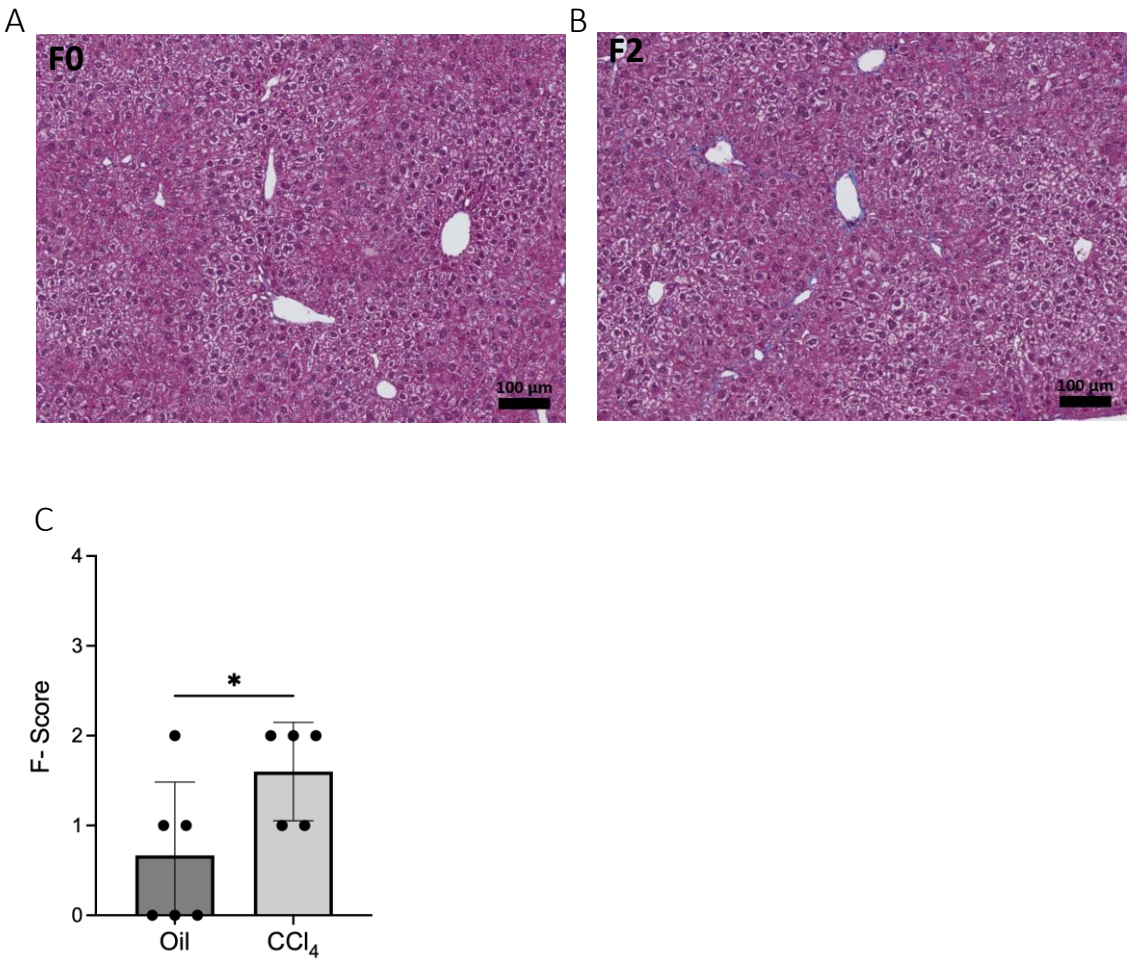

Figure 3: Moderate liver fibrosis is sustained following CCl_4 cessation.

After 16 weeks of treatment, CCl_4 administration was stopped for 4 weeks. Afterwards, animals were euthanized, and the right lobe of the liver collected for histology. Liver sections were formalin-fixed, paraffin embedded and sectioned, then stained with Masson's Trichrome stain. Fibrosis staging was determined using the METAVIR (F-score) scoring system. (A) Representative liver histology image for oil and (B) CCl_4 treated mice. (C) Summary of liver fibrosis scores in the cohort (n=11) 4 weeks post-CCl_4 cessation. Data are presented as group means ±SD and statistically significant differences were determined using a one-tailed unpaired Student's *t*-test (*$p \leq 0.05$).

3.1.3 $CD8^+$ T cell function in CCl_4 treatment

Generalized $CD8^+$ T cell hyperfunction is detected in HCV-infected individuals with advanced liver fibrosis, in which circulating $CD8^+$ T cells express elevated levels of perforin and IFN-γ[77]. A mouse model of hepatotoxin-induced liver disease was developed to mimic this HCV-induced cellular hyperfunction and liver pathology. Previous experiments have demonstrated that 12-16 weeks of CCl_4 treatment induces advanced liver fibrosis and $CD8^+$ T cell hyperfunction, characterized by an elevated proportion of IFN-γ^+ and $GrzB^+$ $CD8^+$ T cells[103]. We aimed to replicate these findings and leverage the CCl_4 model for further investigations into the mechanisms driving $CD8^+$ T cell hyperfunction.

At baseline and every subsequent 4 weeks, blood was collected from the lateral saphenous vein for the assessment of circulating $CD8^+$ T cell function. PBMCs were isolated from whole blood and cultured for 48 hours with anti-CD3/28 antibodies. In two independent experiments, flow cytometry analysis of bulk and subset $CD8^+$ T cells (Figures 4A-C) revealed that cellular function was unaffected by 16 and 21 weeks of CCl_4 treatment (Figure 4D and E). Furthermore, there were no significant differences in the proportion of $GrzB^+$ and IFN-γ^+ $CD8^+$ T cells between oil and CCl_4-treated animals at week 12; a time at which advanced liver fibrosis is expected. However, in E02, a transient elevation in GrzB expression ($p= 0.02$) was detected in CCl_4-treated males at week 18 (data not shown). Unfortunately, this difference did not persist, and differences did not arise in other experiments, even after prolonging treatment upwards of 16 weeks. Therefore, CCl_4-induced $CD8^+$ T cell hyperfunction was not replicated in this model, despite the induction of advanced liver fibrosis.

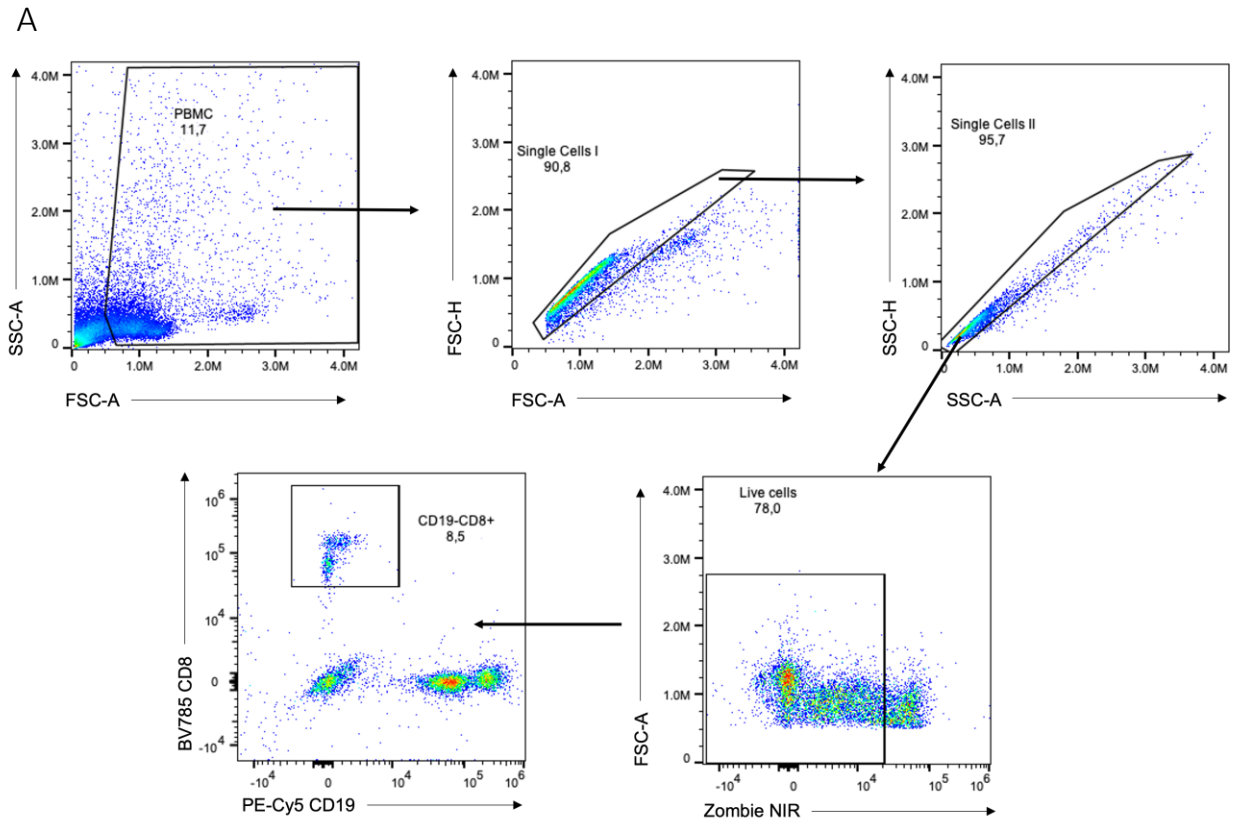
A
PBMC
11,7
SSC-A
FSC-A
Single Cells I
90,8
FSC-H
FSC-A
Single Cells II
95,7
SSC-H
SSC-A
CD19-CD8+
8,5
BV785 CD8
PE-Cy5 CD19
Live cells
78,0
FSC-A
Zombie NIR

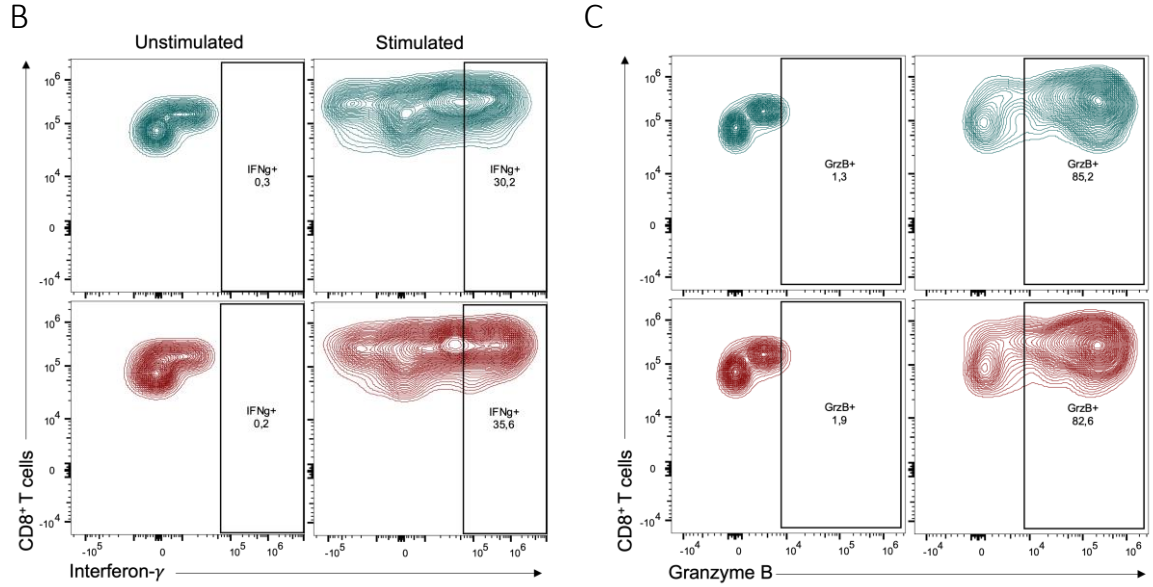
B
Unstimulated
Stimulated
IFNg+
0,3
IFNg+
30,2
IFNg+
0,2
IFNg+
35,6
CD8+ T cells
Interferon-γ
C
GrzB+
1,3
GrzB+
85,2
GrzB+
1,9
GrzB+
82,6
CD8+ T cells
Granzyme B

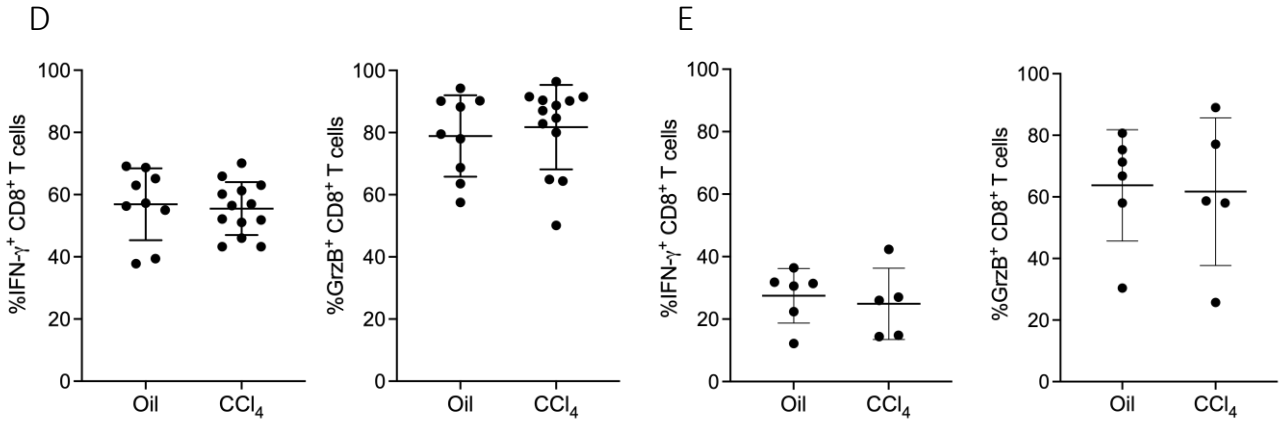

Figure 4: CD8$^+$ T cell function does not differ between oil and CCl_4 treated C57BL/6 mice after 16-21 weeks.

In two independent experiments, mice were treated with CCl_4 for 16-21 weeks. At regular intervals, whole blood PBMCs were stimulated for 48 hours with anti-CD3/28 antibodies and circulating CD8$^+$ T cell function was determined by flow cytometry. (A) The representative flow cytometry gating strategy for CD8$^+$ T cells, gating on PBMCs, single cells, live cells and CD19$^-$ CD8$^+$ cells. (B) Representative gating strategy of CD8$^+$ T cells expressing IFN-γ and (C) GrzB using unstimulated samples to set respective gates as shown. (D) The proportion of IFN-γ^+ and GrzB$^+$ CD8$^+$ T cells at week 21 of CCl_4 treatment (n=22). Data provided by Jiafeng Li (PhD candidate, Crawley Lab). (E) Proportion of IFN-γ^+ and GrzB$^+$ CD8$^+$ T cells at week 16 of treatment in a second independent experiment (n=11). Data are presented as group means ±SD and statistically significant differences were determined using a two-tailed unpaired Student's *t*-test.

3.1.4 $CD8^+$ T cell mitochondrial potential and reactive oxygen species

Mitochondrial potential and ROS can serve as indicators of disrupted cellular metabolism. Cells with elevated mitochondrial membrane potential are polarized and have a higher capacity to engage in OXPHOS and produce ATP[84]. Furthermore, excessive cellular ROS, a possible by-product of elevated mitochondrial potential, can be harmful when sustained for long periods of time, leading to numerous pathologies[114]. We aimed to determine if mitochondrial potential and ROS were elevated alongside $CD8^+$ T cell hyperfunction, providing the foundation for more in-depth analyses on disrupted metabolic processes in chronic liver disease.

$CD8^+$ T cell mitochondrial potential and ROS were evaluated by flow cytometry in CCl_4 treatment, alongside cellular function. In E02, at baseline and every subsequent 4 weeks, PBMCs were isolated and immediately stained with Mitotracker Deep Red and CellROX Green dyes (Figures 5A-C). Unsurprisingly, no significant differences between oil and CCl_4-treated animals in mitochondrial potential and ROS were apparent in the absence of $CD8^+$ T cell hyperfunction. However, the transient elevation in male GrzB expression in the CCl_4-treated group (section 3.2.2) was accompanied by a significant increase in mitochondrial potential (Figure 5D), indicative of a potential correlation between these readouts. Similar to function, this difference did not persist through the end of treatment, at week 21 (Figure 5E).

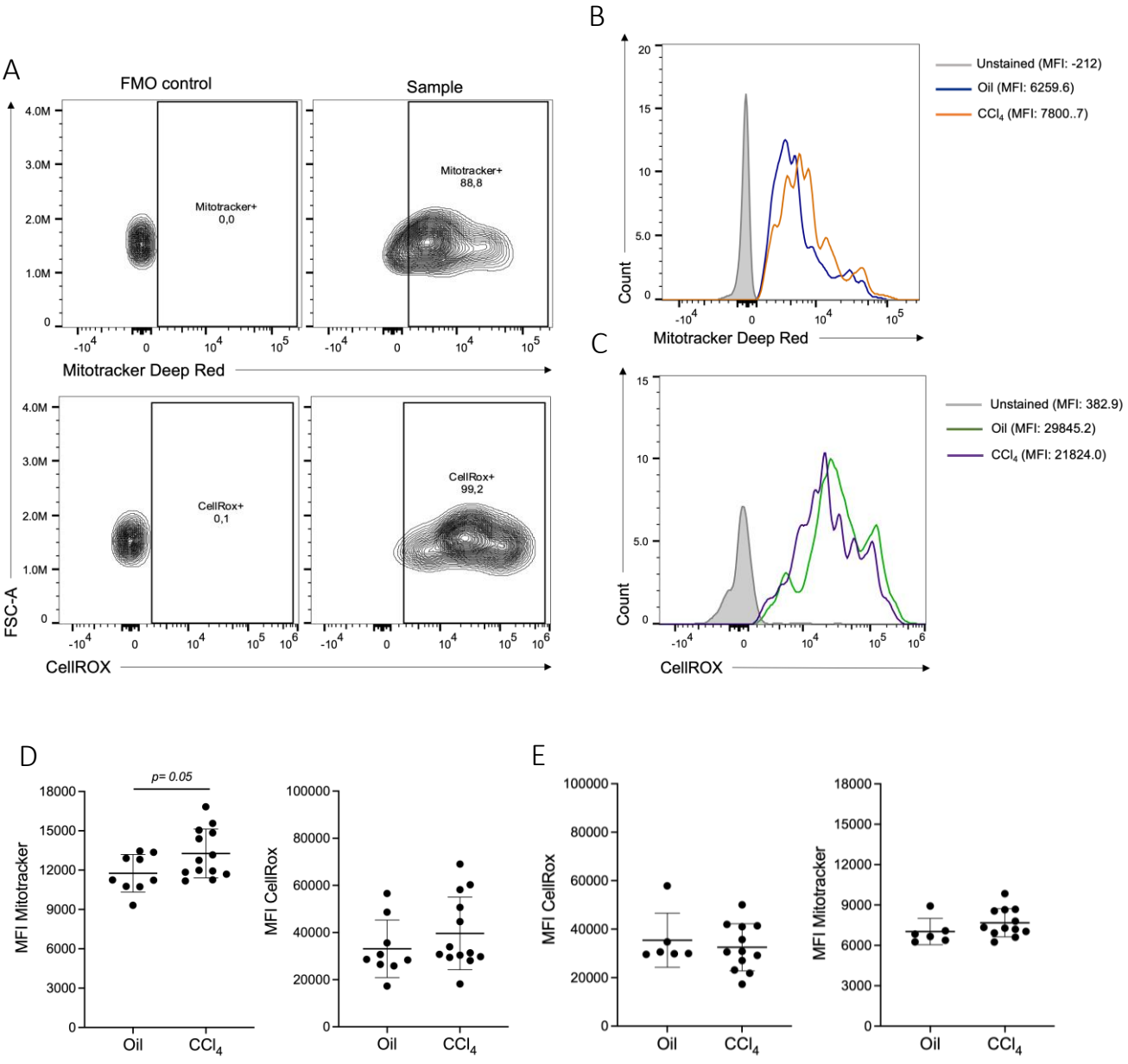

Figure 5: CD8⁺ T cell mitochondrial potential and ROS levels do not differ between oil and CCl_4-treated animals.

Isolated PBMCs were stained with Mitotracker Deep Red and CellROX green for the analysis of mitochondrial potential and ROS respectively, by flow cytometry. (A) The representative gating strategy for mitochondrial potential and reactive oxygen species using FMO controls as shown. (B) Comparison of Mitotracker Deep Red expression and (C) CellROX Green expression in oil and CCl_4-treated mice, and unstained controls. (D) The MFI of Mitotracker Deep Red and CellROX Green at weeks 18 and (E) 21 of treatment (n=22). Data are presented as group means ±SD and statistically significant differences were determined using a two-tailed unpaired Student's *t*-test.

3.1.5 $CD8^+$ T cell adoptive transfer

The Crawley lab has reported that in individuals with chronic HCV infection and advanced liver fibrosis, $CD8^+$ T cell hyperfunction persists even after viral clearance with DAA therapy[77]. This phenotype and pathology was replicated in C57BL/6 mice with CCl_4-induced liver fibrosis, in which cellular hyperfunction persisted post-treatment cessation despite liver tissue remodelling and fibrosis regression[103]. Therefore, the aim of these experiments was to determine if cellular hyperfunction, in an animal model of liver disease, would persist post-adoptive transfer into healthy recipients, removing cells from the fibrotic and inflammatory environment. To do so, it first needed to be determined if unstimulated $CD8^+$ T cells would persist post-adoptive transfer, using the OT-1 model. $CD8^+$ T cells were isolated from the spleens of healthy OT-1 CD45.2 C57BL/6 donors by negative magnetic bead selection and transferred by i.v. tail vein injection to CD45.1 recipients (Figure 6A). This congenic mouse model enables the use of CD45.1 and CD45.2 specific antibodies for tracking of donor and recipient $CD8^+$ T cells in whole blood by flow cytometry. Across various experiments, $5x10^4$ - $2x10^6$ isolated $CD8^+$ T cells were transferred into recipient animals, yielding similar results, in which donor cells could not be detected in whole blood one-week post-adoptive transfer (Figure 6B). Therefore, unstimulated $CD8^+$ T cells could not be followed post-adoptive transfer.

As an alternative study approach, *Listeria monocytogenes* conjugated ovalbumin (LM-OVA) was used to stimulate OT-1 $CD8^+$ T cells post-adoptive transfer, to promote their expansion and render this population detectable by flow cytometry. Even after i.v. challenge with LM-OVA, donor $CD45.2^+$ $CD8^+$ T cells in the blood and spleen of recipient animals one-week post-adoptive transfer were undetectable (data not shown). Therefore, genotype analysis was performed to confirm the presence of the transgenic inserts TCRα-V2 and TCRβ-V5 in these

experimental animals. These transgenes allow the specific recognition of ovalbumin peptide residues by $CD8^+$ T cells, enabling a targeted response to bacterial pathogens such as LM-OVA. This investigation revealed that almost all animals treated with CCl_4 did not carry these transgenes, and therefore would be unable to properly respond to LM-OVA challenge. Owing to these results, and the inability to reproduce $CD8^+$ T cell hyperfunction in the CCl_4 model, no additional adoptive transfer experiments were conducted.

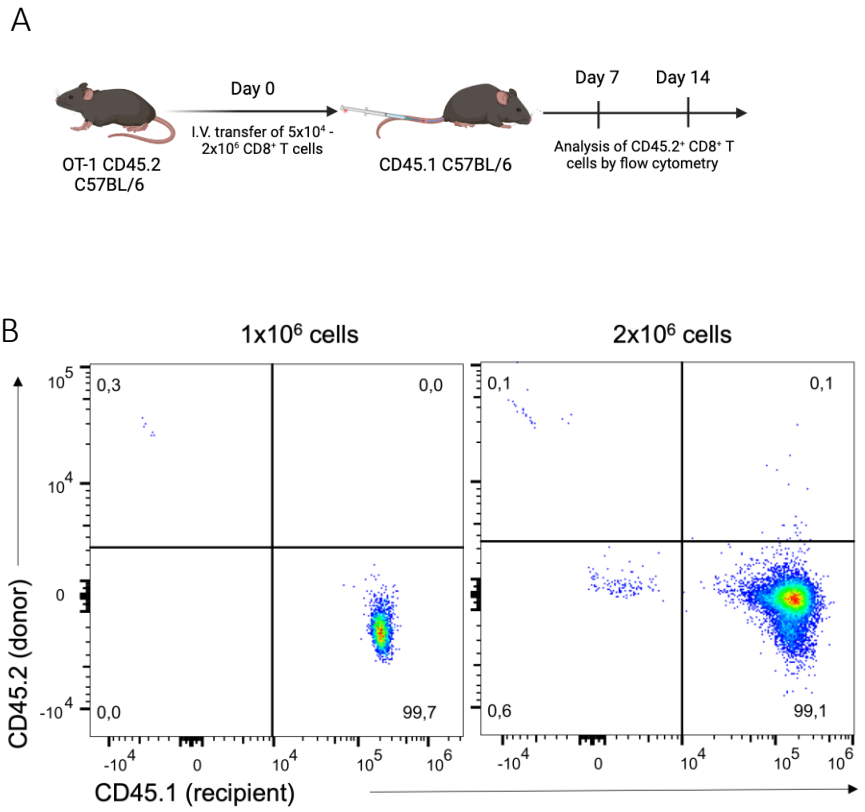

Figure 6: Unstimulated donor CD8$^+$ T cells do not persist post-adoptive transfer and are undetectable in the peripheral blood of recipient animals.

CD8$^+$ T cells were isolated from the spleens of donor OT-1 CD45.2 C57BL/6 mice and transferred intravenously by tail vein injection into CD45.1 recipients. One and two-weeks post-transfer, saphenous blood was collected from recipient animals to determine if donor cells were detectable by flow cytometry. (A) A schematic of the adoptive transfer experiments. (B) Representative flow cytometry density plots demonstrating the proportion of donor and recipient cells one-week post-adoptive transfer of 1x10^6 and 2x10^6 CD8$^+$ T cells.

3.2 The HFMCDD model of liver disease

3.2.1 The effect of the HFMCDD on body weight

C57BL/6 mice aged 8-10 weeks were fed a high-fat, methionine, and choline deficient diet (HFMCDD) composed of 60% kcals from fat, 0.1% methionine and no added choline. Meanwhile, controls were fed a standard chow diet composed of 18% fat, 0.4% methionine and 1200mg/kg of choline. Twelve weeks of HFMCDD-feeding has been shown to induce significant liver steatosis and moderate inflammation and fibrosis[101,102], replicating many pathologic features of human MASH. In this thesis, three groups of C57BL/6 mice: E01 (n=21 males; 9 control, 12 diet), E02 (n=19 females; 7 ctl, 12 diet) and E03 (n=24 males and females; 11 ctl, 13 diet) were placed on the HFMCDD *ad libitum* for 16-21 weeks to induce more robust liver disease and advanced liver fibrosis (Figure 7A).

Just as reported in the literature, HFMCDD and chow-fed animals maintained relatively similar body weights over the course of treatment. However, HFMCDD males in E01 exhibited a transient loss in weight after approximately 3 weeks of diet-feeding. This transient loss has been observed in other groups as well, in which animals quickly recover[99]. Interestingly, significant differences in body weight between E01 chow and HFMCDD males were observed as of week 4, in which control males gained significantly more weight than expected (Figure 7B). Unfortunately, these males had to be individually housed to prevent fighting resulting in life-threatening injuries due to their aggressive nature. It is likely that these males were less physically active than typically group-housed males, thus promoting excessive weight gain. The effect of individual housing and reduced physical activity was less pronounced in their HFMCDD counterparts as methionine restriction in the diet somewhat suppressed excessive weight gain, limited fat deposition, and increased fatty acid oxidation[101,115]. No significant

differences in body weight between chow and HFMCDD mice were detected in group-housed females (Figure 7C) or group-housed males (Figure 7D).

After 21 weeks, a subset of HFMCDD-fed animals in E01 and E02 were switched to a normal chow diet to examine liver injury regression. This 4-week regression period allowed for weight gain in the male HFMCDD group, removing the difference between chow and HFMCDD groups (Figure 7B). On the other hand, HFMCDD and chow females remain similar in weight throughout treatment and cessation periods (Figure 7C).

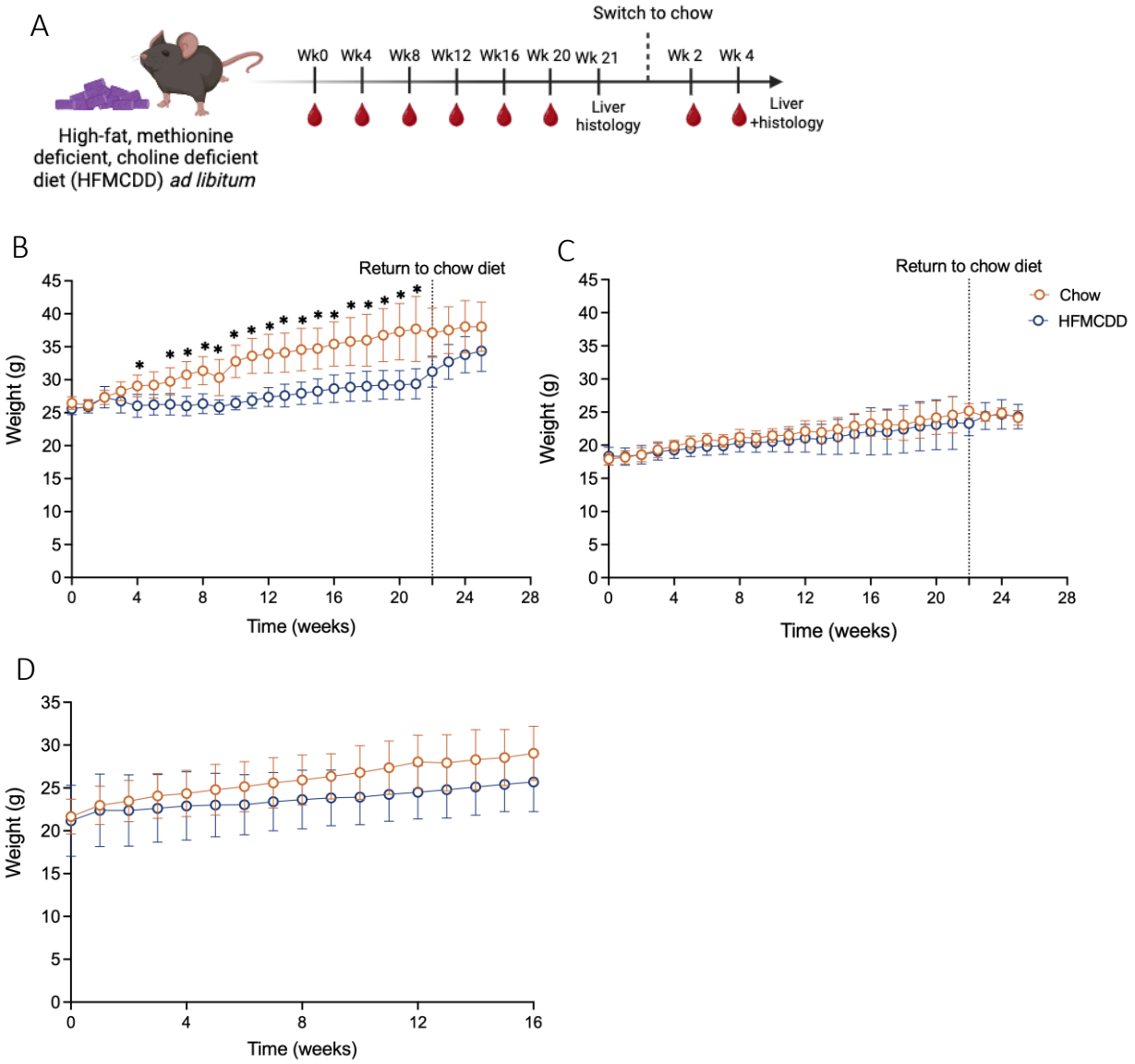

Figure 7: The HFMCDD model of liver disease.

(A) A schematic of the experimental design is shown. C57BL/6 mice aged 8-10 weeks were fed the HFMCDD *ad libitum* for 21 weeks. Blood was collected at baseline and every 4 subsequent weeks for analysis of $CD8^+$ T cell function, mitochondrial potential, and ROS by flow cytometry. At peak treatment, a subset of animals was euthanized for histology, while another group resumed a standard chow diet for a 4-week regression period. Liver sections were collected for histology in a subset of animals at peak liver injury and in another after the 4-week regression period. (B) Body weight gain in control and HFMCDD-fed mice through treatment and resuming the regular chow diet in individually housed males (n=21), (C) group housed females (n=19) and (D) group housed males (n=12). Data presented as group means ±SD. Statistically significant differences between groups were determined using a two-way ANOVA test (*$p \leq 0.05$).

3.2.2. The effect of HFMCDD feeding on organ weight

a. Organ weight at peak HFMCDD treatment

At endpoint, week 21, a subset of chow and HFMCDD animals were euthanized, and the livers and spleens harvested. As expected, HFMCDD livers were visibly larger and yellow in colour, indicative of fat deposition, while control livers were slightly pink (Figures 8A-D). Spleens were also visibly larger in HFMCDD mice (not pictured). In E01 males and E03 females, liver weight, % liver weight, spleen weight and % spleen weight were significantly higher in the HFMCDD group. On the other hand, in E02 females, significant differences only arose in the liver weight and % liver weight (Figures 8E-H). Finally, another cohort of females exhibited significant differences in all readouts (Supplemental Fig. 1), comparable to males. These trends mirror human MASLD, in which splenomegaly is variable and occurs in only a proportion of individuals with MAFLD/MASH[116].

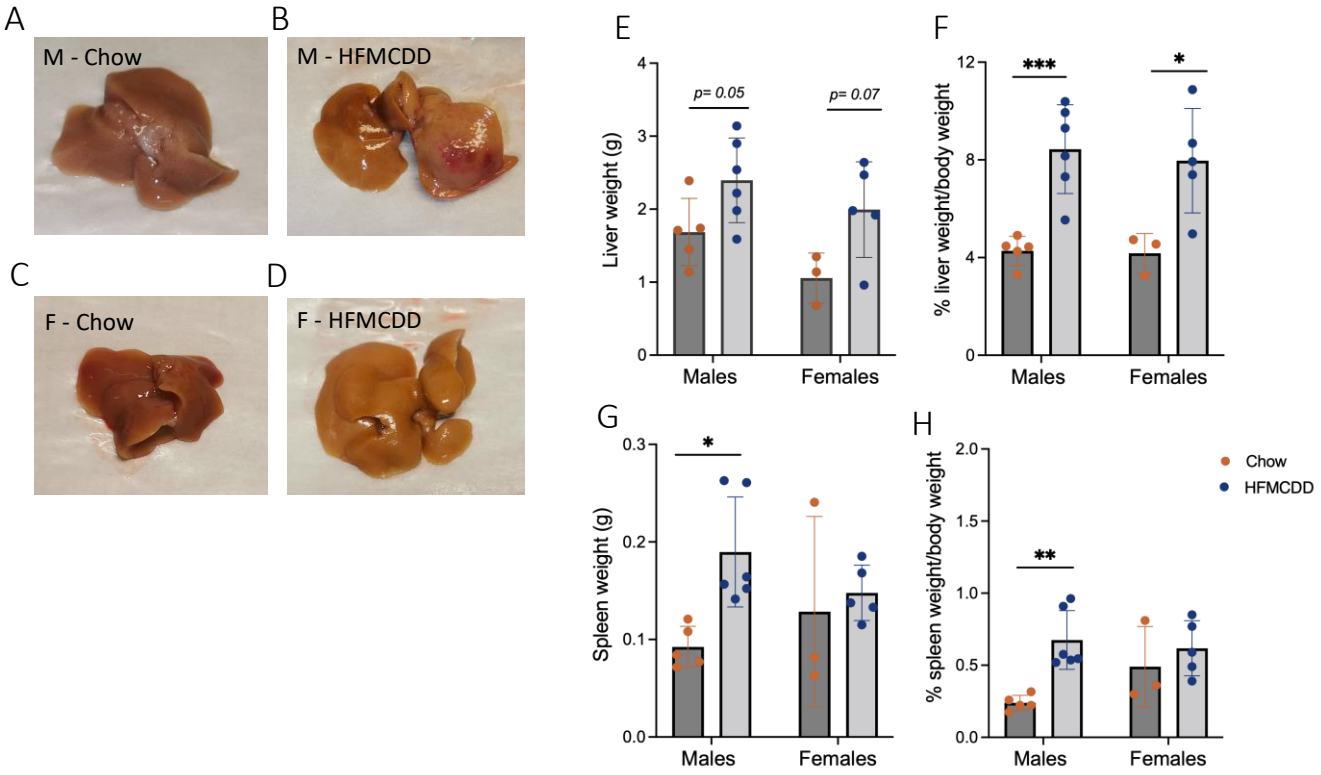

Figure 8: The spleen and liver are enlarged in HFMCDD-fed mice after 21 weeks.

After 21 weeks of HFMCDD feeding, mice were euthanized, and the spleens and livers harvested. (A) Representative liver images of a chow-fed male (fibrosis: 0 and steatosis: 1), (B) HFMCDD-fed male (fibrosis: 4 and steatosis: 3), (C) chow-fed female (fibrosis: 0, steatosis: 0) and (D) HFMCDD-fed female (fibrosis: 2, steatosis: 3). (E) Liver weight and (F) liver weight relative to total body weight in male and female C57BL/6 mice at peak treatment. (G) Spleen weight and (H) spleen weight relative to total body weight in males and females at peak treatment. Data presented as group means ±SD and statistically significant differences were determined using a two-tailed unpaired Student's *t*-test (*p≤0.05, **p≤0.01, ***p≤0.001).

b. Organ weight post-HFMCDD cessation

The remaining animals underwent liver injury regression, during which they were removed from the HFMCDD and returned to the normal chow diet for 4 weeks. After 4 weeks, animals were euthanized, and organs were harvested as previously described. Significant differences in liver weight, % liver weight, spleen weight and % spleen weight persisted in males, even after the recovery period. In females, a trend towards elevated liver weight (p=0.09) was observed and significant differences in all other organ measurements (Figures 9A-D).

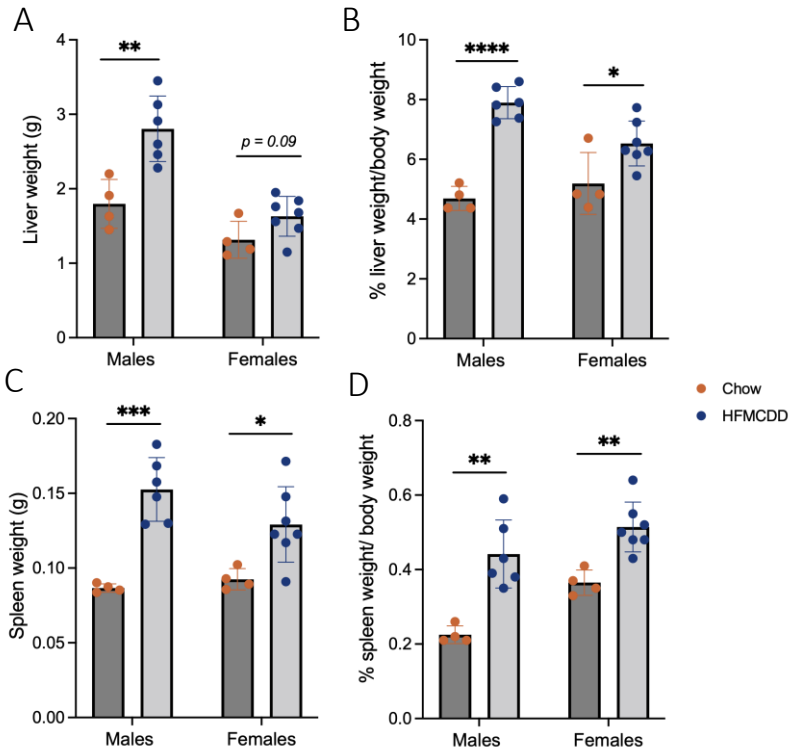

Figure 9: Spleen and liver weight remain elevated 4 weeks post-HFMCDD cessation.

After 4 weeks of regular chow feeding, animals were euthanized, and their spleens and livers harvested. (A) Liver weight and (B) liver weight relative to total body weight in males and females. (C) Spleen weight and (D) spleen weight relative to total body weight in males and females. Data presented as group means ±SD and statistically significant differences were determined using a two-tailed unpaired Student's *t*-test (*p≤0.05, **p≤0.01, ***p≤0.001, ****p≤0.0001).

3.2.3 HFMCDD-induced liver injury

a. *Liver injury at peak HFMCDD treatment*

After 17-21 weeks of HFMCDD-feeding, mice were euthanized for histological analyses as previously described. Liver sections were stained with both Masson's trichrome and H&E stains. Masson's trichrome allows for the visualization of fibrotic tissue while H&E allows for the visualization of steatosis, inflammation, and ballooning. The HFMCDD reliably induced advanced liver fibrosis, steatosis, inflammation, and ballooning. Further histological observations included many degenerated hepatocytes filled with bubbly yellow material and chicken-wire fibrosis (Figures 10A-D and 11A-D).

Most HFMCDD-fed males had advanced liver fibrosis (F4), advanced steatosis (stage 3), moderate inflammation and moderate/severe ballooning (Figure 10E). Interestingly, chow-fed males had more advanced steatosis than expected; half with stage 1 and one with stage 3 steatosis and exhibited low level inflammation and ballooning. The outlier with stage 3 steatosis also had the highest body weight at 49g, far surpassing the expected average of 36.7±3.7g for a male C57BL/6 mouse of that age (31 weeks)[117]. The accumulation of steatosis in the chow-fed controls may be attributed to their abnormal weight gain and reduced physical activity resulting from individual housing. Despite the presence of liver steatosis in controls, a significant increase in the HFMCDD group could still be detected (Figure 10E). On the other hand, HFMCDD-fed females had less severe liver injury, with moderate fibrosis (F2-3), advanced steatosis (stage 3), minimal inflammation and moderate/severe ballooning (Figure 11A-D). HFMCDD-fed females had significantly elevated fibrosis, steatosis, and ballooning in comparison to their chow counterparts (Figure 11E). Unlike males, chow-fed females did not have any steatosis and exhibited low level inflammation and ballooning. These females were housed in groups and very

closely resembled the weight expected for C57BL/6 females of this age. Similar findings were observed in another independent experiment, in which males and females were treated for 17 weeks (Supplemental Fig.2). These findings somewhat parallel the notable sex differences that exist in human MASLD and MASH, driven by differences in estrogens. Males tend to have more severe liver injury, increased pro-inflammatory cytokine production and higher prevalence of HCC[37–39]. Similar trends were observed in the pathology of HFMCDD-induced liver injury, in which males had elevated mean fibrosis ($p=0.07$) and inflammation scores compared to females, although not statistically significant (Figure 11F).

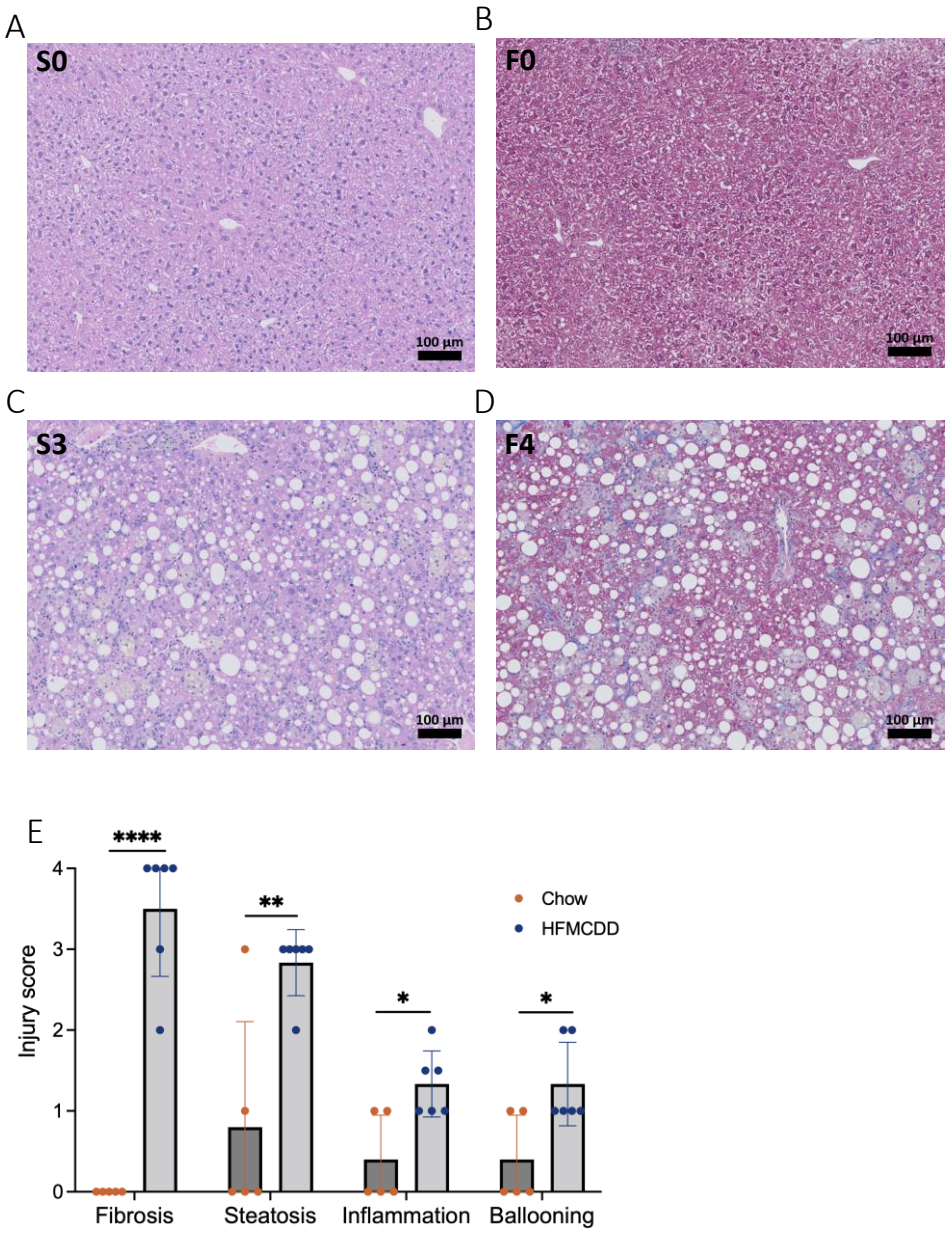

Figure 10: HFMCDD feeding induces advanced liver fibrosis with steatosis, inflammation, and ballooning after 21 weeks in males.

At peak treatment, a subset of animals (n=11) was euthanized, and liver samples were collected for histology. Liver sections were formalin-fixed, sectioned and stained with Masson's Trichrome (fibrosis) and H&E (steatosis, inflammation, and ballooning). (A) Representative liver section images of H&E-stained chow, (B) Masson's Trichrome stained chow, (C) H&E stained HFMCDD and (D) Masson's trichrome stained HFMCDD animals. (E) Liver fibrosis, steatosis, inflammation and ballooning scores in chow and HFMCDD-fed males at peak treatment. Data presented as group means ±SD and statistically significant differences were determined using a two-tailed unpaired Student's *t*-test (*p≤0.05, **p≤0.01, ***p≤0.001).

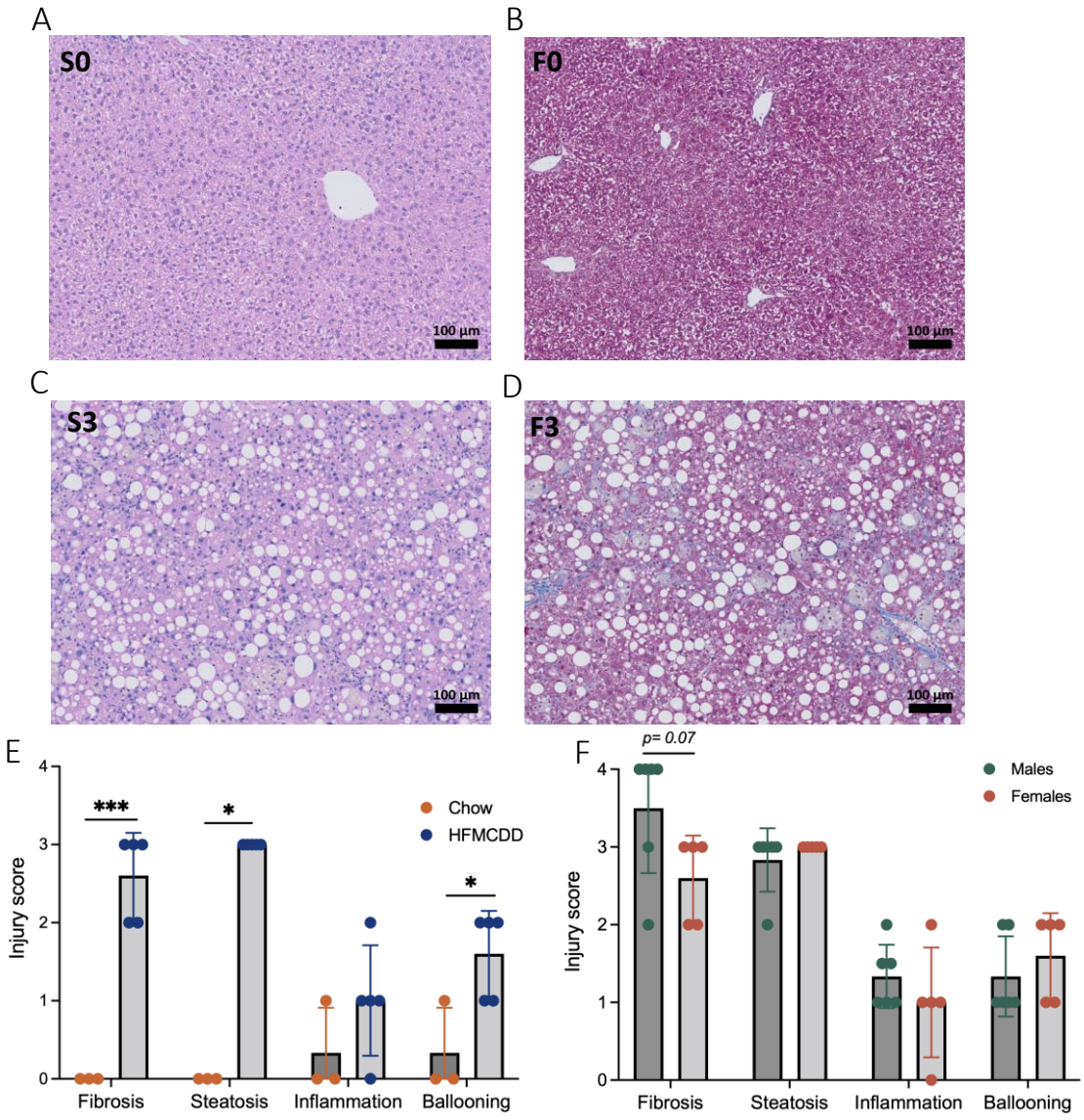

Figure 11: HFMCDD feeding induces liver fibrosis, steatosis, inflammation, and ballooning after 21 weeks in females.

At peak treatment, a subset of animals (n=8) was euthanized, and liver samples were collected for histology. Liver sections were formalin-fixed, sectioned and stained with Masson's Trichrome (fibrosis) and H&E (steatosis, inflammation, and ballooning). (A) Representative liver section images of H&E-stained chow, (B) Masson's Trichrome stained chow, (C) H&E stained HFMCDD and (D) Masson's trichrome stained HFMCDD animals. (E) Liver fibrosis, steatosis, inflammation and ballooning scores in chow and HFMCDD-fed females at peak treatment. (F) Sex differences in liver injury scores in HFMCDD-fed males and females at peak treatment. Data presented as means ±SD and statistically significant differences were determined using a two-tailed unpaired Student's *t*-test (*p≤0.05, ***p≤0.001). Significant differences in figure E steatosis were determined using the Mann-Whitney U test (*p≤0.05).

b. Liver injury regression post-HFMCDD cessation

After 21 weeks, animals underwent a 4-week regression period, during which they were removed from the HFMCDD and placed on a regular chow diet. After regression, livers were harvested for histological analyses as previously described. Interestingly, liver fibrosis scores in these animals were similar to those at peak treatment, in which males had ~F3 fibrosis and females had F2-3 fibrosis (Figures 12A and B). On the other hand, HFMCDD cessation eliminated liver steatosis (stage 0) in females and reduced steatosis to control level in males (stage 0-1). In males, inflammation and ballooning also decreased significantly (Figure 12C), while these values did not change in females (Figure 12D). Although males exhibited more severe liver injury in HFMCDD treatment, females were more resistant to liver remodelling in terms of fibrosis regression. In humans, there is evidence that liver fibrosis regression, following the removal of liver insult (i.e. viral hepatic infection), is impaired in post-menopausal females[118]. Estrogens are not only protective against liver fibrosis progression but appear to play a role in successful tissue remodelling. At the end of this experiment, the 31-week old female mice were approaching menopause, which begins at approximately 36 weeks of age[119]. Declining estrogens associated with pre-menopause could have potentially contributed to delayed liver remodelling in these females. These findings mirror those in HCV-infected patients, in which DAA treatment fails to or minimally reverses advanced liver fibrosis, despite the removal of liver insult[123].

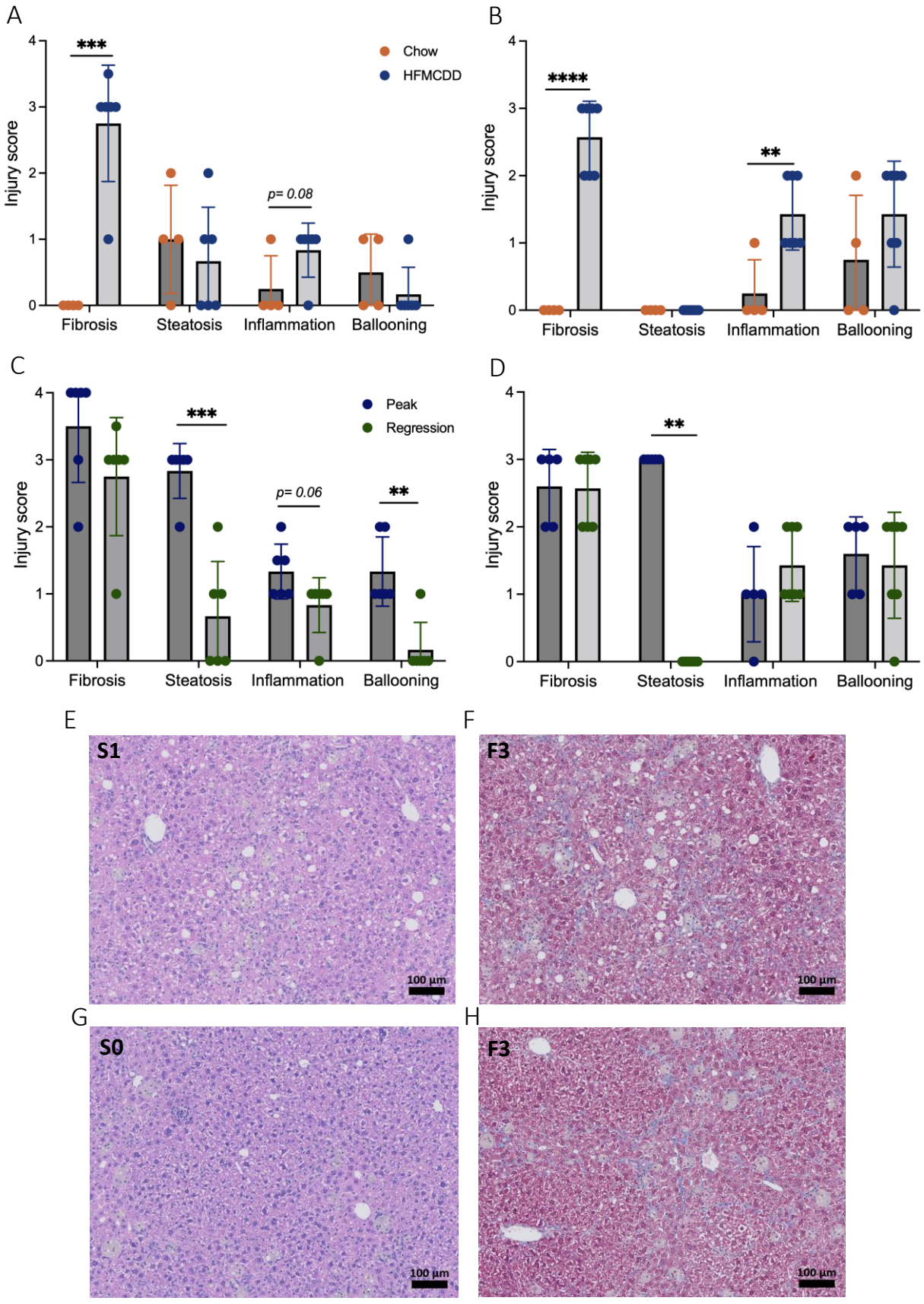
A
B
C
D
E
F
G
H
Injury score
Chow
HFMCDD
Peak
Regression
Fibrosis
Steatosis
Inflammation
Ballooning
***
****
**
p= 0.08
p= 0.06
S1
S0
F3
100 µm

Figure 12: Liver steatosis is reversed post HFMCDD-cessation and 4 weeks of regular chow feeding, while liver fibrosis is persistent.

After 21 weeks of HFMCDD feeding *ad libitum*, animals were resumed on the regular chow diet for 4 weeks. After this period, animals were euthanized, and liver sections were collected for histology. (A) Liver fibrosis, steatosis, inflammation, and ballooning scores in males (n=10) and (B) females (n=11) after 4 weeks of normal chow feeding. (C) Comparison of liver injury scores in animals at peak treatment and those that underwent the 4-week regression period in males and (D) females. (E)&(F) Representative male liver histology images stained with H&E and Masson's Trichrome, respectively. (G)&(H) Representative female liver histology images stained with H&E and Masson's Trichrome, respectively. Data presented as means ±SD and statistically significant differences were determined using a two-tailed unpaired Student's *t*-test (**p≤0.01, ***p≤0.001, ****p≤0.0001). Differences in figure D steatosis were determined using the Mann-Whitney U test (*p≤0.05).

3.2.4 $CD8^+$ T cell function in HFMCDD-feeding

a. $CD8^+$ T cell function with progressive HFMCDD-induced liver injury

At baseline and every subsequent 4 weeks, blood was collected from the lateral saphenous vein. PBMCs were then isolated from whole blood by red blood cell lysis, for functional analysis of circulating $CD8^+$ T cells (Figure 13A-C). In males, analyses revealed a significant increase in the proportion of bulk IFN-γ^+ cells and bulk, T_{CM} and T_{EM} $GrzB^+$ $CD8^+$ T cells in the HFMCDD group after only 4 weeks of feeding (Figures 13D-G). This is a time at which advanced liver steatosis (~stage 3) with very minimal liver fibrosis (F0-1) would be expected[99]. Hyperfunction was transiently lost at week 12, and subset specific analyses revealed that the HFMCDD group had a significantly lower proportion of T_{CM} and T_{EM} IFN-γ^+ $CD8^+$ T cells (not shown). Hyperfunction in GrzB was regained at week 16, in bulk $CD8^+$ T cells, while elevated IFN-γ expression was regained at week 20, in both bulk and T_{CM} cells. Cellular hyperfunction persisted until the end of treatment, at week 21 (Figures 13A-G).

In females, a significant increase in the proportion of $GrzB^+$ $CD8^+$ T cells and an increased trend in IFN-γ ($p=0.07$) HFMCDD-fed animals was observed after 8 weeks of feeding (Figures 14A and B). They also exhibited an upwards trend in T_{CM} and $T_{E/EM}$ $GrzB^+$ $CD8^+$ T cells at week 8 (Figure 14D), although no differences were seen in IFN-γ in these cell subsets (Figure 14C). However, $CD8^+$ T cell functional analyses could not be performed at week 4, and conclusions cannot be made regarding the time at which cellular hyperfunction emerged in this cohort. Significant differences between chow and HFMCDD groups persisted to the end of treatment (Figures 14A and B), as females did not exhibit transient loss of hyperfunction at week 12 as seen in males.

To validate these observations, $CD8^+$ T cell function was evaluated in a third cohort (E03) of both male and female C57BL/6 mice. In males, the HFMCDD group had an elevated proportion of IFN-γ^+ $CD8^+$ T cells after 4 weeks of HFMCDD-feeding (Supplemental Fig. 3A and B), while females had an elevated proportion of IFN-γ^+ $CD8^+$ T cells and a trend towards increased GrzB ($p=0.06$) at 4 weeks (Supplemental Fig. 3C and D). These differences in IFN-γ were transiently lost in males and regained at week 16. On the other hand, differences were lost at week 16 in females, and cellular hyperfunction was not present at endpoint. Additional experiments would be required to demonstrate conclusive sex differences in $CD8^+$ T cell function.

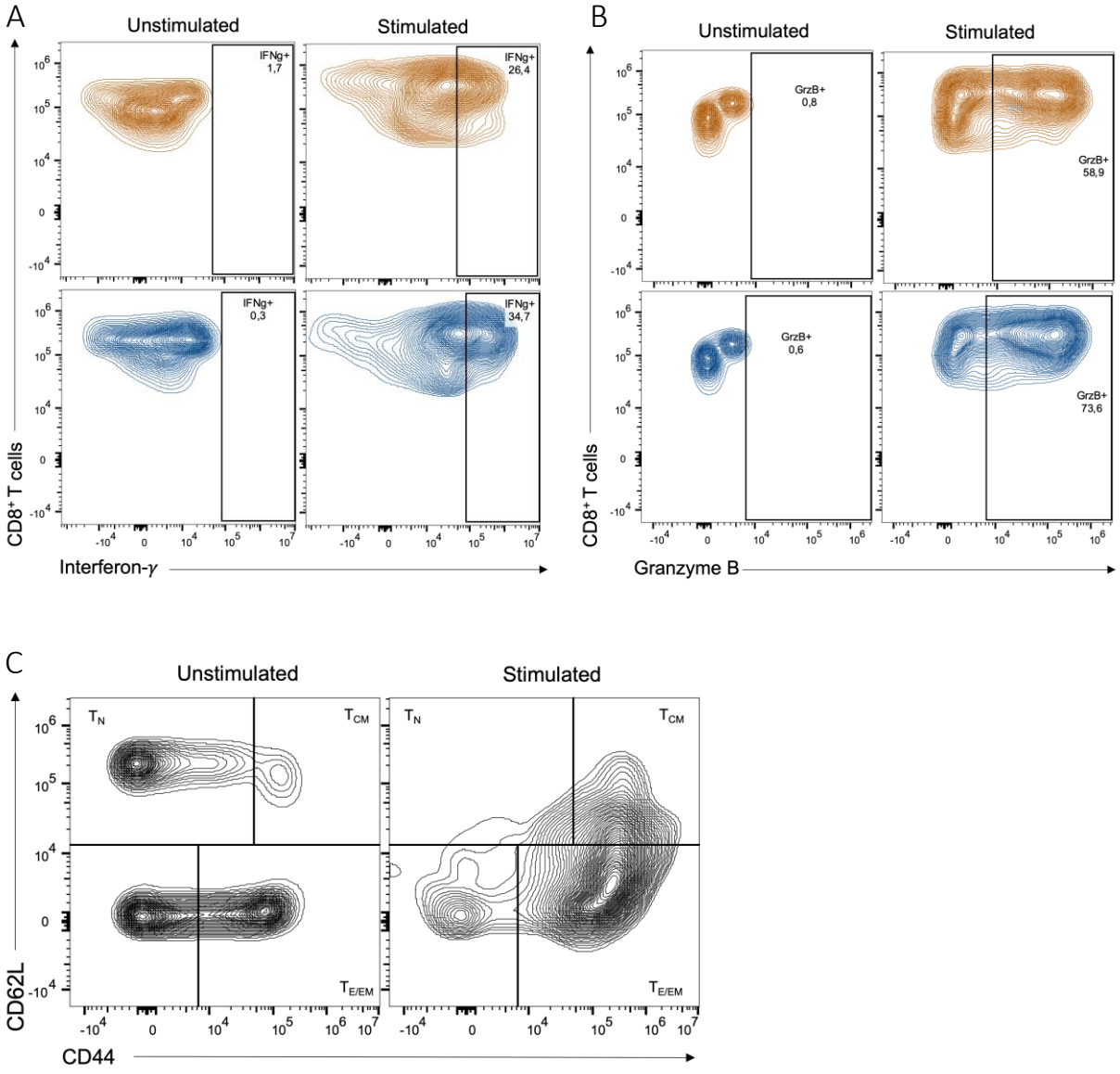
A
Unstimulated
Stimulated
IFNg+
1,7
IFNg+
26,4
IFNg+
0,3
IFNg+
34,7
CD8+ T cells
Interferon-γ
B
Unstimulated
Stimulated
GrzB+
0,8
GrzB+
58,9
GrzB+
0,6
GrzB+
73,6
CD8+ T cells
Granzyme B
C
Unstimulated
Stimulated
TN
TCM
TE/EM
CD62L
CD44

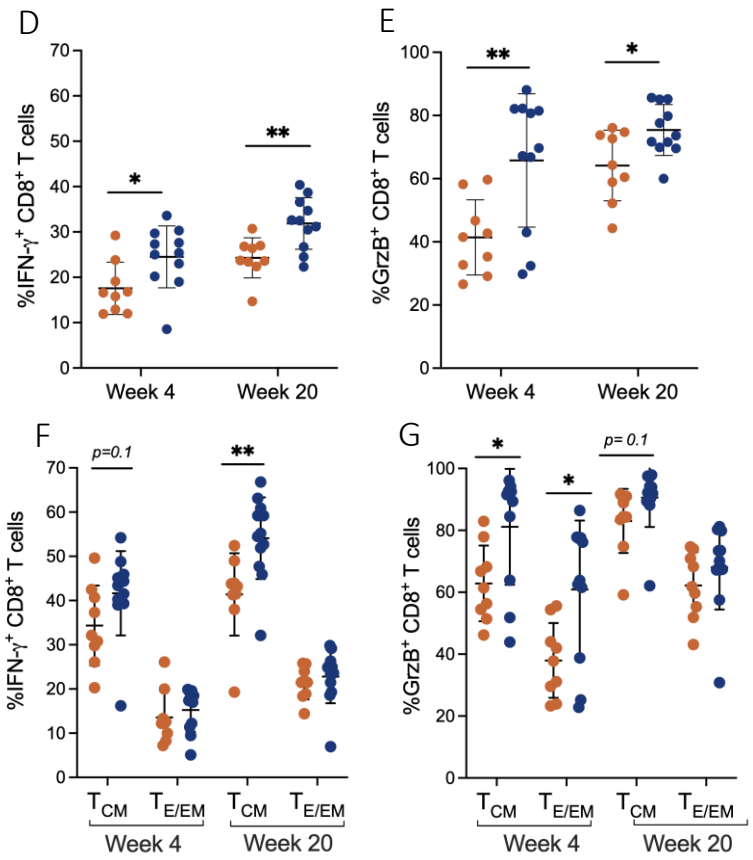

Figure 13: CD8$^+$ T cell hyperfunction is evident after 4 weeks of HFMCDD-feeding in males and is sustained through treatment.

PBMCs were stimulated for 48 hours with anti-CD3/28 antibodies for functional analysis of circulating CD8$^+$ T cells. (A) The representative gating strategy of CD8$^+$ T cells expressing IFN-γ and (B) GrzB, using unstimulated samples to set respective gates as shown. (C) Representative gating strategy for CD8$^+$ T cell subsets. Using CD44 and CD62L markers, naïve (CD44$^-$CD62L$^+$, T_N), central memory (CD44$^+$CD62L$^+$, T_{CM}) and effector/ effector memory (CD44$^+$CD62L$^-$, $T_{E/EM}$) CD8$^+$ T cells were distinguished. (D) Proportion of IFN-γ^+ and (E) GrzB$^+$ CD8$^+$ T cells after 4 weeks of treatment and at peak treatment. (F) Proportion of IFN-γ^+ and (G) GrzB$^+$ central memory (T_{CM}) and effector/ effector memory ($T_{E/EM}$) CD8$^+$ T cells at weeks 4 and 20 of treatment. Data presented as group means ±SD. Statistically significant differences were determined using a two-tailed unpaired Student's *t*-test (*p≤0.05, **p≤0.01).

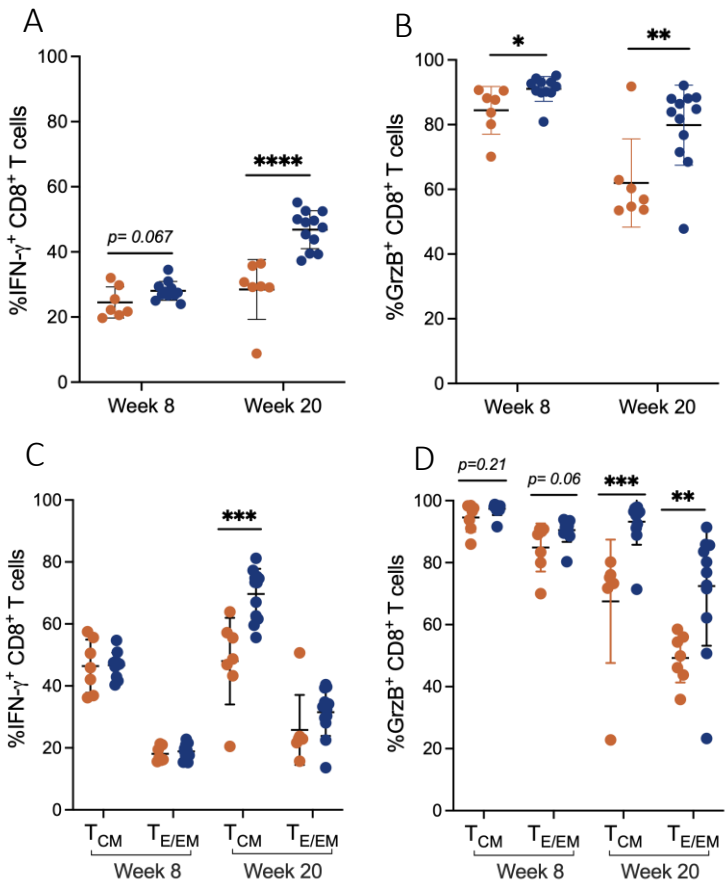

Figure 14: CD8$^+$ T cell hyperfunction is evident after 8 weeks of HFMCDD-feeding in females and is sustained through treatment.

PBMCs were stimulated for 48 hours with anti-CD3/28 antibodies for functional analysis of circulating CD8$^+$ T cells. (A) Proportion of IFN-γ^+ and (B) GrzB$^+$ CD8$^+$ T cells after 8 and 20 weeks of treatment. (C) Proportion of IFN-γ^+ and (D) GrzB$^+$ central memory (T_{CM}) and effector/ effector memory ($T_{E/EM}$) CD8$^+$ T cells at weeks 8 and 20 of treatment. Data presented as group means ±SD and statistically significant differences were determined using a two-tailed unpaired Student's *t*-test (*p≤0.05, **p≤0.01, ***p≤0.001).

b. $CD8^+$ T cell function post-HFMCDD cessation

After 21 weeks of HFMCDD feeding, a subset of animals was randomly selected for liver injury regression experiments. These groups, 10 males (4 ctl, 6 HFMCDD) and 11 females (4 ctl, 7 HFMCDD), were returned to a regular chow diet for 4 weeks. Blood was collected at weeks 2 and 4 post-diet cessation for the analysis of circulating $CD8^+$ T cell function. Despite significant differences in IFN-γ and GrzB expression in the E01 male cohort at week 20 (Figure 13), the mice randomly selected for diet-cessation experiments did not differ significantly, and only a trend towards increased IFN-γ (p=0.06) was observed. After 2 and 4 weeks on a regular chow diet, there was no difference in $CD8^+$ T cell function between control and HFMCDD-fed mice. This may be explained by the lack of significant hyperfunction at peak treatment in the mice randomly selected for regression (Figure 15A).

In E02 females, there was a significant difference in IFN-γ^+ $CD8^+$ T cells, but not GrzB, in the HFMCDD group of regression mice. After 2 weeks on a regular chow diet, there was a trend of increased IFN-γ, although not statistically significant (p=0.09), and a significant increase in GrzB expression. However, after 4 weeks, there is a significant decrease in the proportion of IFN-γ^+ $CD8^+$ T cells in the HFMCDD group, and no difference in GrzB (Figure 15B). Therefore, in males and females, $CD8^+$ T cell hyperfunction did not persist 4 weeks post-HFMCDD cessation, despite sustained liver fibrosis. Liver steatosis was rapidly reversed to control levels, potentially contributing to this lack of hyperfunction.

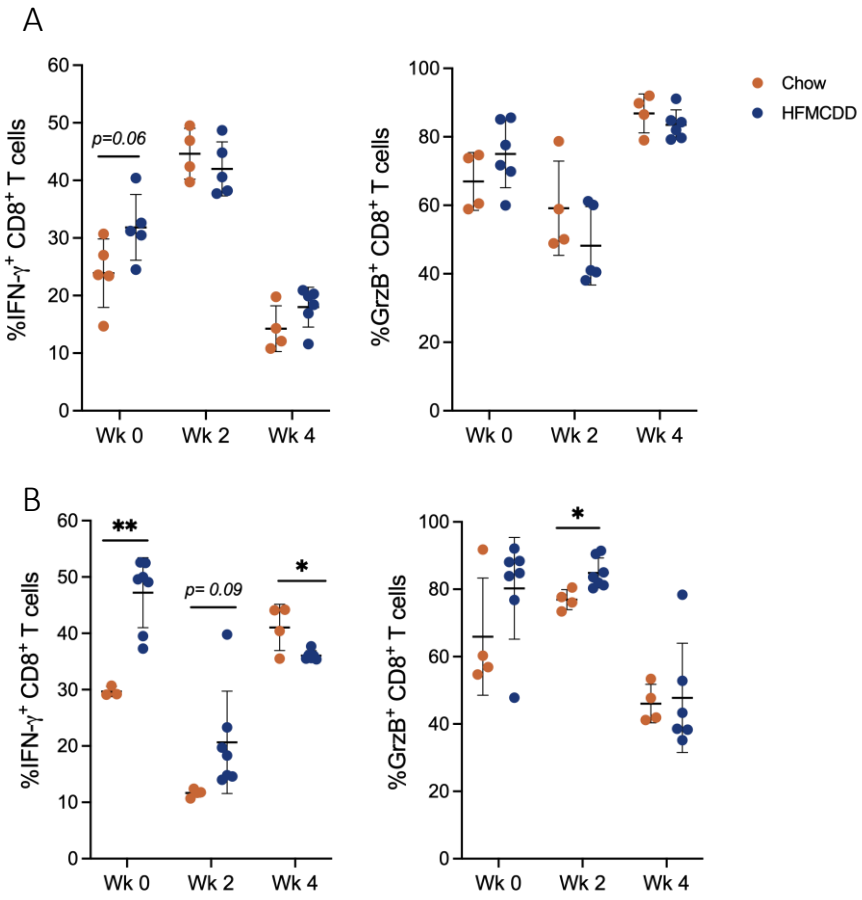

Figure 15: CD8$^+$ T cell hyperfunction does not persist post-HFMCDD cessation with liver steatosis regression.

At peak treatment, HFMCDD-fed animals resumed a normal chow diet for 4 weeks. Every 2 weeks post-diet cessation, saphenous blood was collected to evaluate circulating CD8$^+$ T cell function by flow cytometry. Isolated PBMCs were stimulated with anti-CD3/28 antibodies for 48 hours. (A) Proportion of IFN-γ^+ and GrzB$^+$ CD8$^+$ T cells at weeks 0, 2 and 4 post-HFMCDD cessation in males (n=10) and (B) females (n=11). Data presented as group means ±SD and statistically significant differences were determined using a two-tailed unpaired Student's *t*-test (*p≤0.05, **p≤0.01).

3.2.5 $CD8^+$ T cell mitochondrial potential and ROS in HFMCDD-induced liver disease

a. $CD8^+$ T cell mitochondrial fitness at peak HFMCDD treatment

At baseline and every subsequent 4 weeks, PBMCs were isolated from whole blood and immediately assessed for their $CD8^+$ T cell mitochondrial potential and ROS activity by flow cytometry (Figure 16A-B). In males, differences between the chow and HFMCDD groups appeared to be transient: cellular ROS activity was elevated at week 4, the same time at which cellular hyperfunction was observed and when advanced steatosis with minimal liver fibrosis is expected[102]. This persisted until week 12, after which significant differences between groups were no longer apparent by these measures (Figure 16D). Meanwhile, $CD8^+$ T cell mitochondrial potential, an indicator of cellular ATP production, was trending upwards in the HFMCDD group at weeks 8 ($p=0.06$) (Figure 16C) and 16 ($p=0.07$). Interestingly, no significant differences emerge through the entire treatment period. It was hypothesized that mitochondrial potential would be upregulated in hyperfunctional cells, as elevated cellular respiration may drive elevated effector functions. Therefore, in males, it can be concluded that hyperfunction is associated with an increase in cellular ROS, followed by an increasing trend in mitochondrial potential, although these differences are not sustained. Meanwhile, in females, no significant differences were observed in either mitochondrial potential or ROS over the treatment period (Figure 17), despite cellular hyperfunction.

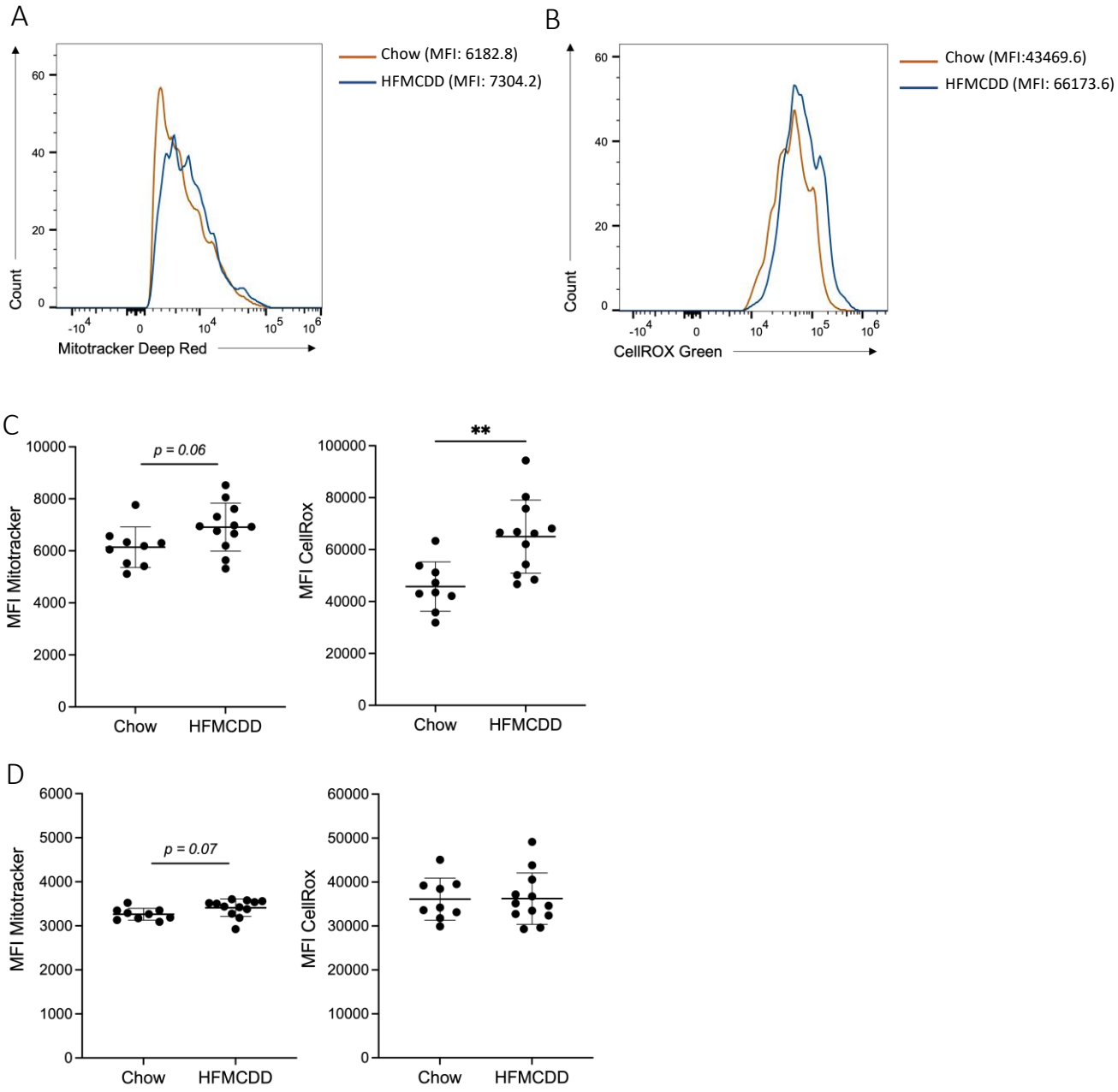

Figure 16: CD8$^+$ T cell mitochondrial potential and ROS are transiently elevated in HFMCDD-fed males.

Freshly isolated PBMCs were stained with Mitotracker Deep Red and CellROX Green for CD8$^+$ T cell metabolic analysis by flow cytometry. (A) Representative expression of Mitotracker Deep Red and (B) CellROX Green in chow and HFMCDD-fed mice at week 8 of treatment. (C) Mitotracker Deep Red and CellROX Green MFI at weeks 8 and (D) 16 of treatment. Data presented as group mean ±SD and statistically significant differences were determined using a two-tailed unpaired Student's *t*-test (**p≤0.01).

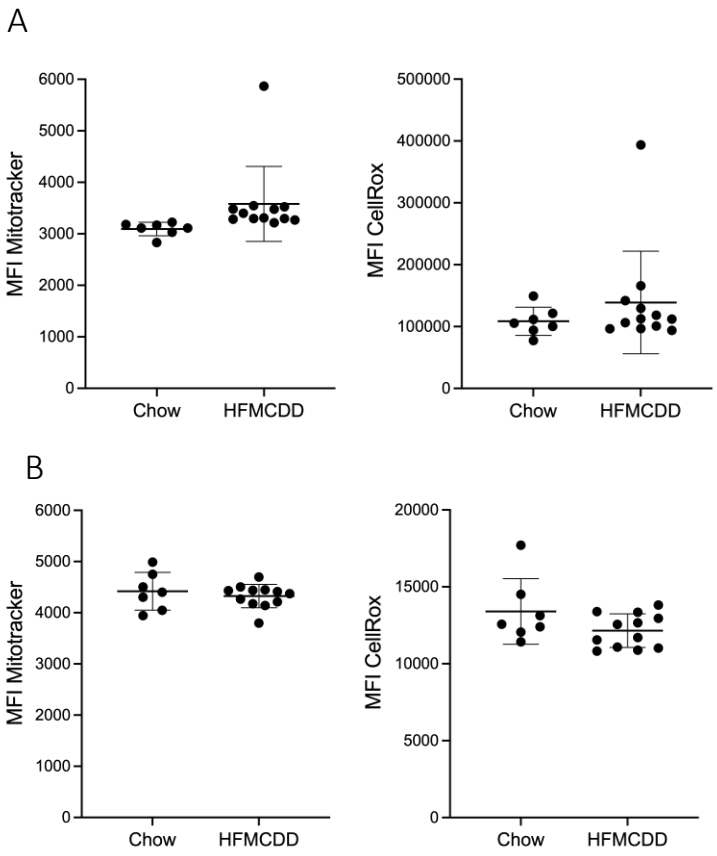

Figure 17: CD8$^+$ T cell mitochondrial potential and ROS do not differ between chow and HFMCDD-fed females.

Freshly isolated PBMCs were stained with Mitotracker Deep Red and CellROX green for CD8$^+$ T cell metabolic analysis by flow cytometry. (A) Mitotracker Deep Red and CellROX Green MFI at weeks 8 and (B) 20 of treatment. Data presented as group means ±SD and statistically significant differences were determined using a two-tailed unpaired Student's *t*-test.

b. $CD8^+$ T cell mitochondrial fitness post-HFMCDD cessation

After 21 weeks, animals were returned to a regular chow diet for liver injury regression. Two and four weeks post-HFMCDD cessation, $CD8^+$ T cell mitochondrial potential and ROS were evaluated in whole blood PBMCs as previously described. Unsurprisingly, in the absence of cellular hyperfunction, no significant differences in mitochondrial potential and ROS were observed after HFMCDD cessation in males (Figures 18A and B). In females, despite elevated IFN-γ and GrzB expression at week 2, and elevated IFN-γ expression at week 4 (Figure 15), changes in the mitochondrial potential or ROS were not detected (Figures 18 C and D). Therefore, the absence of an association between hyperfunction and these metabolic measures persisted throughout the experiment.

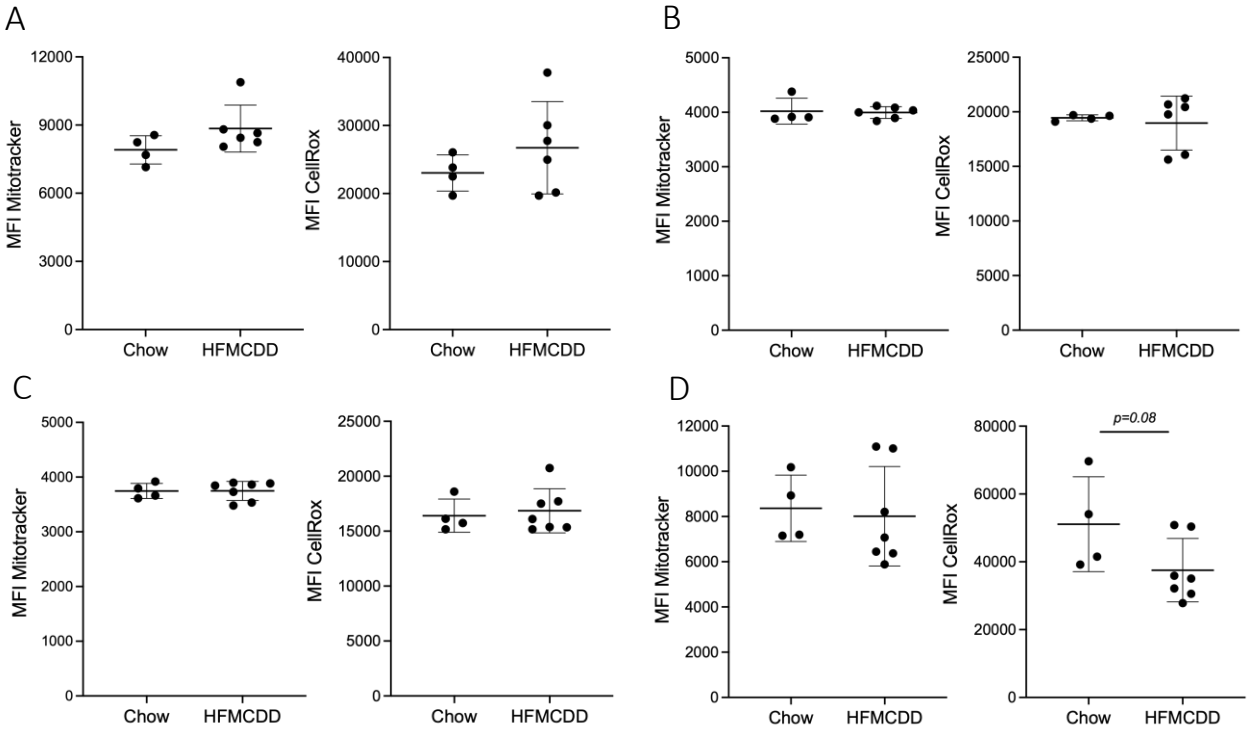

Figure 18: CD8$^+$ T cell mitochondrial potential and ROS do not differ between chow and HFMCDD-fed males and females post-diet cessation.

Freshly isolated PBMCs were stained with Mitotracker Deep Red and CellROX green for CD8$^+$ T cell metabolic analysis by flow cytometry. (A) MFI of Mitotracker Deep Red and CellROX Green in males 2 and (B) 4 weeks post-HFMCDD cessation. (C) MFI of Mitotracker Deep Red and CellROX Green in females 2 and (D) 4 weeks post-HFMCDD cessation. Data presented as group means ±SD and statistically significant differences were determined using a two-tailed unpaired Student's *t*-test.

3.2.6. $CD8^+$ T cell mitochondrial respiration and glycolysis at peak liver injury

Animals in E01 (males) and E02 (females) were randomized into two groups; one of which was euthanized for Seahorse XF metabolic analysis at peak HFMCDD treatment, and the other for the examination of $CD8^+$ T cell function, mitochondrial potential, and ROS post-diet cessation as described above. The Seahorse XF Analyzer quantifies cellular OCR and ECAR, indicators of mitochondrial respiration and glycolysis, respectively. Readouts are obtained after the input of various compounds into wells of isolated $CD8^+$ T cells: oligomycin, FCCP, rotenone/antimycin A and monensin, each providing distinct information on cellular respiration.

a. $CD8^+$ T cell respiration and glycolysis in males

There were no significant differences in the OCR (Figures 19B-D) and ECAR (Figures 19I-K) between control and HFMCDD males, including in baseline, maximal and spare capacity readouts. However, a trending increase in the male HFMCDD group was observed in the proton leak ($p=0.1$) (Figure 19E), a potential indicator of mitochondrial damage. $CD8^+$ T cell energy phenotype profiles also demonstrate that both chow and HFMCDD animals transitioned from an aerobic, primarily utilizing OXPHOS, to energetic states, utilizing both OXPHOS and glycolysis, following metabolic challenge (Figure 19L). It is important to note that in this group, an insufficient number of $CD8^+$ T cells were isolated to plate the standard number of technical replicates (6-8) per animal. Therefore, this experiment was repeated in a second cohort of C57BL/6 males, which yielded similar results. In E03 males, there were no significant differences between the chow and HFMCDD groups in basal or maximal ECAR and OCR. There was, however, a trending increase in the basal OCR ($p=0.07$) and significant elevation in

non-mitochondrial respiration (Supplemental Fig. 4), a measure of respiration that is not coupled to ATP production and a potential indicator of mitochondrial damage.

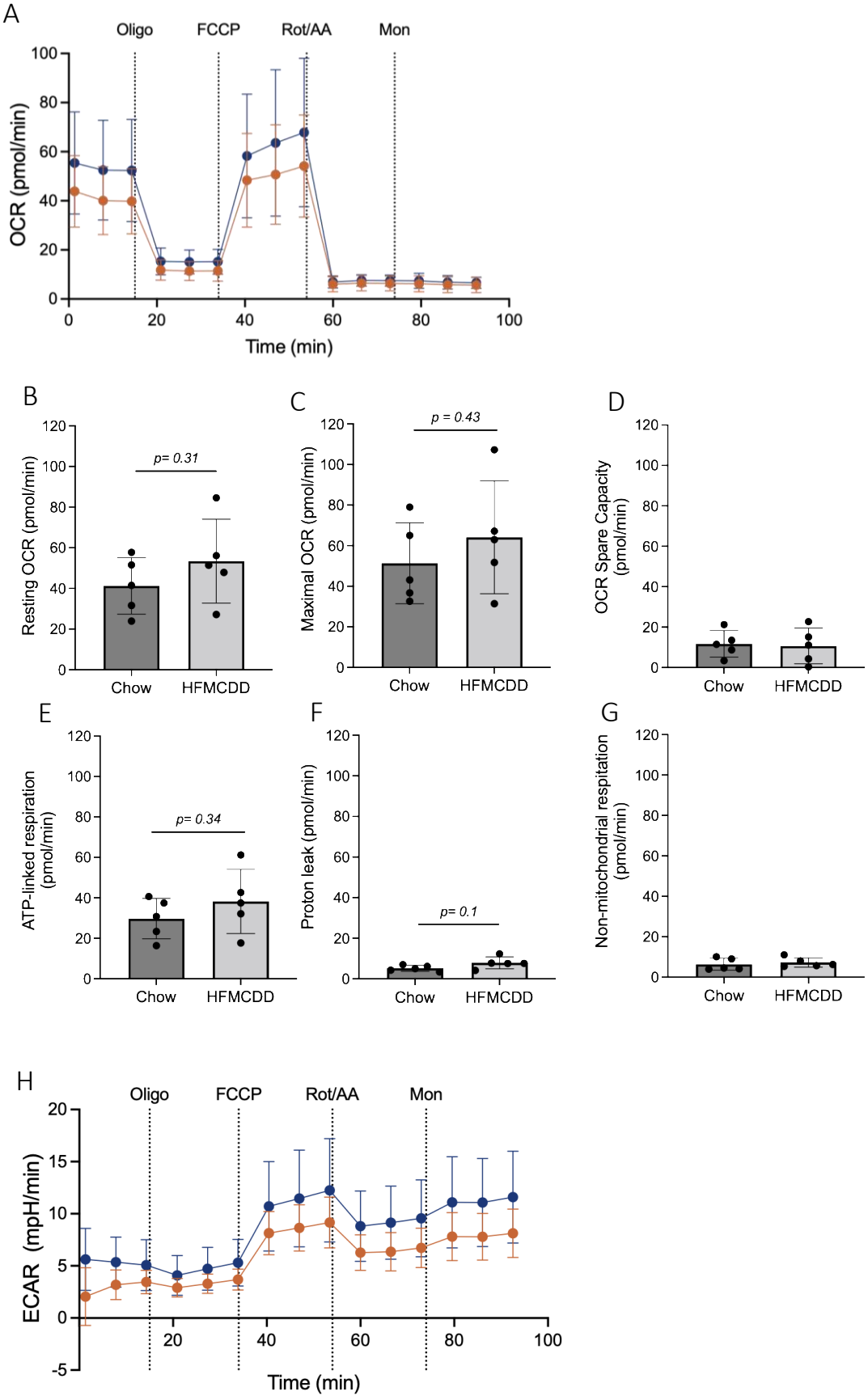
A
Oligo
FCCP
Rot/AA
Mon
OCR (pmol/min)
Time (min)
B
Resting OCR (pmol/min)
p= 0.31
Chow
HFMCDD
C
Maximal OCR (pmol/min)
p = 0.43
D
OCR Spare Capacity (pmol/min)
E
ATP-linked respiration (pmol/min)
p= 0.34
F
Proton leak (pmol/min)
p= 0.1
G
Non-mitochondrial respitation (pmol/min)
H
ECAR (mpH/min)

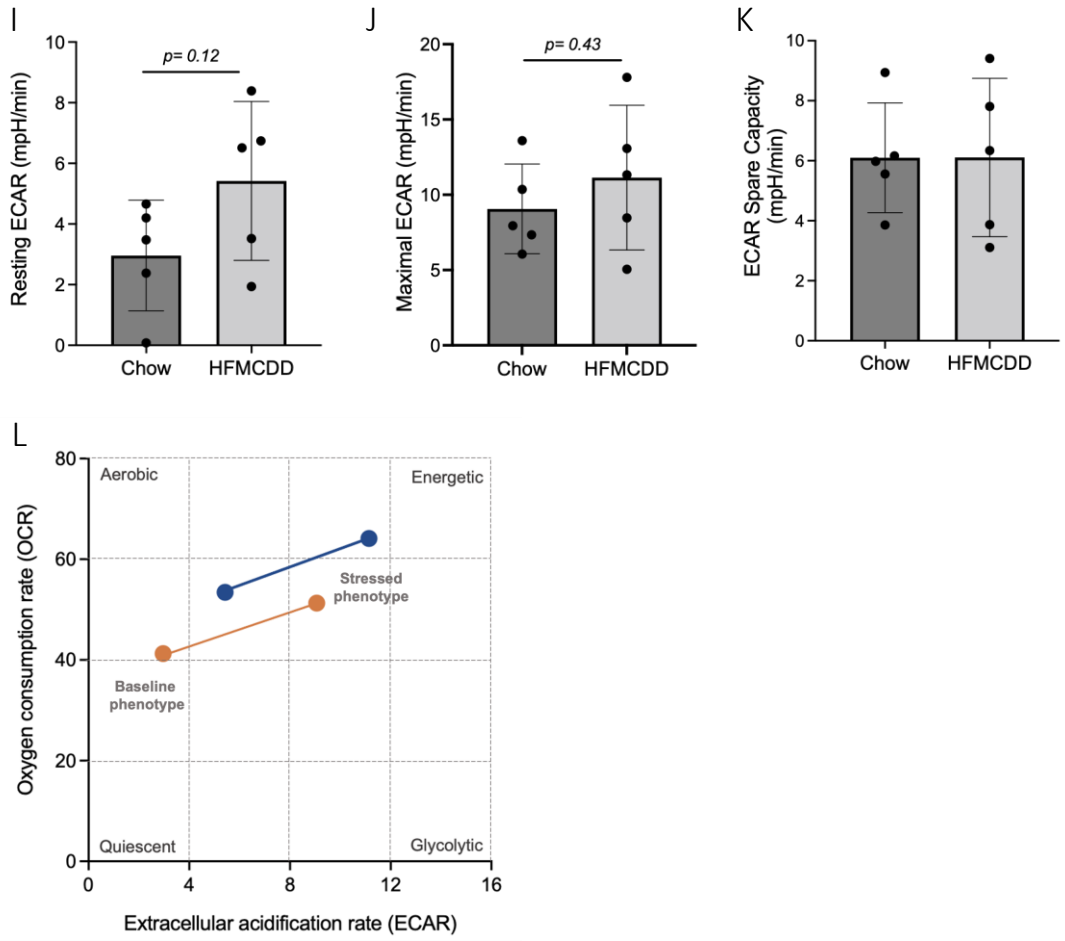

Figure 19: OCR and ECAR do not differ between chow and HFMCDD-fed males.

At peak treatment, week 21, animals were euthanized, and their spleens harvested. $CD8^+$ T cells were isolated from the spleens using negative magnetic bead selection for Seahorse metabolic analysis. (A) $CD8^+$ T cell OCR in response to the subsequent input of oligomycin, FCCP, rotenone/antimycin A and monensin. (B) Basal OCR, (C) maximal OCR, (D) spare respiratory capacity, (E) ATP-linked respiration, (F) proton leak and (G) non-mitochondrial respiration in chow and HFMCDD-fed animals at peak treatment. (H) $CD8^+$ T cell ECAR in response to the subsequent input of oligomycin, FCCP, rotenone/antimycin A and monensin. (I) Basal ECAR, (J) maximal ECAR and (K) ECAR spare capacity in chow and HFMCDD-fed animals at peak treatment. (L) $CD8^+$ T cell energy phenotype profiles in chow and HFMCDD-fed animals before and after metabolic challenge. Data presented as group means ±SD and statistically significant differences were determined using a two-tailed unpaired Student's *t*-test.

b. $CD8^+$ T cell respiration and glycolysis in females

In females, significant differences in mitochondrial respiration and glycolysis were measured. At peak treatment, HFMCDD-fed mice had elevated OCR and ECAR in all readouts, except for spare capacities (Figures 20 B-D and I-K). Therefore, $CD8^+$ T cells of HFMCDD females not only had elevated OXPHOS and glycolysis at rest but also a higher capacity to engage in these metabolic processes when challenged, meeting physiological energy demands. Furthermore, basal respiration in HFMCDD animals was elevated in comparison to the maximal respiration of chow-fed controls (Figure 20A). This indicates that diet-induced liver disease drove resting $CD8^+$ T cells in HFMCDD-fed mice to have a higher capacity to engage in OXPHOS in comparison to those in chow-fed mice, even following metabolic challenge. Finally, $CD8^+$ T cell energy phenotypes demonstrate clear differences between groups, in which, chow mice transition from a quiescent to glycolytic state and HFMCDD mice transition from an aerobic to energetic state post-metabolic challenge (Figure 20L).

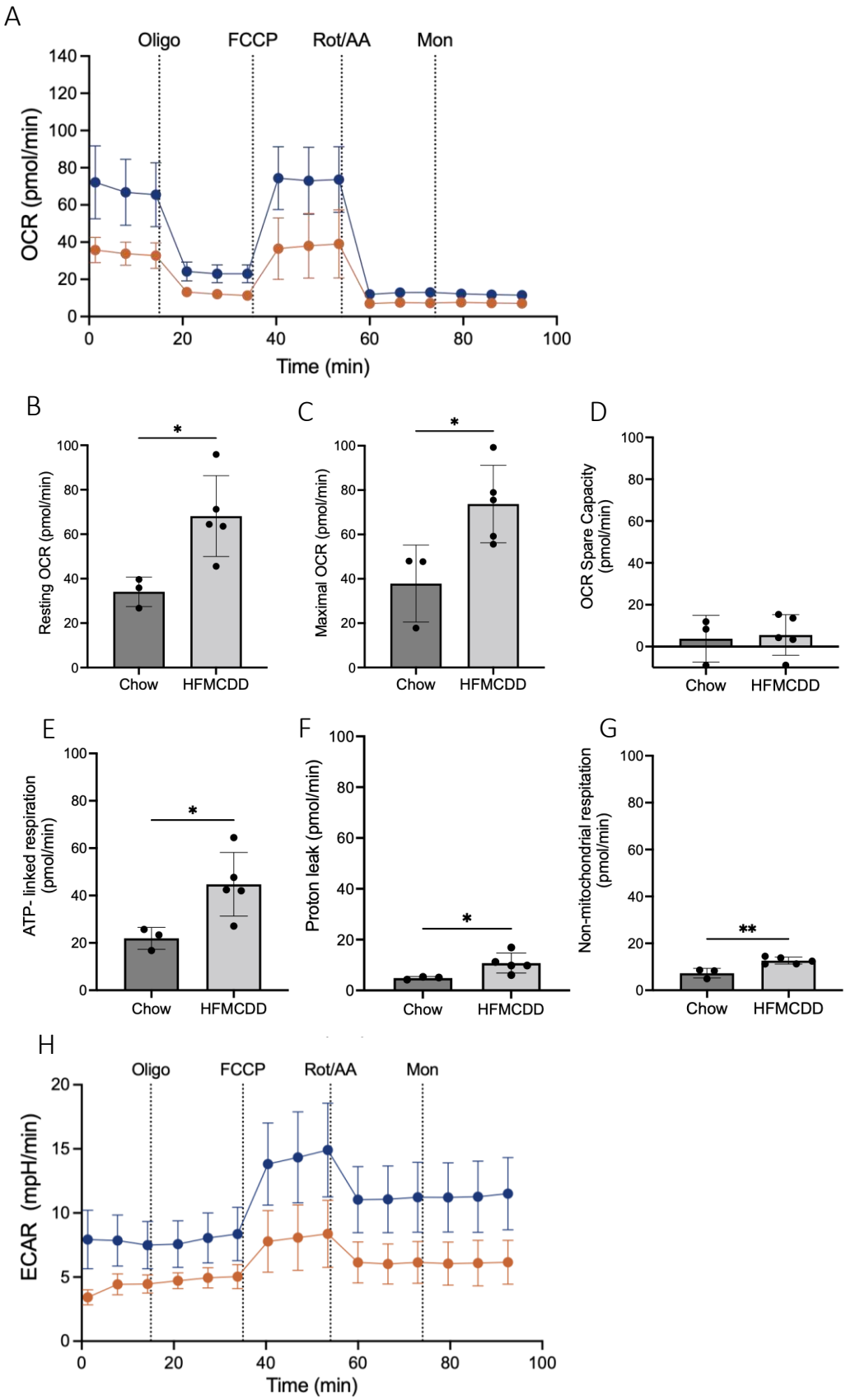
A
Oligo
FCCP
Rot/AA
Mon
OCR (pmol/min)
Time (min)
B
Resting OCR (pmol/min)
Chow
HFMCDD
C
Maximal OCR (pmol/min)
D
OCR Spare Capacity (pmol/min)
E
ATP- linked respiration (pmol/min)
F
Proton leak (pmol/min)
G
Non-mitochondrial respitation (pmol/min)
H
ECAR (mpH/min)

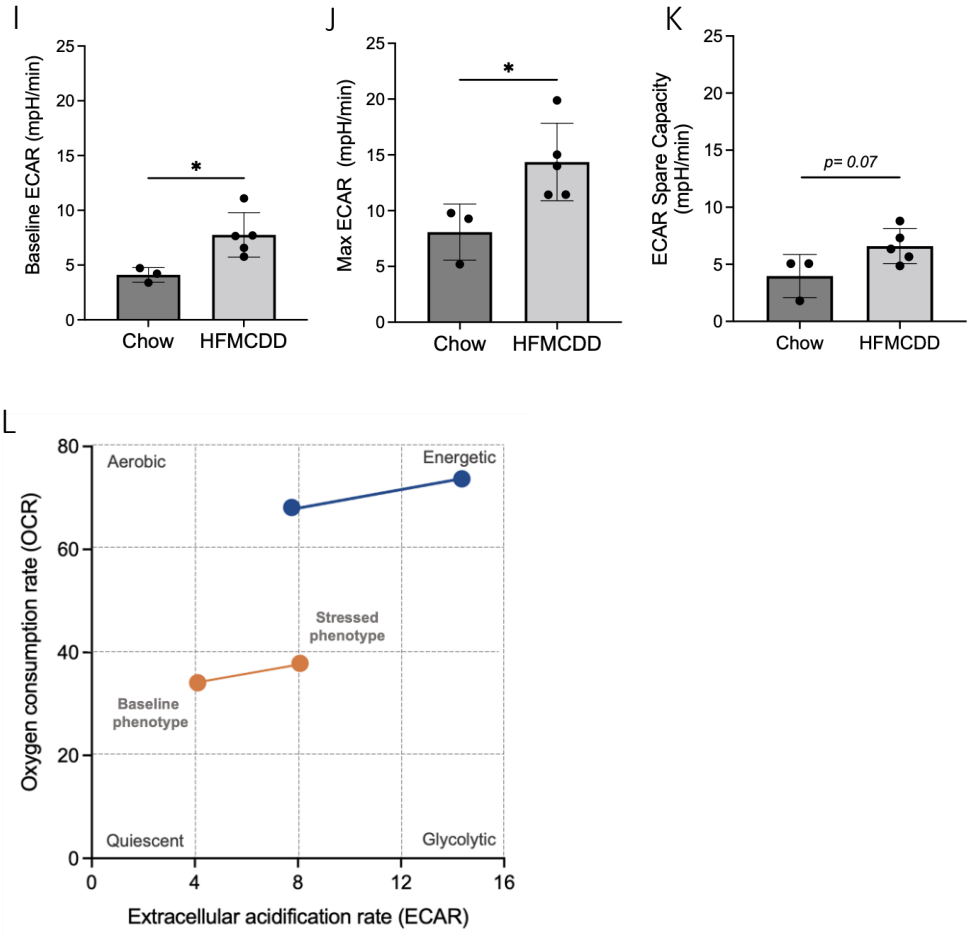

Figure 20: OCR and ECAR are upregulated in HFMCDD-fed females.

At peak treatment, week 21, animals were euthanized, and their spleens harvested. $CD8^+$ T cells were isolated from the spleens using negative magnetic bead selection for Seahorse metabolic analysis. (A) $CD8^+$ T cell OCR in response to the subsequent input of oligomycin, FCCP, rotenone/antimycin A and monensin. (B) Basal OCR, (C) maximal OCR, (D) spare respiratory capacity, (E) ATP-linked respiration, (F) proton leak and (G) non-mitochondrial respiration in chow and HFMCDD-fed animals at peak treatment. (H) $CD8^+$ T cell ECAR in response to the subsequent input of oligomycin, FCCP, rotenone/antimycin A and monensin. (I) Basal ECAR, (J) maximal ECAR and (K) ECAR spare capacity in chow and HFMCDD-fed animals at peak treatment. (L) $CD8^+$ T cell energy phenotype profiles in chow and HFMCDD-fed animals before and after metabolic challenge. Data presented as group means ±SD and statistically significant differences were determined using a two-tailed unpaired Student's *t*-test (*$p \leq 0.05$, **$p \leq 0.01$).

3.3 High-fat diet model

3.3.1 Liver injury induced by HFD feeding

In a collaborative project with the Bruin lab at the Carleton University, C57BL/6 mice aged 28-30 weeks were placed on a 45% HFD *ad libitum* for 14 weeks[103]. HFDs (≥45% fat) reliably induce MetS, encompassing obesity and hyperglycemia, characteristic of human MASLD. However, the progression from MASLD to MASH is not well replicated and a minimum of 25 weeks is often required to induce moderate liver disease[100]. The aim of this experiment was to determine how a short-term 14-week treatment period would influence liver pathology, host metabolism and downstream $CD8^+$ T cell function.

At endpoint, animals were euthanized, and liver samples were collected for histological analyses. Liver sections were formalin fixed, paraffin embedded, sectioned, and stained with Masson's trichrome and H&E dyes. HFD and control animals developed similar levels of liver fibrosis, with scores ranging from F0-2 (Figure 21A). As expected, advanced fibrosis was sparse and only one HFD treated mouse had developed F3 liver fibrosis. In controls, sex-specific analyses revealed that most females had minimal fibrosis (F1-2), while males had lower-level fibrosis (F0-1). Furthermore, HFD-fed animals had significantly elevated steatosis in comparison to chow-fed animals, in which most controls had no steatosis (only one with stage 2). Similar to fibrosis, steatosis was highly variable in the HFD group, ranging from stage 0-3. Low level inflammation was present in both control and HFD groups, yielding no significant differences. HFD mice had moderate ballooning (stage 0-2), while controls had an absence thereof (Figure 21A). Finally, no significant sex differences were observed in ballooning, steatosis, and inflammation scoring between male and female HFD-treated animals (data not shown). These histological findings confirm that this HFD model induced variable degrees of liver injury and

that the 14-week treatment period was not sufficient to induce advanced liver fibrosis, reminiscent of other reports using similar HFD models[99].

3.3.2 $CD8^+$ T cell dysfunction in HFD feeding

At endpoint, blood samples were collected by cardiac puncture and PBMCs were isolated following red blood cell lysis. PBMCs were then cultured for 48 hours with anti-CD3/28 stimulation and analyzed by flow cytometry for $CD8^+$ T cell functional analysis. Bulk circulating $CD8^+$ T cells in the HFD group had significantly elevated IFN-γ and GrzB expression (Figure 21B). Subset specific analysis also revealed significant differences in GrzB expression by T_{CM} cells and a trend in T_E/T_{EM} cells (Figure 21C). It is notable that $CD8^+$ T cell function was variable in both the HFD and chow groups, mirroring the variability observed in liver injury. Therefore, in the 45% HFD model, $CD8^+$ T cell hyperfunction was evident with steatotic pathology, yet in the absence of advanced liver fibrosis. This demonstrates that chronic liver insult resulting from liver steatosis is sufficient to drive $CD8^+$ T cell dysfunction.

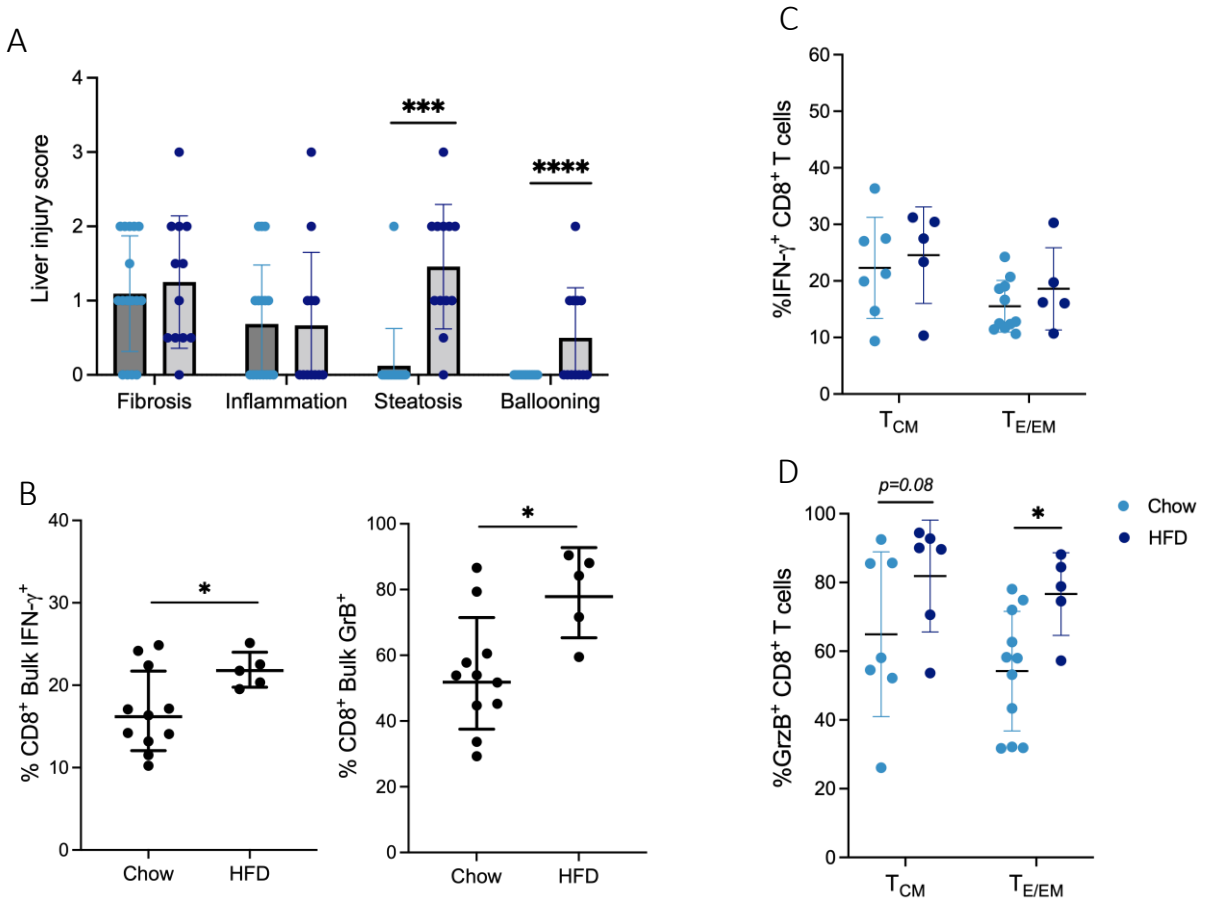

Figure 21: High-fat diet feeding induces CD8$^+$ T cell hyperfunction and liver steatosis in the absence of advanced liver fibrosis.

C57BL/6 mice aged 28-30 weeks were fed a regular chow (13% fat) or a 45% HFD for 14 weeks. After 14 weeks, animals were euthanized for blood and liver sample collection. Isolated PBMCs were stimulated for 48 hours with anti-CD3/28 antibodies for CD8$^+$ T cell functional analysis by flow cytometry. Liver samples were formalin-fixed, paraffin embedded, sectioned, and stained with Masson's Trichrome and H&E for histology. (A) Fibrosis, steatosis, inflammation and ballooning scores in chow and HFD-fed mice. (B) Proportion of IFN-γ^+ and GrzB$^+$ bulk CD8$^+$ T cells in chow and HFD-fed mice at peak treatment. (C) Proportion of IFN-γ^+ and (D) GrzB$^+$ central memory (T_{CM}) and effector/effector memory ($T_{E/EM}$) CD8$^+$ T cells. Data presented as group means ±SD and statistically significant differences were determined using a two-tailed unpaired Student's *t*-test (*p≤0.05, ***p≤0.001, ****p≤0.0001).

3.3.2 Metabolic syndrome in HFD feeding

MetS, characterized by obesity, hyperglycemia, hypertension and insulin resistance, is an important driver of human MASLD and its progression to MASH[120]. Therefore, features of MetS were measured in mice fed a 45% HFD for 14 weeks. HFD-fed animals developed obesity, with significantly elevated body weight and percent fat mass in comparison to chow-fed controls (Figures A-B & E-F). After 13 weeks of HFD feeding, animals underwent a glucose tolerance test, measuring blood glucose and plasma insulin levels over a period of 60-90 minutes in response to intravenous glucose administration. Post-challenge, HFD mice had significantly elevated blood glucose and insulin levels in comparison to their chow-fed counterparts (Figures C-D & G-H). Minor sex differences emerged, in which, the difference between blood glucose in HFD and chow-fed males persists for a longer period (90-minutes post-challenge). Together, these results indicate that HFD feeding may have impaired insulin sensitivity, in which animals were unable to control hyperglycemia despite upregulated insulin production.

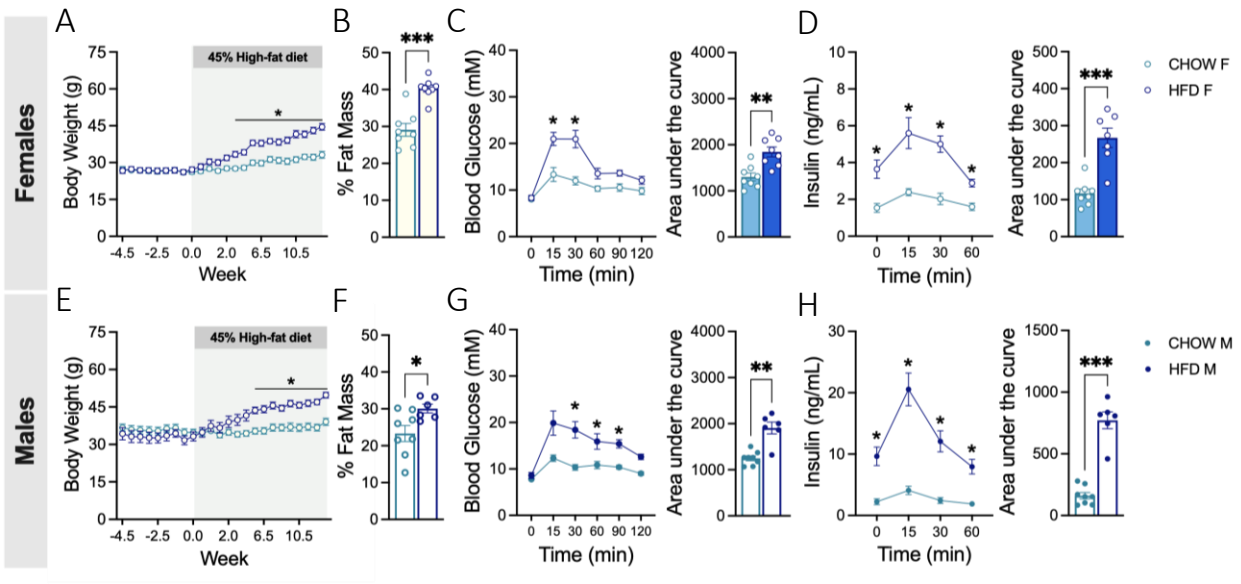

Figure 22: Host metabolism is disrupted in HFD feeding in male and female C57BL/6 mice.

(A)&(E) Body weight tracking over the course of treatment. (B)&(F) Percent fat mass. (C)&(G) Systemic blood glucose in response to glucose tolerance tests at week 13 of HFD feeding. (D)&(H) Plasma insulin in response to glucose tolerance test. Data presented as group mean ±SD and statistically significant differences were determined using a two-tailed unpaired Student's *t*-test (*p≤0.05, **p≤0.01, ***p≤0.001). Data obtained from Angela Ching (PhD candidate, Bruin lab).

Chapter 4: Discussion

In this thesis, a model of diet-induced liver disease is described, which evaluated impacts on circulating $CD8^+$ T cell function, mitochondrial potential, ROS, mitochondrial respiration, and glycolysis. This model reliably induced MASH-related liver pathology, characterized by advanced steatosis and fibrosis, with moderate ballooning and inflammation. Liver disease was accompanied by circulating bulk, central memory, and effector/effector memory $CD8^+$ T cell hyperfunction, in which cells expressed elevated IFN-γ and GrzB. Transiently elevated ROS and mitochondrial potential were detected in males at the time when hyperfunction emerged, while elevated mitochondrial respiration and glycolysis were detected in females at peak treatment. In an alternate model of chronic liver disease, induced by hepatotoxin, we were unable to evaluate these aspects of T cell immunometabolism as $CD8^+$ T cell hyperfunction was not reproduced, as previously reported[103].

4.1 Hepatotoxin-induced advanced liver fibrosis

Studying the immunological impact of HCV-induced liver fibrosis remains challenging due to the lack of susceptible animal models. Therefore, the carbon tetrachloride model, first developed in rats, was established to replicate features of liver pathology, without confounding viral infection. CCl_4 induces hepatocyte necrosis, pericentral fibrosis with progressive central and portal bridging, and eventual cirrhosis. Initial necrosis triggers wound healing responses, characterized by the recruitment of inflammatory cells, the accumulation of mitochondrial ROS and the deposition of ECM components, promoting fibrogenesis[96]. Although the C57BL/6 strain is often reported to develop intermediate liver fibrosis in CCl_4 treatment[95], the Crawley lab previously induced advanced (F3-4) fibrosis following 12-16 weeks of hepatotoxin

administration[103]. Therefore, this strain was selected for its ability to develop advanced liver disease mimicking that reported in HCV-infection and as it is readily available in multiple knockout and transgenic models, thereby facilitating opportunities for future mechanistic studies.

In this thesis, C57BL/6 mice were treated with CCl_4 for a period of 21 weeks. Data demonstrated that 21 weeks of CCl_4 treatment induced advanced liver fibrosis (Figure 2C), consistently generating F3 fibrosis in males (Figure 2E), as we previously described[103]. However, livers from the females yielded an uncharacteristically high variability of fibrosis (F0-4) (Figure 2D). It is notable that most animals tolerated treatment well, maintaining relatively similar body weights to their control counterparts (Figure 1B) and had the ability to quickly recover post-saphenous bleed, as previously observed. However, animals randomized to the CCl_4 group were slightly lower in weight than those assigned to the treatment group, and body weight should be considered in the randomization of future groups for such studies.

In another cohort of animals, liver injury was assessed post-CCl_4 cessation. Following a brief 4-week regression period, CCl_4-treated animals had mild liver fibrosis (F1-2), which was significantly elevated in comparison to controls (Figure 3). Although liver fibrosis severity was not verified at peak CCl_4 treatment, the animals likely had F3-4 fibrosis as previously described in this model[103]. In future cohorts, larger sample sizes should be utilized to allow for histological analyses at peak treatment and post-treatment cessation, for the quantification of the degree of liver injury regression. In individuals with chronic liver disease, liver fibrosis regression is often dictated by individual factors and the severity of tissue damage sustained. In certain HCV-infected patients, viral clearance with DAA therapy successfully improves liver fibrosis. One study found that 49% of individuals with advanced fibrosis had a 20% reduction in their FibroTest scores, a system that uses serum biomarkers to assign liver fibrosis severity[121]. This

correlates with reductions in METAVIR scores, in another independent experiment, in which approximately 50% of HCV-infected individuals decreased from F3-4 to F0-2 post-HCV cure with DAA therapy[122]. The mechanisms driving liver fibrosis regression are complex, and often require many years in those that achieve SVR, but unfortunately, many cirrhotic patients are unable to regress fibrosis post-HCV cure. These individuals remain at high-risk for the development of HCC, ranging from 1.8-2.5% annually[122].

4.2 $CD8^+$ T cell function in hepatotoxin-induced liver fibrosis

$CD8^+$ T cells play an important role in the immune-mediated response to intracellular pathogens and certain cancers[66,67]. In HCV infection, $CD8^+$ T cell responses are particularly important for viral control and to produce immunoregulatory IFN-γ. However, HCV-specific $CD8^+$ T cell activity is not detectable until upwards of 8 weeks post-HCV infection, potentially contributing to the high proportion of individuals progressing to chronic persistent infection[68]. In chronic HCV infection, many groups report virus-specific $CD8^+$ T cell exhaustion, negatively impacting effector function and viral clearance[66,70,72]. Complementing this pathogen-specific knowledge, the Crawley lab has reported hyperfunction of bulk circulating $CD8^+$ T cells, characterized by elevated perforin and IFN-γ expression in advanced liver fibrosis[123]. A model of hepatotoxin-induced liver disease was adapted in C57BL/6 mice to mimic HCV-related liver pathology in approximately 12-16 weeks. This model also reliably induced bulk $CD8^+$ T cell hyperfunction in multiple independent experiments, in which CCl_4-treated mice had elevated proportions of both IFN-γ^+ and $GrzB^+$ $CD8^+$ T cells[103]. Other reports also found that the CCl_4 model impairs $CD4^+$ T cells, in which CCl_4 treatment triggers an imbalance in the ratio of Tregs/Th17 cells in the liver, contributing to the progression of fibrosis[124]. Unfortunately, in this

thesis, we were unable to detect $CD8^+$ T cell hyperfunction despite the development of CCl_4-induced advanced liver fibrosis. Differences in immune cell function did not emerge even after prolonging the CCl_4 treatment period upwards of 20 weeks (Figure 4). The use of a new CCl_4 stock in CCl_4-E02 did not resolve this issue. Finally, $CD8^+$ T cell mitochondrial potential and ROS did not differ between CCl_4 and control animals perhaps in tandem, or consequentially, in the absence of cellular hyperfunction.

4.3 Inducing advanced liver steatosis and fibrosis in HFMCDD-feeding

Today, MASLD/ MASH remains the fastest growing cause of chronic liver disease in Canada and is replacing hepatic viral infections as the primary indicator for liver transplantation[2]. North America is particularly affected by the rising epidemic of metabolic syndrome, encompassing factors such as obesity, type II diabetes/insulin resistance and hyperlipidemia: important risk factors in MASLD and its progression to MASH. Therefore, a mouse model was adopted that better replicates pathologic features of human MASLD to examine the downstream impacts on immune cell function. These experiments also aimed to characterize sex differences in disease progression as important differences exist in human MASLD risk, fibrosis development and HCC[37,38,40]. The HFMCDD model integrates features of the HFD and MCD models, rapidly generating advanced liver fibrosis without overweight/obesity as a confounder. Chiba et al. have reported that 0.1% methionine induces the greatest degree of liver injury, while preventing weight loss and cachexia characteristic of the MCD model. Animals on the HFMCDD are reported to have similar body weight to controls, yet have elevated liver weight and elevated plasma triglycerides[101]. This model also induces progressive liver fibrosis, with: moderate fibrosis (F1/2) by week 4 of diet-feeding, periportal-

sinusoidal (F2) fibrosis by week 8 and advanced bridging pan-lobular fibrosis (F3) by week 12[102].

In this thesis, twenty-one weeks of *ad libitum* HFMCDD feeding induced significant liver disease in both male and female C57BL/6 mice (Figures 10E, 11E) with minor sex differences. In males, there was more advanced liver fibrosis (F3-F4) than in females (F2-F3). Meanwhile, steatosis and inflammation were comparable across sexes, with an average of stage 3 steatosis and stage 1 inflammation. Elevations in liver and spleen weight were also observed in males (Figure 8) even in the absence of obesity/overweight, in both individual and group housing (Supplemental Fig. 1). Therefore, weight gain in individually housed males (Figure 7B) likely did not drive these trends in organ weight. In females, an increase in liver weight was apparent in one cohort (Figure 8), and elevated spleen and liver weight in another (Supplemental Fig. 1). These features replicate hepatomegaly and splenomegaly, common features of human MASLD and MASH. Splenomegaly tends to be associated with cirrhosis and portal hypertension, in which 20-30% of patients with F3-4 fibrosis experience enlargement of the spleen[116]. A driving factor of splenomegaly in MetS is the production of inflammatory factors, released by adipose fat circulating in the portal system[125]. Finally, in group housing, HFMCDD animals, both males and females, maintained relatively similar body weights to their control counterparts (Figure 7C and D).

A cohort of mice fed the HFMCDD for 21 weeks underwent liver pathology regression, following a return to the control chow diet. After 4 weeks on the chow diet, steatosis was reduced to control levels in males (Score 1-2) (Figure 12A and C) and fully resolved in females (Score 0) (Figure 12B and D). Fibrosis regression did not occur as readily in this model, reducing by approximately one F score in males, while remaining unchanged in females. From these

results, it is estimated that upwards of 4 weeks is required for significant liver tissue remodelling with diet-induced liver damage of this nature. Similar to HCV, liver fibrosis regression in MASH is dependent on its severity. Those with minimal fibrosis (F1) are more likely to undergo regression with lifestyle modification and treatment of MetS, while those with advanced fibrosis may have more persistent liver injury[126]. Furthermore, females appeared to display delayed liver fibrosis regression, in comparison to their male counterparts, potentially attributable to declining estrogens.

4.4 $CD8^+$ T cell hyperfunction in diet-induced liver disease

In MASLD, liver resident $CD8^+$ T cells have been found to display an activated-exhausted phenotype. In disease, these cells produce elevated inflammatory cytokines, sustaining chronic inflammation, while they express PD-1 conferring exhaustion in HCC[57,127]. Furthermore, these activated-exhausted tissue-resident T cells play a direct role in liver pathology, driving fibrosis and the progression from MASLD to MASH through the non-specific killing of hepatocytes. Altered hepatic lipid metabolism plays a role in the development of this T cell phenotype, in which excess fatty acid, acetate, increases cellular granzyme expression and TNF release[57]. We aimed to characterize functional disturbances of bulk circulating $CD8^+$ T cells in a murine model replicating MASH pathology. $CD8^+$ T cell hyperfunction, characterized by elevated GrzB and IFN-γ expression, arose after 4 weeks of *ad libitum* HFMCDD feeding in males, at a time when advanced steatosis with minimal fibrosis is expected[99]. This hyperfunction was transiently lost at week 12 and subsequently reoccurred until the end of the 21-week treatment period (Figure 13). Hyperfunction emerged at week 8 in a cohort of females and persisted through the end of treatment (Figure 14). However, in this group we were unable to

perform $CD8^+$ T cell functional analyses at week 4, the time at which hyperfunction emerged in males. Therefore, a direct comparison to their male counterparts could not occur, and these experiments were repeated in a second cohort of females. Interestingly, this second cohort of females displayed hyperfunction in IFN-γ after 4 weeks of HFMCDD feeding, similar to the first cohort of males (Supplemental Fig. 3C and D). Because of this inconsistency observed in the results, conclusive sex differences in hyperfunction timing cannot be established until additional HFMCDD experiments are conducted. Together, these data indicate that cellular hyperfunction emerges when peak liver steatosis is expected, at a time when liver fibrosis has not been established. While in the CCl_4 model, which does not develop significant liver steatosis, advanced fibrosis is required for cellular hyperfunction. These findings may have important implications for human MASLD, in which immune dysfunction may parallel closely the progression of liver damage.

After 21 weeks, a subset of HFMCDD-fed animals in E01 (males) and E02 (females) were returned to the control chow diet. Following HFMCDD cessation, $CD8^+$ T cell function was monitored for an additional 4 weeks. In males, $CD8^+$ T cell hyperfunction did not persist post-HFMCDD cessation. However, these results may be attributed to the animal randomization process, where the $CD8^+$ T cell function of the selected control and HFMCDD animals for this sub study were not significantly different at peak (Figure 15A). In the future, to ensure the comparison of animals that differ in $CD8^+$ T cell function, between chow and HFMCDD treatments, cessation study groups will be intentionally selected. In females, potential lasting hyperfunction was observed, in which the HFMCDD-fed mice switched to the control chow diet retained significantly elevated GrzB expression and trending elevated IFN-γ ($p=0.09$) 2 weeks post-diet cessation compared to mice fed the chow throughout the study (Figure 15B). The

females selected for this sub study were hyperfunctional at peak treatment, unlike with the males. Additional regression experiments need to be performed to establish conclusive sex-specific differences in lasting cellular hyperfunction. In human MASLD, perhaps the attainment of peak liver fibrosis would preserve the immunological scar on cells, resulting in sustained immune dysfunction, as previously observed in human HCV and the CCl_4 model.

4.5 $CD8^+$ T cell metabolic fitness in a murine model of diet-induced liver disease replicating MASH pathology

To elucidate potential mechanisms driving $CD8^+$ T cell hyperfunction, we aimed to determine if metabolic fitness (i.e., OXPHOS and glycolysis) was altered in diet-induced liver injury. Throughout HFMCDD experiments, unstimulated circulating $CD8^+$ T cell mitochondrial potential and ROS were quantified by flow cytometry. In males, $CD8^+$ T cell ROS were elevated concurrently with the appearance of hyperfunction, at week 4. This was closely followed by a trending increase in mitochondrial potential, at week 8 (Figure 16C). These findings indicate potentially upregulated mitochondrial respiration in advanced steatosis, in which cells are more polarized and have a higher capacity to engage in OXPHOS, generating ATP required for effector functions. Sex dependencies in this aspect of cellular biology were notable, these differences did not emerge in HFMCDD-fed females at any time throughout treatment (Figure 17).

Extracellular acidification and oxygen consumption rates were then evaluated at peak treatment, as measures of glycolysis and OXPHOS, respectively. Surprisingly, in the absence of notable differences in mitochondrial polarization and ROS, significant differences were apparent in female ECAR and OCR readouts (Figure 20), but not in males (Figure 19). Furthermore, in

females, basal OCR values in the HFMCDD group were elevated not only in comparison to the basal OCR in the control group but also compared to the maximal OCR in these controls (Figure 20A), indicating that $CD8^+$ T cells from HFMCDD-fed mice have a higher capacity to engage in OXPHOS even at rest. Cells from the HFMCDD animals also had elevated maximal respiration in comparison to control animals when metabolically challenged *in vitro* with FCCP (Figure 20C). Therefore, in steatotic liver disease, $CD8^+$ T cells from HFMCDD mice have elevated energy availability and utilization potential, likely driven by the chronic inflammatory environment, and likely contributing to the elevated effector functions of these cells. However, despite cellular hyperfunction and advanced liver disease pathology, these differences did not arise in two independent studies of HFMCDD-treated males (Figure 19).

To better elucidate metabolic mechanisms driving cellular hyperfunction, future directions may include analyses of the mTOR signaling pathway. This pathway is activated upon TCR signaling and CD28 co-stimulation, driving cellular glycolysis and mitochondrial respiration (Figure 23). This could be assessed by measuring the phosphorylation of protein S6 by flow cytometry, a surrogate marker for mTORC1 activity. Furthermore, certain drugs, such as metformin, act to inhibit the mTOR signaling pathway, reducing T cell effector functions[128]. Administering metformin in this murine model of diet-induced liver disease may elucidate the role of mTOR signaling in driving cellular hyperfunction in steatotic liver disease.

4.6 $CD8^+$ T cell hyperfunction in a model of HFD-induced steatosis without advanced liver fibrosis

In an alternate murine model of MASLD, C57BL/6 mice were fed a 45% HFD *ad libitum* for 14 weeks as part of a collaborative project with Dr. Jennifer Bruin's lab at Carleton

University. As previously described, HFDs induce MetS, notably obesity and insulin resistance[99,129], characteristic of how most humans experience MASLD. Unfortunately, the HFD models poorly replicate the transition to MASH and chronic inflammation, and often require upwards of 25 weeks to induce advanced liver fibrosis[100]. In this study, the HFD mice developed MetS, elevated body weight (Figure 22A and E), elevated percent fat mass (Figure 22B and F) and elevated blood glucose post-glucose challenge (Figure 22C and G). Fibrosis was highly variable in the HFD group, yielding an average of F1 fibrosis in both control and HFD groups (Figure 21A), confirming that HFDs induce varying degrees of liver injury. However, we did observe significantly elevated steatosis (stage 1-2) and ballooning in the HFD group. In the Crawley lab, future HFMCDD cohorts should be evaluated for MetS, characterizing host metabolism as it relates to human MASLD.

Flow cytometry analysis of bulk circulating $CD8^+$ T cell function revealed significantly elevated IFN-γ and GrzB expression in the HFD group (Figure 21B and C). Therefore, as observed in the HFMCDD model, these findings highlight the importance of steatosis or the immunological features of steatosis in driving cellular hyperfunction, in which advanced liver fibrosis was not required to drive functional impairments.

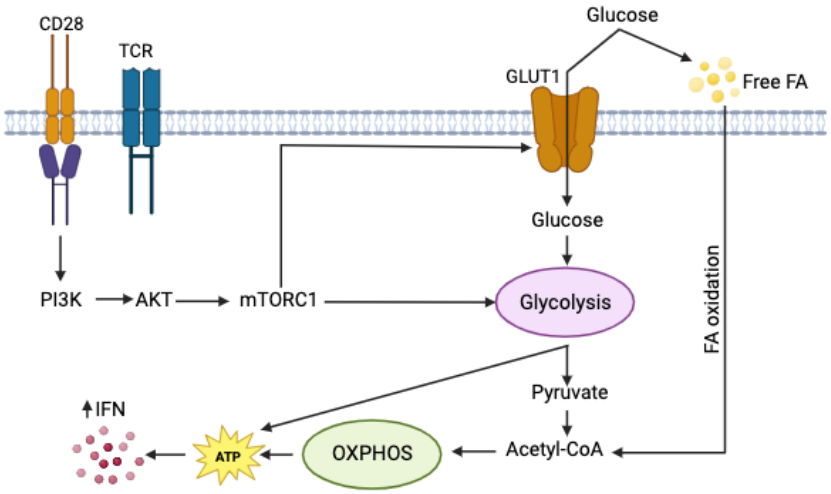

Figure 23: Overview of CD8^{+} T cell metabolism driving effectors functions in MASLD.

Appendix

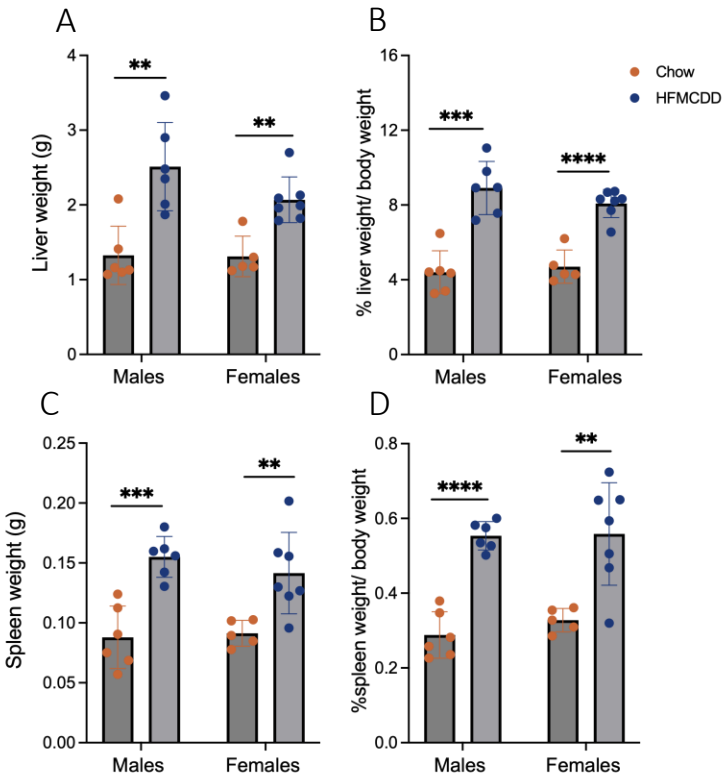

Supplemental figure 1: The spleen and liver are enlarged in HFMCDD mice after 17 weeks.

After 17 weeks of HFMCDD feeding, mice were euthanized, and the spleens and livers harvested. (A) Liver weight and (B) liver weight relative to total body weight in male and female C57BL/6 mice at peak treatment. (C) Spleen weight and (D) spleen weight relative to total body weight in males and females at peak treatment. Data presented as group means ±SD and statistically significant differences were determined using a two-tailed unpaired Student's *t*-test (**p≤0.01, ***p≤0.001, ****p≤0.0001).

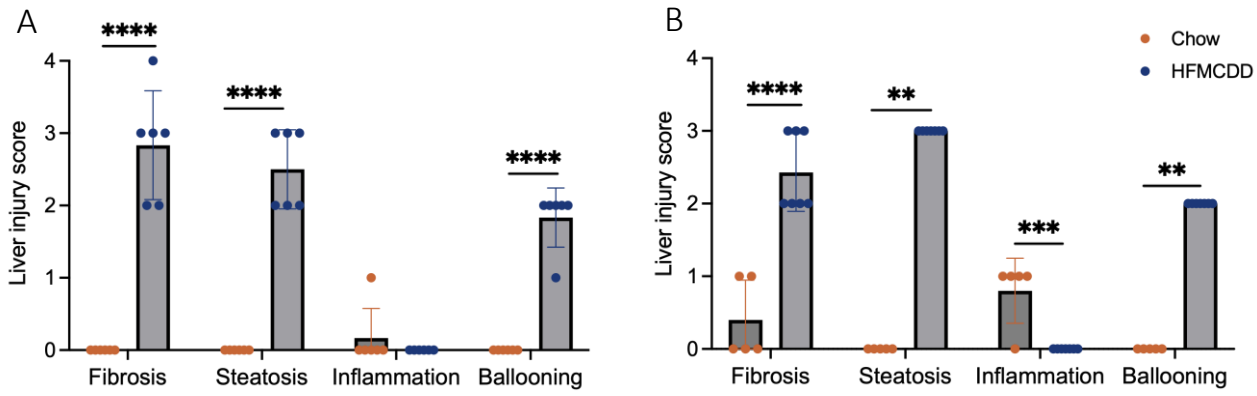

Supplemental figure 2: HFMCDD-feeding induces advanced liver fibrosis with steatosis, ballooning, and inflammation after 17 weeks in male and female C57BL/6 mice.

At peak treatment, animals were euthanized, and liver samples were collected for histology. Liver sections were formalin-fixed, sectioned and stained with Masson's Trichrome (fibrosis) and H&E (steatosis, inflammation, and ballooning). (A) Liver fibrosis, steatosis, inflammation and ballooning scores in chow and HFMCDD-fed males and (B) females at peak treatment. Data presented as group means ±SD and statistically significant differences were determined using a two-tailed unpaired Student's *t*-test (**p≤0.01, ***p≤0.001, ****P≤0.0001). In Figure B, a Mann-Whitney U-test was performed for statistical analyses of steatosis and ballooning.

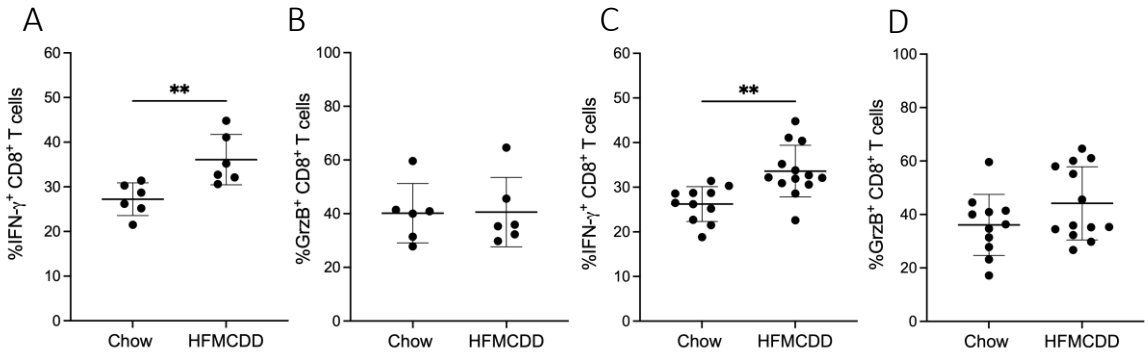

Supplemental figure 3: CD8$^+$ T cell hyperfunction arises after 4 weeks of HFMCDD-feeding in males and females.

PBMCs were stimulated for 48 hours with anti-CD3/28 antibodies for functional analysis of circulating CD8$^+$ T cells. (A) Proportion of IFN-γ^+ and (B) GrzB$^+$ CD8$^+$ T cells in males. (C) Proportion of IFN-γ^+ and (D) GrzB$^+$ CD8$^+$ T cells in females. Data presented as group means ±SD. Statistically significant differences were determined using a two-tailed unpaired Student's *t*-test (**p≤0.01).

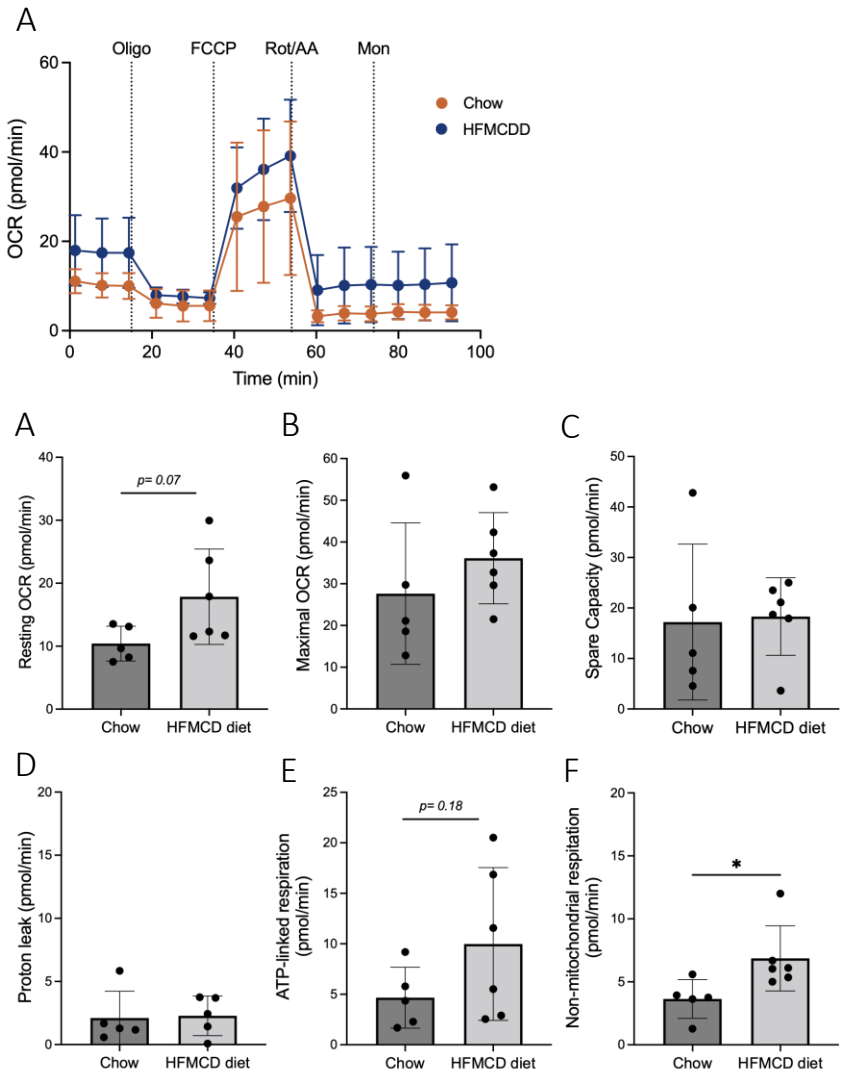

Supplemental figure 4: Mitochondrial respiration does not differ between chow and HFMCDD-fed males after 17 weeks of HFMCDD feeding.

At peak treatment, week 17, animals were euthanized, and the spleen harvested. $CD8^+$ T cells were isolated from the spleen using negative magnetic bead selection. (A) $CD8^+$ T cell OCR in response to subsequent injection of oligomycin, FCCP, rotenone/antimycin A and monensin. (B) Basal OCR, (C) Maximal OCR, (D) Spare respiratory capacity, (E) ATP-linked respiration, (E) Proton leak and (F) Non-mitochondrial respiration in chow and HFMCDD-fed animals at peak treatment. Data presented as group means ±SD and statistically significant differences were determined using a two-tailed unpaired Student's *t*-test (*$p \leq 0.05$).

References

1. Global Epidemiology of Chronic Liver Disease - Cheemerla - 2021 - Clinical Liver Disease - Wiley Online Library. Accessed November 16, 2022. https://aasldpubs.onlinelibrary.wiley.com/doi/10.1002/cld.1061

2. Brahmania M, Biondi MJ, Joshi S, Lee E, Jung HM, Kehar M. Priority actions for elevating liver health in Canada: A call to action. *Can Liver J*. 6(2):283-290. doi:10.3138/canlivj-2022-0041

3. Canada H. Government of Canada supports first national guideline on high-risk drinking and alcohol use disorder. Published January 28, 2021. Accessed July 31, 2023. https://www.canada.ca/en/health-canada/news/2021/01/government-of-canada-supports-first-national-guideline-on-high-risk-drinking-and-alcohol-use-disorder.html

4. Fuster D, Sanvisens A, Bolao F, Rivas I, Tor J, Muga R. Alcohol use disorder and its impact on chronic hepatitis C virus and human immunodeficiency virus infections. *World J Hepatol*. 2016;8(31):1295-1308. doi:10.4254/wjh.v8.i31.1295

5. Chiang DJ, McCullough AJ. The Impact of Obesity and Metabolic Syndrome on Alcoholic Liver Disease. *Clin Liver Dis*. 2014;18(1):157-163. doi:10.1016/j.cld.2013.09.006

6. Shirazi F, Wang J, Wong RJ. Nonalcoholic Steatohepatitis Becomes the Leading Indication for Liver Transplant Registrants Among US Adults Born Between 1945 and 1965. *J Clin Exp Hepatol*. 2020;10(1):30-36. doi:10.1016/j.jceh.2019.06.007

7. Lytvyak E, Straube S, Modi R, Lee KK. Trends in obesity across Canada from 2005 to 2018: a consecutive cross-sectional population-based study. *CMAJ Open*. 2022;10(2):E439-E449. doi:10.9778/cmajo.20210205

8. Government of Canada SC. Diabetes, 2017. Published November 14, 2018. Accessed September 20, 2023. https://www150.statcan.gc.ca/n1/pub/82-625-x/2018001/article/54982-eng.htm

9. Government of Canada SC. Overweight and obese adults, 2018. Published June 25, 2019. Accessed September 20, 2023. https://www150.statcan.gc.ca/n1/pub/82-625-x/2019001/article/00005-eng.htm

10. Swain MG, Ramji A, Patel K, et al. Burden of nonalcoholic fatty liver disease in Canada, 2019–2030: a modelling study. *CMAJ Open*. 2020;8(2):E429-E436. doi:10.9778/cmajo.20190212

11. Preciado MV, Valva P, Escobar-Gutierrez A, et al. Hepatitis C virus molecular evolution: Transmission, disease progression and antiviral therapy. *World J Gastroenterol*. 2014;20(43):15992-16013. doi:10.3748/wjg.v20.i43.15992

12. Tosone G, Maraolo AE, Mascolo S, Palmiero G, Tambaro O, Orlando R. Vertical hepatitis C virus transmission: Main questions and answers. *World J Hepatol*. 2014;6(8):538-548. doi:10.4254/wjh.v6.i8.538

13. Is sexual contact a major mode of hepatitis C virus transmission? - Tohme - 2010 - Hepatology - Wiley Online Library. Accessed August 1, 2023. https://aasldpubs.onlinelibrary.wiley.com/doi/full/10.1002/hep.23808

14.World Health Organization. Elimination of hepatitis by 2030. Accessed July 31, 2023. https://www.who.int/multi-media/details/elimination-of-hepatitis-by-2030

15. World Health Organization. Hepatitis C. Accessed July 31, 2023. https://www.who.int/news-room/fact-sheets/detail/hepatitis-c

16. Adinolfi LE, Durante-Mangoni E, Zampino R, Ruggiero G. Review article: hepatitis C virus-associated steatosis – pathogenic mechanisms and clinical implications. *Alimentary Pharmacology & Therapeutics*. 2005;22(s2):52-55. doi:10.1111/j.1365-2036.2005.02597.x

17. Bose SK, Ray R. Hepatitis C virus infection and insulin resistance. *World J Diabetes*. 2014;5(1):52-58. doi:10.4239/wjd.v5.i1.52

18. Tsubota A, Fujise K, Namiki Y, Tada N. Peginterferon and ribavirin treatment for hepatitis C virus infection. *World J Gastroenterol*. 2011;17(4):419-432. doi:10.3748/wjg.v17.i4.419

19. Kish T, Aziz A, Sorio M. Hepatitis C in a New Era: A Review of Current Therapies. *P T*. 2017;42(5):316-329.

20. Sulkowski MS, Cooper C, Hunyady B, et al. Management of adverse effects of Peg-IFN and ribavirin therapy for hepatitis C. *Nat Rev Gastroenterol Hepatol*. 2011;8(4):212-223. doi:10.1038/nrgastro.2011.21

21. Bailey JR, Barnes E, Cox AL. Approaches, Progress, and Challenges to Hepatitis C Vaccine Development. *Gastroenterology*. 2019;156(2):418-430. doi:10.1053/j.gastro.2018.08.060

22. Poynard T, Ratziu V, Charlotte F, Goodman Z, McHutchison J, Albrecht J. Rates and risk factors of liver fibrosis progression in patients with chronic hepatitis C. *Journal of Hepatology*. 2001;34(5):730-739. doi:10.1016/S0168-8278(00)00097-0

23. Bakr I, Rekacewicz C, Hosseiny ME, et al. Higher clearance of hepatitis C virus infection in females compared with males. *Gut*. 2006;55(8):1183-1187. doi:10.1136/gut.2005.078147

24. Canada PHA of. Hepatitis C in Canada: 2019 surveillance data. Published July 14, 2021. Accessed September 27, 2023. https://www.canada.ca/en/public-health/services/publications/diseases-conditions/hepatitis-c-2019-surveillance-data.html

25. Yasuda M, Shimizu I, Shiba M, Ito S. Suppressive effects of estradiol on dimethylnitrosamine-induced fibrosis of the liver in rats. *Hepatology*. 1999;29(3):719-727. doi:10.1002/hep.510290307

26. Yuan Y, Shimizu I, Shen M, et al. Effects of estradiol and progesterone on the proinflammatory cytokine production by mononuclear cells from patients with chronic hepatitis C. *World J Gastroenterol*. 2008;14(14):2200-2207. doi:10.3748/wjg.14.2200

27. Itagaki T, Shimizu I, Cheng X, et al. Opposing effects of oestradiol and progesterone on intracellular pathways and activation processes in the oxidative stress induced activation of cultured rat hepatic stellate cells. *Gut*. 2005;54(12):1782-1789. doi:10.1136/gut.2005.053278

28. Teng ML, Ng CH, Huang DQ, et al. Global incidence and prevalence of nonalcoholic fatty liver disease. *Clin Mol Hepatol*. 2023;29(Suppl):S32-S42. doi:10.3350/cmh.2022.0365

29. Fernando DH, Forbes JM, Angus PW, Herath CB. Development and Progression of Non-Alcoholic Fatty Liver Disease: The Role of Advanced Glycation End Products. *International Journal of Molecular Sciences*. 2019;20(20). doi:10.3390/ijms20205037

30. Friedman SL, Neuschwander-Tetri BA, Rinella M, Sanyal AJ. Mechanisms of NAFLD development and therapeutic strategies. *Nat Med*. 2018;24(7):908-922. doi:10.1038/s41591-018-0104-9

31. Pouwels S, Sakran N, Graham Y, et al. Non-alcoholic fatty liver disease (NAFLD): a review of pathophysiology, clinical management and effects of weight loss. *BMC Endocr Disord*. 2022;22:63. doi:10.1186/s12902-022-00980-1

32. Mehal WZ. The Gordian knot of dysbiosis, obesity and NAFLD. *Nature Reviews Gastroenterology & Hepatology*. 2013;10(11):637-645. doi:10.1038/nrgastro.2013.146

33. Shah PA, Patil R, Harrison SA. NAFLD-related hepatocellular carcinoma: The growing challenge. *Hepatology*. 2023;77(1):323-338. doi:10.1002/hep.32542

34. Aithal GP, Thomas JA, Kaye PV, et al. Randomized, Placebo-Controlled Trial of Pioglitazone in Nondiabetic Subjects With Nonalcoholic Steatohepatitis. *Gastroenterology*. 2008;135(4):1176-1184. doi:10.1053/j.gastro.2008.06.047

35. Caldwell SH, Battle EH. A Pilot Study of a Thiazolidinedione, Troglitazone, in Nonalcoholic Steatohepatitis. 2001;96(2).

36. Yang JD, Abdelmalek MF, Pang H, et al. Gender and Menopause Impact Severity of Fibrosis Among Patients with Nonalcoholic Steatohepatitis. *Hepatology*. 2014;59(4):1406-1414. doi:10.1002/hep.26761

37. Vernon G, Baranova A, Younossi ZM. Systematic review: the epidemiology and natural history of non-alcoholic fatty liver disease and non-alcoholic steatohepatitis in adults.

Alimentary Pharmacology & Therapeutics. 2011;34(3):274-285. doi:10.1111/j.1365-2036.2011.04724.x

38. Sex Differences in NAFLD: State of the Art and Identification of Research Gaps - PMC. Accessed June 15, 2023. https://www.ncbi.nlm.nih.gov/pmc/articles/PMC6766425/

39. Ong JP, Pitts A, Younossi ZM. Increased overall mortality and liver-related mortality in non-alcoholic fatty liver disease. *Journal of Hepatology*. 2008;49(4):608-612. doi:10.1016/j.jhep.2008.06.018

40. Foryst-Ludwig A, Clemenz M, Hohmann S, et al. Metabolic Actions of Estrogen Receptor Beta (ERβ) are Mediated by a Negative Cross-Talk with PPARγ. *PLoS Genet*. 2008;4(6):e1000108. doi:10.1371/journal.pgen.1000108

41. Khatun M, Ray RB. Mechanisms Underlying Hepatitis C Virus-Associated Hepatic Fibrosis. *Cells*. 2019;8(10). doi:10.3390/cells8101249

42. Khomich O, Ivanov AV, Bartosch B. Metabolic Hallmarks of Hepatic Stellate Cells in Liver Fibrosis. *Cells*. 2019;9(1):24. doi:10.3390/cells9010024

43. de Oliveria Andrade LJ, D'Oliveira A, Melo RC, De Souza EC, Costa Silva CA, Paraná R. Association Between Hepatitis C and Hepatocellular Carcinoma. *J Glob Infect Dis*. 2009;1(1):33-37. doi:10.4103/0974-777X.52979

44. Mittal S, El-Serag HB. Epidemiology of HCC: Consider the Population. *J Clin Gastroenterol*. 2013;47(0):S2-S6. doi:10.1097/MCG.0b013e3182872f29

45. Dhamija E, Paul SB, Kedia S. Non-alcoholic fatty liver disease associated with hepatocellular carcinoma: An increasing concern. *Indian J Med Res*. 2019;149(1):9-17. doi:10.4103/ijmr.IJMR_1456_17

46. Sung H, Ferlay J, Siegel RL, et al. Global Cancer Statistics 2020: GLOBOCAN Estimates of Incidence and Mortality Worldwide for 36 Cancers in 185 Countries. *CA: A Cancer Journal for Clinicians*. 2021;71(3):209-249. doi:10.3322/caac.21660

47. Baglieri J, Brenner DA, Kisseleva T. The Role of Fibrosis and Liver-Associated Fibroblasts in the Pathogenesis of Hepatocellular Carcinoma. *Int J Mol Sci*. 2019;20(7):1723. doi:10.3390/ijms20071723

48. Regev A, Berho M, Jeffers LJ, et al. Sampling error and intraobserver variation in liver biopsy in patients with chronic HCV infection. *The American Journal of Gastroenterology*. 2002;97(10):2614-2618. doi:10.1111/j.1572-0241.2002.06038.x

49. Bedossa P, Poynard T. An algorithm for the grading of activity in chronic hepatitis C. *Hepatology*. 1996;24(2):289-293. doi:10.1002/hep.510240201

50. Afdhal NH. Fibroscan (Transient Elastography) for the Measurement of Liver Fibrosis. *Gastroenterol Hepatol (N Y)*. 2012;8(9):605-607.

51. Understanding Your Liver Elastography (FibroScan®) Results | Memorial Sloan Kettering Cancer Center. Accessed September 29, 2023. https://www.mskcc.org/cancer-care/patient-education/understanding-your-fibroscan-results

52. Why are non-invasive risk scores such as FIB-4 used in clinical practice? | AASLD. Published February 20, 2022. Accessed November 29, 2023. https://www.aasld.org/liver-fellow-network/core-series/why-series/why-are-non-invasive-risk-scores-such-fib-4-used

53. Emerging Roles of T Cells in the Pathogenesis of Nonalcoholic Steatohepatitis and Hepatocellular Carcinoma - PMC. Accessed October 3, 2023. https://www-ncbi-nlm-nih-gov.proxy.bib.uottawa.ca/pmc/articles/PMC8581300/

54. Kazankov K, Jørgensen SMD, Thomsen KL, et al. The role of macrophages in nonalcoholic fatty liver disease and nonalcoholic steatohepatitis. *Nat Rev Gastroenterol Hepatol*. 2019;16(3):145-159. doi:10.1038/s41575-018-0082-x

55. Barrow F, Khan S, Wang H, Revelo XS. The Emerging Role of B Cells in the Pathogenesis of NAFLD. *Hepatology*. 2021;74(4):2277-2286. doi:10.1002/hep.31889

56. Jerrells TR. Role of activated CD8+ T cells in the initiation and continuation of hepatic damage. *Alcohol*. 2002;27(1):47-52. doi:10.1016/S0741-8329(02)00210-0

57. Dudek M, Pfister D, Donakonda S, et al. Auto-aggressive CXCR6+ CD8 T cells cause liver immune pathology in NASH. *Nature*. 2021;592(7854):444-449. doi:10.1038/s41586-021-03233-8

58. He B, Wu L, Xie W, et al. The imbalance of Th17/Treg cells is involved in the progression of nonalcoholic fatty liver disease in mice. *BMC Immunol*. 2017;18:33. doi:10.1186/s12865-017-0215-y

59. Zhang M, Zhang S. T Cells in Fibrosis and Fibrotic Diseases. *Front Immunol*. 2020;11:1142. doi:10.3389/fimmu.2020.01142

60. Bhogal RK, Bona CA. B cells: no longer bystanders in liver fibrosis. *J Clin Invest*. 2005;115(11):2962-2965. doi:10.1172/JCI26845

61. Winer DA, Winer S, Shen L, et al. B Lymphocytes Promote Insulin Resistance through Modulation of T Lymphocytes and Production of Pathogenic IgG Antibody. *Nat Med*. 2011;17(5):610-617. doi:10.1038/nm.2353

62. Zhang N, Bevan MJ. CD8+ T Cells: Foot Soldiers of the Immune System. *Immunity*. 2011;35(2):161-168. doi:10.1016/j.immuni.2011.07.010

63. Sigal LJ. Activation of CD8 T Lymphocytes during Viral Infections. *Encyclopedia of Immunobiology*. Published online 2016:286-290. doi:10.1016/B978-0-12-374279-7.14009-3

64. Nolz JC, Starbeck-Miller GR, Harty JT. Naive, effector and memory CD8 T-cell trafficking: parallels and distinctions. *Immunotherapy*. 2011;3(10):1223-1233. doi:10.2217/imt.11.100

65. Bennett TJ, Udupa VAV, Turner SJ. Running to Stand Still: Naive CD8+ T Cells Actively Maintain a Program of Quiescence. *Int J Mol Sci*. 2020;21(24):9773. doi:10.3390/ijms21249773

66. Raskov H, Orhan A, Christensen JP, Gögenur I. Cytotoxic CD8+ T cells in cancer and cancer immunotherapy. *Br J Cancer*. 2021;124(2):359-367. doi:10.1038/s41416-020-01048-4

67. Charles A Janeway J, Travers P, Walport M, Shlomchik MJ. T cell-mediated cytotoxicity. In: *Immunobiology: The Immune System in Health and Disease. 5th Edition*. Garland Science; 2001. Accessed September 20, 2023. https://www.ncbi.nlm.nih.gov/books/NBK27101/

68. Sung PS, Racanelli V, Shin EC. CD8+ T-Cell Responses in Acute Hepatitis C Virus Infection. *Front Immunol*. 2014;5:266. doi:10.3389/fimmu.2014.00266

69. Hofmann M, Tauber C, Hensel N, Thimme R. CD8+ T Cell Responses during HCV Infection and HCC. *J Clin Med*. 2021;10(5):991. doi:10.3390/jcm10050991

70. Kurachi M. CD8+ T cell exhaustion. *Semin Immunopathol*. 2019;41(3):327-337. doi:10.1007/s00281-019-00744-5

71. Trautmann L, Janbazian L, Chomont N, et al. Upregulation of PD-1 expression on HIV-specific CD8+ T cells leads to reversible immune dysfunction. *Nat Med*. 2006;12(10):1198-1202. doi:10.1038/nm1482

72. Fenwick C, Joo V, Jacquier P, et al. T-cell exhaustion in HIV infection. *Immunol Rev*. 2019;292(1):149-163. doi:10.1111/imr.12823

73. Yates KB, Tonnerre P, Martin GE, et al. Epigenetic scars of CD8+ T cell exhaustion persist after cure of chronic infection in humans. *Nat Immunol*. 2021;22(8):1020-1029. doi:10.1038/s41590-021-00979-1

74. Ringelhan M, Pfister D, O'Connor T, Pikarsky E, Heikenwalder M. The immunology of hepatocellular carcinoma. *Nat Immunol*. 2018;19(3):222-232. doi:10.1038/s41590-018-0044-z

75. Schinkel SCB, Carrasco-Medina L, Cooper CL, Crawley AM. Generalized Liver- and Blood-Derived CD8+ T-Cell Impairment in Response to Cytokines in Chronic Hepatitis C Virus Infection. *PLOS ONE*. 2016;11(6):e0157055. doi:10.1371/journal.pone.0157055

76. Petrovas C, Mueller YM, Dimitriou ID, et al. Increased mitochondrial mass characterizes the survival defect of HIV-specific CD8+ T cells. *Blood*. 2007;109(6):2505-2513. doi:10.1182/blood-2006-05-021626

77. Vranjkovic A, Deonarine F, Kaka S, Angel JB, Cooper CL, Crawley AM. Direct-Acting Antiviral Treatment of HCV Infection Does Not Resolve the Dysfunction of Circulating CD8+ T-Cells in Advanced Liver Disease. *Frontiers in Immunology*. 2019;10. Accessed January 4, 2023. https://www.frontiersin.org/articles/10.3389/fimmu.2019.01926

78. Massanella M, Negredo E, Pérez-Álvarez N, et al. CD4 T-cell hyperactivation and susceptibility to cell death determine poor CD4 T-cell recovery during suppressive HAART. *AIDS*. 2010;24(7):959-968. doi:10.1097/QAD.0b013e328337b957

79. Metabolic signaling in T cells | Cell Research. Accessed September 14, 2023. https://www.nature.com/articles/s41422-020-0379-5

80. Konjar Š, Veldhoen M. Dynamic Metabolic State of Tissue Resident CD8 T Cells. *Front Immunol*. 2019;10:1683. doi:10.3389/fimmu.2019.01683

81. Turbitt WJ, Rosean CB, Weber KS, Norian LA. Obesity and CD8 T cell metabolism: Implications for anti-tumor immunity and cancer immunotherapy outcomes. *Immunol Rev*. 2020;295(1):203-219. doi:10.1111/imr.12849

82. Buck MD, O'Sullivan D, Pearce EL. T cell metabolism drives immunity. *J Exp Med*. 2015;212(9):1345-1360. doi:10.1084/jem.20151159

83. Zheng K, Zheng X, Yang W. The Role of Metabolic Dysfunction in T-Cell Exhaustion During Chronic Viral Infection. *Front Immunol*. 2022;13:843242. doi:10.3389/fimmu.2022.843242

84. Bengsch B, Johnson AL, Kurachi M, et al. Bioenergetic insufficiencies due to metabolic alterations regulated by PD-1 are an early driver of CD8+ T cell exhaustion. *Immunity*. 2016;45(2):358-373. doi:10.1016/j.immuni.2016.07.008

85. Aregay A, Owusu Sekyere S, Deterding K, et al. Elimination of hepatitis C virus has limited impact on the functional and mitochondrial impairment of HCV-specific CD8+ T cell responses. *Journal of Hepatology*. 2019;71(5):889-899. doi:10.1016/j.jhep.2019.06.025

86. Schurich A, Pallett LJ, Jajbhay D, et al. Distinct Metabolic Requirements of Exhausted and Functional Virus-Specific CD8 T Cells in the Same Host. *Cell Rep*. 2016;16(5):1243-1252. doi:10.1016/j.celrep.2016.06.078

87. Paredes JL, Fernandez-Ruiz R, Niewold TB. T Cells in Systemic Lupus Erythematosus. *Rheum Dis Clin North Am*. 2021;47(3):379-393. doi:10.1016/j.rdc.2021.04.005

88. Yin Y, Choi SC, Xu Z, et al. Normalization of CD4+ T Cell Metabolism Reverses Lupus. *Sci Transl Med*. 2015;7(274):274ra18. doi:10.1126/scitranslmed.aaa0835

89. Ohmes J, Comdühr S, Akbarzadeh R, Riemekasten G, Humrich JY. Dysregulation and chronicity of pathogenic T cell responses in the pre-diseased stage of lupus. *Frontiers in Immunology*. 2022;13. Accessed September 15, 2023. https://www.frontiersin.org/articles/10.3389/fimmu.2022.1007078

90. Howie D, Ten Bokum A, Necula AS, Cobbold SP, Waldmann H. The Role of Lipid Metabolism in T Lymphocyte Differentiation and Survival. *Front Immunol*. 2018;8:1949. doi:10.3389/fimmu.2017.01949

91. Wang Z, Aguilar EG, Luna JI, et al. Paradoxical effects of obesity on T cell function during tumor progression and PD-1 checkpoint blockade. *Nat Med*. 2019;25(1):141-151. doi:10.1038/s41591-018-0221-5

92. Finlay DK, Rosenzweig E, Sinclair LV, et al. PDK1 regulation of mTOR and hypoxia-inducible factor 1 integrate metabolism and migration of CD8+ T cells. *J Exp Med*. 2012;209(13):2441-2453. doi:10.1084/jem.20112607

93. Burm R, Collignon L, Mesalam AA, Meuleman P. Animal Models to Study Hepatitis C Virus Infection. *Front Immunol*. 2018;9:1032. doi:10.3389/fimmu.2018.01032

94. Mouse Models of Liver Fibrosis | SpringerLink. Accessed September 14, 2023. https://link.springer.com/protocol/10.1007/978-1-0716-1382-5_23

95. Scholten D, Trebicka J, Liedtke C, Weiskirchen R. The carbon tetrachloride model in mice. *Lab Anim*. 2015;49(1_suppl):4-11. doi:10.1177/0023677215571192

96. Starkel P, Leclercq IA. Animal models for the study of hepatic fibrosis. *Best Practice & Research Clinical Gastroenterology*. 2011;25(2):319-333. doi:10.1016/j.bpg.2011.02.004

97. Choline's role in maintaining liver function: new evidence for epigenetic mechanisms - PMC. Accessed November 29, 2023. https://www-ncbi-nlm-nih-gov.proxy.bib.uottawa.ca/pmc/articles/PMC3729018/

98. Zhong F, Zhou X, Xu J, Gao L. Rodent Models of Nonalcoholic Fatty Liver Disease. *Digestion*. 2020;101(5):522-535. doi:10.1159/000501851

99. Matsumoto M, Hada N, Sakamaki Y, et al. An improved mouse model that rapidly develops fibrosis in non-alcoholic steatohepatitis. *Int J Exp Pathol*. 2013;94(2):93-103. doi:10.1111/iep.12008

100. Velázquez KT, Enos RT, Bader JE, et al. Prolonged high-fat-diet feeding promotes non-alcoholic fatty liver disease and alters gut microbiota in mice. *World J Hepatol*. 2019;11(8):619-637. doi:10.4254/wjh.v11.i8.619

101. Chiba T, Suzuki S, Sato Y, Itoh T, Umegaki K. Evaluation of Methionine Content in a High-Fat and Choline-Deficient Diet on Body Weight Gain and the Development of Non-Alcoholic

Steatohepatitis in Mice. *PLoS One*. 2016;11(10):e0164191. doi:10.1371/journal.pone.0164191

102. Wei G, An P, Vaid KA, et al. Comparison of murine steatohepatitis models identifies a dietary intervention with robust fibrosis, ductular reaction, and rapid progression to cirrhosis and cancer. *Am J Physiol Gastrointest Liver Physiol*. 2020;318(1):G174-G188. doi:10.1152/ajpgi.00041.2019

103. Madani J, Li J, Vranjkovic A, et al. CD8 T cell hyperfunction and reduced tumour control in models of advanced liver fibrosis. Published online September 22, 2023:2023.09.20.557752. doi:10.1101/2023.09.20.557752

104. Li J, Vranjkovic A, Read D, et al. Differential and lasting gene expression changes in circulating CD8 T cells in chronic HCV infection with cirrhosis and related insights on the role of Hedgehog signaling. Published online September 21, 2023:2023.09.20.557725. doi:10.1101/2023.09.20.557725

105. A06071302 Formula - Search Formulas - Research Diets, Inc. Accessed November 22, 2023. https://researchdiets.com/formulas/a06071302

106. Inotiv. 2018 Teklad Global 18% Protein Rodent Diets. Accessed November 22, 2023. https://www.inotivco.com/rodent-natural-ingredient-2018-diets

107. D12451 Formula - Search Formulas - Research Diets, Inc. Accessed December 3, 2023. https://researchdiets.com/formulas/d12451

108. Inotiv. 2014 Teklad Global 14% Protein Rodent Maintenance Diets. Accessed November 24, 2023. https://www.inotivco.com/rodent-natural-ingredient-2014-diets

109. EasySep™ Mouse CD8+ T Cell Isolation Kit | STEMCELL Technologies. Accessed November 24, 2023. https://www.stemcell.com/products/easysep-mouse-cd8-t-cell-isolation-kit.html

110. Mouse Spleen Cell Isolation Protocol - CA. Accessed November 24, 2023. https://www.thermofisher.com/ca/en/home/life-science/cell-analysis/cell-analysis-learning-center/immunology-at-work/immunology-protocols/mouse-spleen-cell-isolation-protocol.html

111. How to Prepare a Single Cell Suspension from Mouse Spleen. Accessed November 24, 2023. https://www.stemcell.com/prepare-single-cell-suspension-from-mouse-spleen.html

112. Cornell Univeristy. User Guide: Agilent Seahorse Units. https://www.biotech.cornell.edu/sites/default/files/2020-06/Seahorse%20User%20Guide.pdf

113. Leonard AK, Loughran EA, Klymenko Y, et al. Chapter 4 - Methods for the visualization and analysis of extracellular matrix protein structure and degradation. In: Mecham RP, ed.

Methods in Cell Biology. Vol 143. Methods in Extracellular Matrix Biology. Academic Press; 2018:79-95. doi:10.1016/bs.mcb.2017.08.005

114. Zorova LD, Popkov VA, Plotnikov EY, et al. Mitochondrial membrane potential. *Anal Biochem*. 2018;552:50-59. doi:10.1016/j.ab.2017.07.009

115. Plaisance EP, Greenway FL, Boudreau A, et al. Dietary Methionine Restriction Increases Fat Oxidation in Obese Adults with Metabolic Syndrome. *J Clin Endocrinol Metab*. 2011;96(5):E836-E840. doi:10.1210/jc.2010-2493

116. Cacciottolo TM, Kumar A, Godfrey EM, Davies SE, Allison M. Spleen Size Does Not Correlate With Histological Stage of Liver Disease in People With Nonalcoholic Fatty Liver Disease. *Clinical Gastroenterology and Hepatology*. 2023;21(2):535-537.e1. doi:10.1016/j.cgh.2022.01.007

117. Body Weight Information for Aged C57BL/6J (000664). The Jackson Laboratory. Accessed October 27, 2023. https://www.jax.org/jax-mice-and-services/strain-data-sheet-pages/body-weight-chart-aged-b6

118. Xiong M, Li J, Yang S, et al. Influence of Gender and Reproductive Factors on Liver Fibrosis in Patients With Chronic Hepatitis B Infection. *Clin Transl Gastroenterol*. 2019;10(10):e00085. doi:10.14309/ctg.0000000000000085

119. Diaz Brinton R. Minireview: Translational Animal Models of Human Menopause: Challenges and Emerging Opportunities. *Endocrinology*. 2012;153(8):3571-3578. doi:10.1210/en.2012-1340

120. Fahed G, Aoun L, Bou Zerdan M, et al. Metabolic Syndrome: Updates on Pathophysiology and Management in 2021. *Int J Mol Sci*. 2022;23(2):786. doi:10.3390/ijms23020786

121. Fibrosis reversal after hepatitic C virus elimination - PMC. Accessed November 14, 2023. https://www-ncbi-nlm-nih-gov.proxy.bib.uottawa.ca/pmc/articles/PMC6535048/

122. Luna-Cuadros MA, Chen HW, Hanif H, Ali MJ, Khan MM, Lau DTY. Risk of hepatocellular carcinoma after hepatitis C virus cure. *World J Gastroenterol*. 2022;28(1):96-107. doi:10.3748/wjg.v28.i1.96

123. Vranjkovic A, Deonarine F, Kaka S, Angel JB, Cooper CL, Crawley AM. Direct-Acting Antiviral Treatment of HCV Infection Does Not Resolve the Dysfunction of Circulating CD8+ T-Cells in Advanced Liver Disease. *Front Immunol*. 2019;10:1926. doi:10.3389/fimmu.2019.01926

124. Sun XF, Gu L, Deng WS, Xu Q. Impaired balance of T helper 17/T regulatory cells in carbon tetrachloride-induced liver fibrosis in mice. *World J Gastroenterol*. 2014;20(8):2062-2070. doi:10.3748/wjg.v20.i8.2062

125. Tarantino G, Citro V, Balsano C. Liver-spleen axis in nonalcoholic fatty liver disease. *Expert Review of Gastroenterology & Hepatology*. 2021;15(7):759-769. doi:10.1080/17474124.2021.1914587

126. Heyens LJM, Busschots D, Koek GH, Robaeys G, Francque S. Liver Fibrosis in Non-alcoholic Fatty Liver Disease: From Liver Biopsy to Non-invasive Biomarkers in Diagnosis and Treatment. *Frontiers in Medicine*. 2021;8. Accessed November 15, 2023. https://www.frontiersin.org/articles/10.3389/fmed.2021.615978

127. Zhong X, Lv M, Ma M, et al. State of CD8+ T cells in progression from nonalcoholic steatohepatitis to hepatocellular carcinoma: From pathogenesis to immunotherapy. *Biomedicine & Pharmacotherapy*. 2023;165:115131. doi:10.1016/j.biopha.2023.115131

128. Xu L, Wang X, Chen Y, et al. Metformin Modulates T Cell Function and Alleviates Liver Injury Through Bioenergetic Regulation in Viral Hepatitis. *Frontiers in Immunology*. 2021;12. Accessed November 22, 2023. https://www.frontiersin.org/articles/10.3389/fimmu.2021.638575

129. Lang P, Hasselwander S, Li H, Xia N. Effects of different diets used in diet-induced obesity models on insulin resistance and vascular dysfunction in C57BL/6 mice. *Sci Rep*. 2019;9(1):19556. doi:10.1038/s41598-019-55987-x